ROYAUME DU MAROC
Université Mohammed V - RABAT -
جامعة محمد الخامس – الرباط –
Faculté des sciences
كلية العلوم
CENTRE D'ÉTUDES DOCTORALES - SCIENCES ET TECHNOLOGIES

N° d'ordre : 3713

THÈSE

En vue de l'obtention du : ***DOCTORAT***

Structure de Recherche : Laboratoire de la Matière Condensée et des Sciences Interdisciplinaires (LaMCScI)-URL CNRST

Discipline : Physique Informatique

Spécialité : Science des matériaux

Présentée et soutenue le : 03/12/2022
Par :

Hajar Moatassim

In-depth Atomic-scale study of hybrid perovskite materials for photovoltaic application

JURY

Hamid EZ-ZAHRAOUY	PES, Université Mohammed V, Faculté des Sciences de Rabat	Président
Mimoun ZAZOUI	PES, Université Hassan II, FST Mohammedia	Rapporteur /Examinateur
El Mehdi SALMANI	PH, Université Mohammed V, Faculté des Sciences de Rabat	Rapporteur /Examinateur
Abdallah EL KENZ	PES, Université Mohammed V, Faculté des Sciences de Rabat	Rapporteur/Examinateur
Abdelilah BENYOUSSEF	Expert, PES, Academy Hassan II des Sciences et Techniques, Rabat	Examinateur
Omar MOUNKACHI	PH, Université Mohammed V, Faculté des Sciences de Rabat	Co-Directeur de thèse
Mohammed LOULIDI	PES, Université Mohammed V, Faculté des Sciences de Rabat	Directeur de thèse
Halima ZAARI	PA, Université Mohammed V, Faculté des Sciences de Rabat	Invitée

Année Universitaire: 2022/2023

Acknowledgements

This work was carried out within the Laboratory of Condensed Matter and Interdisciplinary of Sciences under the direction of Professor **Loulidi Mohammed** and the co-advisor Professor **Mounkachi Omar**.

First and foremost, I owe a huge debt of gratitude to my supervisor Professor **Loulidi Mohammed,** PES in FSR for his professional guidance, generous advice, and extraordinary measure of patience. I feel incredibly fortunate to have had the opportunity of his mentorship.

My innermost gratitude is also conveyed to my co-advisor Professor **Mounkachi Omar,** PH in FSR for his guidance, tireless efforts, and for providing a conducive and exemplary work atmosphere with other colleagues.

Additional thanks go to Professor **Ez-zahraouy Hamid,** PES in FSR for accepting the presidency of the jury, for his availability, and help at any time, and for many in-depth discussions.

I would like to thank Professor **Zazoui Mimoun,** PES in FST for agreeing to participate in this jury as rapporteur and for reading my dissertation.

I warmly thank the Professor **Salmani El mehdi,** PH in FSR for agreeing to participate in this jury as rapporteur and also for his advice, discussion, and reading my dissertation.

I would like to thank Professor **El Kenz Abdallah,** PES in FSR for agreeing to participate in this jury as rapporteur, I would thank him also for his insightful comments and advices that have contributed in the development and bringing up of this work.

Particular thanks go to Professor **Abdelilah Benyoussef,** PES in FSR for accepting to participate in this jury as examiner, and for many fruitful and in-depth discussions that were really the font of all learning and also for his willingness to share knowledge.

✉ Faculté des Sciences, avenue Ibn Battouta, BP. 1014 RP, Rabat –Maroc
☎ 00212(05) 537 77 18 34/35/38, 🖷 00212(05) 537 77 42 61, http://www.fsr.ac.ma

Acknowledgements

I would like to pay my special regards to Professor **Zaari Halima,** PA in FSR who has guided and supported me throughout this thesis for accepting to participate in this jury as examiner, and for making tasks easier to complete with her company.

I cannot forget to thank my family and my friends for their love and support, without there company it would not be easy for me to reach this position where I could attempt a PhD. Finally, I would like to thank my colleagues from the Laboratory of Condensed Matter and Interdisciplinary of Sciences for the exchange we had and the good time we shared.

Hajar Moatassim

✉ Faculté des Sciences, avenue Ibn Battouta, BP. 1014 RP, Rabat –Maroc
☎ 00212(05) 537 77 18 34/35/38, 🖷 00212(05) 537 77 42 61, http://www.fsr.ac.ma

ABSTRACT

Energy plays a major role in the modern world and contributes significantly in humanity development. To fulfill the energy demand and also overcome the problem of global warming, many researchers have been interested in the development of renewable energy such as the solar energy. In the present time hybrid lead halide perovskites used as light absorbers in photovoltaic cells have demonstrated an excellent interest due to their optoelectronic properties and their high efficiency. Yet, they have also shown some drawbacks, such as their high degradation which influences their performances. Furthermore, most of this hybrid perovskites contain toxic lead which has a negative impact on the environment. In this context, this thesis presents an in-depth access and understanding of the hybrid perovskite fundamental atomic-scale properties as well as suggest some approaches to mitigate the hybrid perovskite degradation processes and also to reduce their toxicity. Results obtained in this thesis provide an examination of the hybrid perovskite degradation mechanism in the presence of moister and oxygen. Limitation of degradation against oxygen as well as an approach for mitigating the water-hybrid perovskite interaction are discussed also. Furthermore, new efficient less lead halide perovskites are suggested and carried out in this thesis.

Keywords : Hybrid perovskite, Photovoltaic, Organic, Inorganic, $CH_3NH_3PbI_3$, DFT, Solar cell.

✉ Faculté des Sciences, avenue Ibn Battouta, BP. 1014 RP, Rabat –Maroc
☎ 00212(05) 537 77 18 34/35/38, 🖷 00212(05) 537 77 42 61, http://www.fsr.ac.ma

RESUME

L'énergie a un rôle majeur dans le monde moderne et contribue de manière significative au développement de l'humanité. Pour répondre à la demande en énergie et surmonter le problème du réchauffement climatique, de nombreux chercheurs se sont intéressés au développement d'énergies renouvelables telle que l'énergie solaire. À l'heure actuelle, les pérovskites hybrides d'halogénure de plomb utilisées comme absorbeurs de lumière dans les cellules photovoltaïques, ont suscité un grand intérêt en raison de leurs propriétés optoélectroniques impressionnantes ainsi que leur rendement élevé. Cependant, elles ont également montré quelques inconvénients, tel que leur forte dégradation qui influence leurs performances. De plus, ces pérovskites hybrides contiennent le plomb qui est toxique ce qui impacte négativement l'environnement. Dans ce contexte, cette thèse présente une étude approfondie pour une compréhension des propriétés fondamentales des pérovskites hybrides à l'échelle atomique et propose ainsi certaines approches pour atténuer les processus de dégradation des pérovskites hybrides et réduire leur toxicité. Les résultats obtenus dans cette thèse fournissent un examen du mécanisme de dégradation de la pérovskite hybride en présence d'humidité et d'oxygène. La limitation de la dégradation contre l'oxygène ainsi qu'une approche pour atténuer l'interaction eau-pérovskite hybride sont également discutées. De plus, de nouvelles pérovskites moins toxiques et qui présentent une efficacité élevée sont suggérées et étudiées dans cette thèse.

Mot clé : Perovskite hybride, Photovoltaique, Organique, Inorganique, $CH_3NH_3PbI_3$, DFT, Cellule solaire

✉ Faculté des Sciences, avenue Ibn Battouta, BP. 1014 RP, Rabat –Maroc
☎ 00212(05) 537 77 18 34/35/38, 🖷 00212(05) 537 77 42 61, http://www.fsr.ac.ma

List of publication

1. **Patent "**New hybrid material, non-toxic, efficient for photovoltaic application"
2. **Moatassim, H**.; Zaari, H.; Kenz, A. E.; Benyoussef, A.; Loulidi, M.; Mounkachi, O. Theoretical Investigation of FAPbSnGeX3 Efficiency. *RSC Adv.* 2022, *12* (15), 8945–8952.

   https://doi.org/10.1039/D2RA00345G
3. **Moatassim, H**.; El Kenz, A.; Benyoussef, A.; Loulidi, M.; Mounkachi, O. Degradation Mechanism of CH3NH3PbI3 and Enhancing Its Optical Absorption through Variety of Doping Sites. *Comput. Condens. Matter* 2021, *29*, e00611. https://doi.org/10.1016/j.cocom.2021.e00611
4. Boubekraoui, A.; **Moatassim, H**.; Al-Shami, A.; Ez-Zahraouy, H. DFT Study of Structural, Electronic, and Thermoelectric Properties of Cs2PdX(X=Br2Be2Te2) Compound. *Comput. Condens. Matter* 2021, *29*, e00600. https://doi.org/10.1016/j.cocom.2021.e00600
5. **Moatassim, H**.; Zaari, H.; Kenz, A. E.; Benyoussef, A.; Loulidi, M.; Mounkachi, O. An inside mechanism understanding to mitigate vacancy formation and water interaction in hybrid perovskite (in peer-reviewed process).

✉ Faculté des Sciences, avenue Ibn Battouta, BP. 1014 RP, Rabat –Maroc
☎ 00212(05) 537 77 18 34/35/38, 🖷 00212(05) 537 77 42 61, http://www.fsr.ac.ma

ABBREVIATIONS

PV	Photovoltaic
ETL	Electron Transport Layer
HTL	Hole Transport Layer
SRH	Shockley-Read-Hall
PCE	Power Conversion Efficiency
J_{sc}	The short-circuit current density
V_{oc}	The open-circuit voltage
FF	Fill Factor
P_{sun}	solar irradiation
R_{sh}	shunt resistance
R_s	Series resistance
P	Electrical power
I	Electric current
P_{max}	Maximum power point
EQE	External quantum efficiency
PVC	Photovoltaic Cell
DSSCs	Dye-Sensitized Solar Cells
UV	Ultrat Violet
PSCs	Perovskite solar cells
CTL	Charge Transporting Layer
ALD	Atomic Layer Deposition
FC	Front Contact
BC	Back Contact
HOIP	Hybrid Organic Inorganic Perovskite
BIPV	Building-Integrated Photovoltaic
DFT	Density Functional Theory

General introduction

Energy plays a major role in the modern world and contributes significantly in humanity's development. The world's energy demand increased during the recent years due to the increase of both the population and the living standard which are estimated to grow up by 50% in 2037[1] leading to a rise of the energy cost[2]. Over the centuries, fossil fuel has been considered as the main source of energy. With the growing of population, these fossil fuels run out faster than they are generated. Although, the fossil fuels represent a billion-dollar market for the industry it has downsides as the impact that it has on the environment, moreover, being one of the major elements contributing to the global warming. The use of oil, gas and coal causes an ecological and environmental problem especially coal that produces more CO_2 than the other fossil fuels, in addition, more than 60% of fossil fuels energy used for electricity generation is lost in conversion[3]. Thus, fossil fuels are not a sustainable energy source. To solve these problems, the researchers turn out to the renewable energy such as biomass energy, wind energy, and solar energy. The main source of the available energy in the planet is the sun[4]. Solar energy is everywhere and available in great abundance, it's the fastest growing energy technology. The Sun produces a massive 3.828×10^{26} watts of electromagnetic radiation[5]. The radiation that reaches the earth becomes less due to the reflection by the clouds, atmosphere and Earth's surface. However, the total energy hitting the Earth represents more than 10,000 times the world's total energy use[6]. Thus, solar energy represents a high heat source which lasts throughout the years and also can meet all technological, industrial, and residential sector demands of humanity. The photosynthesis procedure converts energy of light into energy of chemical compounds resulting in chemical fuel from sunlight, the latter can also produce heat and electricity[7]. The conversion of sunlight into electrical energy goes through photovoltaic panels, solar thermal power plants and also trough mirrors that concentrate solar radiation. This solar energy can be conserving and stored by thermal storage, battery storage and mechanical storage. Therefore, the energy storage can be used to fulfil the mismatch between energy supply and consumption[8]. In 2019, the renewable technologies were assigned to satisfy 11% of global primary energy. Morocco is the largest energy importer in North Africa, generating a total of 4.7 TWh, 1.64 TWh, and 1.85 TWh by the year 2019 by wind, hydropower and solar respectively[9]. Furthermore, Morocco has also launched one of the world's largest and most ambitious solar energy plans with an investment of 9billion USD to reduce its reliance on imported

fossil fuels and to expand wind, hydroelectric and solar photovoltaics (PV) development[10]. The first generation of solar cells has been developed in 1958 and was mainly based on crystalline Silicon that has dominated the largest commercial PV installations. Solar cell-based crystalline Silicon has shown success in photovoltaics reaching today an efficiency of 25.25%. However, this efficiency has become stagnated because of the expense of the material and its elaboration. In this context, recently hybrid perovskite materials have been put in the spotlight due to their high power conversion efficiency that has achieved a value of 25.8% in a few years[11]. Hybrid perovskite materials have become a center of interest and competitive materials for photovoltaic applications. These materials showed impressive properties and are so far more complicated than the CiGs, Si, and the other materials used in solar cell[12]. $MAPbI_3$ has been the most efficient hybrid perovskite to undergo investigation during the few last years, however, it presents an imperative challenge that includes the enhancement of its stability and the elimination of toxicity. Hybrid perovskite suffers from an instability against moisture, oxygen, ultra violet (UV), and light. Different strategies have been studied to improve the hybrid perovskite stability such as their encapsulation[13], composition engineering[14], or enhancing their films crystallinity by varying or mixing different elements (cation organic or/and halogen) constituting the hybrid perovskite material[15]. In the other hand, these compounds contain toxic lead that blocks the commercialization of these materials, so far, no substitution of lead has demonstrated a better performance than the $MAPbI_3$. In this regard, this thesis provides a detailed study and in-depth access to the $MAPbI_3$ hybrid perovskite properties as well as presents multiple approaches that serve to diminish toxicity of hybrid perovskite and to mitigate the perovskite weaknesses that are still under intense debate.

This thesis will be organized as follows:

In Section 1 an introduction to the photovoltaic effect as well as the important parameters provided for the power conversion efficiency calculation and the different photovoltaic technology, generation will be introduced firstly. After, we will give a description of solar cells-based hybrid perovskite, their synthesis, and deposition method used for their fabrication. Furthermore, the hybrid perovskite material properties, deep understanding of their mechanism degradation, technology used to improve their stability, and research progress summary on the performance of lead-free PSCs will be discussed in this section.

In Section 2 we give a compressive survey on density functional theory and its implementation. For this purpose, we present the Schrodinger equation that is the basis equation for all theoretical studies of material physical properties as well as the approximation used for simplifying this equation. In this section we describe also how Bloch's theorem in combination with pseudopotential can be used for describing the system's properties as well as we introduce the description of the Quantum espresso code that has been used in the research outcomes investigation of this thesis.

Section 3 represents results of the research evaluated during this thesis. The main focus of this section is understanding the degradation mechanism of hybrid perovskite, enhancing and reducing their degradation processes, and suggesting potential new less toxic materials candidates for photovoltaic application. In this section the investigation of the bromine doping effect on $MAPbI_3$ as well as a detailed study of the influence of vacancy and humidity on the degradation of hybrid perovskite were established. A rational approach to diminish the toxicity and increase the stability of these compounds was investigated also. Finally, power conversion of new promising less lead halide perovskite was provided.

General Conclusion summarizes the main contributions that were made throughout this research regarding the development of new strategies to overcome the defects that the hybrid perovskite $MAPbI_3$ suffers from such as instability and toxicity and to furthermore improve its physical properties to better suit the photovoltaic application. As perspective, we pointed out in this conclusion that we plan to work on the experimental aspect of this material as well as we are working on the realization of a prototype of a photovoltaic cell in the future.

Introduction générale

L'énergie joue un rôle majeur dans le monde moderne et est un moteur essentiel pour le développement de l'humanité. Cependant, la demande croissante en énergie a entraîné une augmentation des émissions de gaz à effet de serre et a exacerbé le problème du réchauffement climatique. Afin de relever ce défi, de nombreux chercheurs se sont tournés vers les énergies renouvelables telles que l'énergie solaire.

Actuellement, les pérovskites hybrides d'halogénure de plomb sont utilisées comme absorbeurs de lumière dans les cellules photovoltaïques en raison de leur rendement élevé et de leurs propriétés optoélectroniques impressionnantes. Cependant, ces pérovskites hybrides présentent des inconvénients, tels que leur forte dégradation qui affecte leurs performances, ainsi que leur contenu en plomb toxique qui a un impact négatif sur l'environnement.

Dans ce contexte, cette thèse propose une étude approfondie des pérovskites hybrides à l'échelle atomique pour mieux comprendre leurs propriétés fondamentales. Elle explore également différentes approches pour atténuer les processus de dégradation des pérovskites hybrides et réduire leur toxicité.

Les résultats de cette thèse fournissent un examen détaillé du mécanisme de dégradation des pérovskites hybrides en présence d'humidité et d'oxygène, ainsi que des approches pour limiter cette dégradation. Elle propose également de nouvelles pérovskites moins toxiques et plus efficaces.

Ainsi, cette thèse est organisée en trois sections. La première section décrit les propriétés fondamentales des pérovskites hybrides et présente les défis associés à leur utilisation en tant que matériaux pour les cellules photovoltaïques. La deuxième section explore les mécanismes de dégradation des pérovskites hybrides et propose des approches pour atténuer leur dégradation en présence d'oxygène et d'humidité. Enfin, la troisième section présente de nouvelles pérovskites moins toxiques et plus efficaces pour les cellules photovoltaïques.

En somme, cette thèse représente une contribution significative à la recherche sur les pérovskites hybrides et leur utilisation pour la production d'énergie renouvelable. Elle propose des solutions pour améliorer leur performance et leur durabilité, tout en réduisant leur impact environnemental.

Cette thèse sera organisée comme suit :

La section 1 introduit l'effet photovoltaïque et les paramètres importants nécessaires pour calculer le rendement de conversion de puissance, ainsi que les différentes technologies photovoltaïques disponibles. Nous présentons également dans cette section les cellules solaires à base de pérovskites hybrides, leur synthèse et les méthodes de dépôt utilisées pour leur fabrication. En outre, nous abordons les propriétés des matériaux pérovskites hybrides, en mettant l'accent sur la compréhension approfondie de leur mécanisme de dégradation, les technologies utilisées pour améliorer leur stabilité, ainsi que les progrès de la recherche sur les performances des PSC sans plomb.

Dans la section 2, nous donnons un aperçu de la théorie de la fonctionnelle de la densité et de sa mise en œuvre. Nous présentons l'équation de Schrödinger, qui est la base de toutes les études théoriques des propriétés physiques des matériaux, ainsi que les approximations utilisées pour simplifier cette équation. Nous décrivons également comment le théorème de Bloch en combinaison avec le pseudopotentiel peut être utilisé pour décrire les propriétés du système. Nous introduisons également le code Quantum espresso, qui a été utilisé pour étudier les résultats de recherche de cette thèse.

La section 3 présente les résultats de recherche évalués au cours de cette thèse. L'objectif principal de cette section est de comprendre le mécanisme de dégradation de la pérovskite hybride, d'améliorer et de réduire ses processus de dégradation, et de suggérer de nouveaux matériaux candidats potentiels moins toxiques pour l'application photovoltaïque. Nous présentons dans cette section l'effet du dopage du $MAPbI_3$, ainsi nous montrons une étude détaillée de l'influence des sites vacants et de l'humidité sur la dégradation de la pérovskite hybride. Nous avons également étudié une approche rationnelle pour diminuer la toxicité et augmenter la stabilité de ces composés. Enfin, nous avons fourni la conversion de puissance d'une nouvelle pérovskite prometteuse halogénure de plomb.

La conclusion générale résume les principales contributions de cette thèse en ce qui concerne le développement de nouvelles stratégies pour surmonter les faiblesses de la pérovskite hybride $MAPbI_3$, tels que l'instabilité et la toxicité afin d'améliorer ses propriétés physiques pour mieux s'adapter à l'application photovoltaïque. En perspective, nous prévoyons de travailler sur l'aspect expérimental de ce matériau, ainsi nous prévoyons réaliser un prototype de cellule photovoltaïque dans le future.

Contents

1st section literature review

Chapter I: Photovoltaic from principle to application

Chapter II: Solar cell based hybrid perovskite

3rd section Outcomes of research

Chapter I: Somme approaches for reducing the hybrid perovskite degradation processes

Chapter II: FAPbSnGeX3 as potential candidate for photovoltaic application

1st section

literature review

✉ Faculté des Sciences, avenue Ibn Battouta, BP. 1014 RP, Rabat –Maroc
☎ 00212(05) 537 77 18 34/35/38, 🖷 00212(05) 537 77 42 61, http://www.fsr.ac.ma

First Section-Introduction

Throughout the 19th century, light was considered as a wave, until Einstein came up with his revolutionary theory, which stated that light behaves as a set of particles[16]. This approach given by Einstein has been proven right yet again after the discovery of the photoelectric effect. The photoelectric effect has opened another world to the next set out of the light theory. This effect has been noticed when an electron was emitted from a metal exposed to electromagnetic radiation. The electron emitted is called a photoelectron. Surprisingly, the photoelectron energy showed absolutely no dependence on the radiation's intensity. This phenomenon was explained by Einstein when he defined an equation that relates the quantum of light energy or also the so-called photon energy to the light frequency ν and Planck's constant $\hbar$. The above proved that photoelectron energy depends only on the frequency of light and not on its intensity. The photoelectric effect equation expresses the kinetic energy E_k of a photoelectron emitted from a metal as $E_k = \hbar\nu - w$; where w represents the work function (The energy needed to break through the surface). Thus, the absorbed photon energy above a certain frequency was ascribed as responsible for the emitted electron in the photoelectric effect. Thanks to the photoelectric effect that made the photovoltaic revolution possible. The photovoltaic consists of the direct conversion of light into electricity based on the photoelectric effect. The first photovoltaic cell was introduced by bell laboratories and was patented in 1941[17], since the photovoltaic became the new alternative for fossil fuels. At the beginning solar cells were made out of silicon, this silicon based cells have proven to be a great success in photovoltaics and was able to reach a high efficiency of 25.25%[18]. Silicon-based cells are the most used cells today; they dominate the largest commercial photovoltaic installations. Different parameters impact industrial solar energy projects such as durability, efficiency, and the cost of solar cells. To meet the efficiency cost ratio various architectures and solar cell generations were investigated. To date, four essential generations have been proposed, they consist of crystalline Silicon, thin film, emerged technology, and perovskite based cells. Si, CdTe, CiGs, GaAs, and hybrid perovskite were the main semiconductors used as absorbing materials in these solar cells. Recently, the fourth hybrid perovskite generation has appeared as a new promising material in photovoltaic. Hybrid organic inorganic perovskites materials set a record in the power conversion efficiency of solar cells. Their efficiency has greatly increased in just a few years, making these materials very competitive contenders to silicon. Hybrid perovskite based solar cells

are characterized by their flexibility, their ultra-thin and low-cost photovoltaic cells that show a very promising future for the solar cells industry. Fig.1 depicts the energy conversion efficiencies according to the timeline of solar cell researches since 1976.

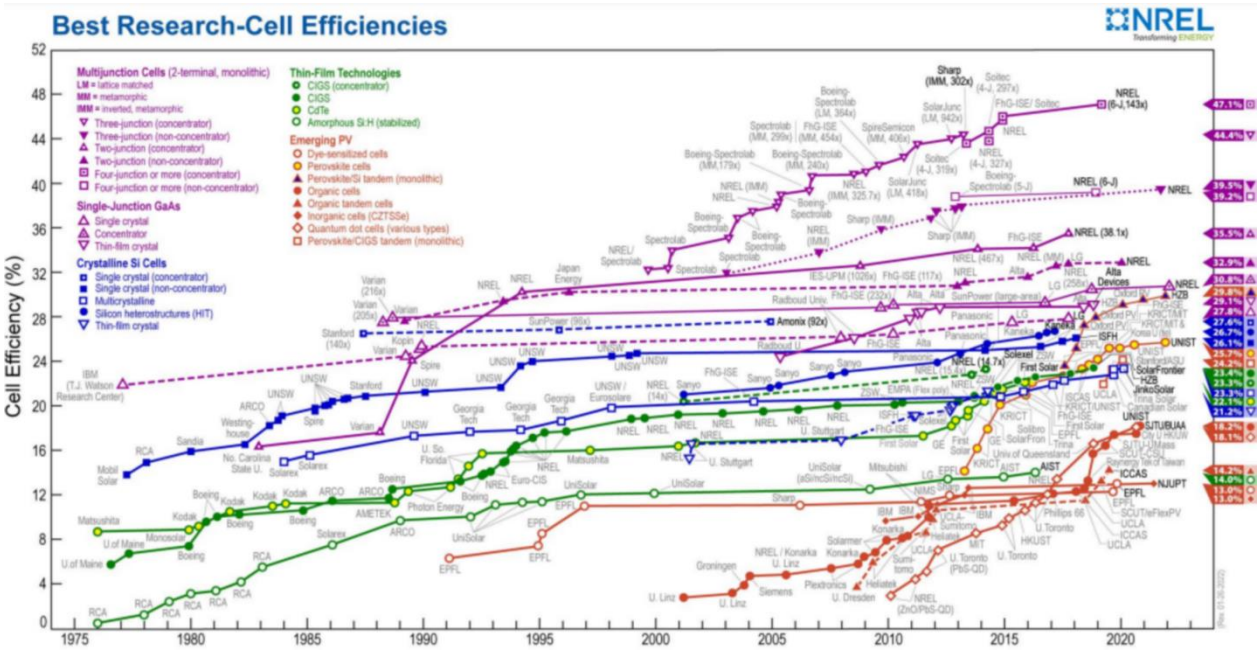

Fig. 1. Reported timeline of research solar cell energy conversion efficiencies since 1976[19]

Chapter I

Photovoltaic from principle to application

I. Introduction

In this chapter photovoltaic effect description as well as underlying working principle of a solar cell are introduced. Definition of the important parameters provided for the power conversion efficiency calculation (Short-circuit current density (J_{sc}), open-circuit voltage (V_{oc}), fill factor (FF) and the incident power from the solar irradiation (P_{sun})) will be given. Furthermore, the different photovoltaic technology and generation are discussed in this chapter.

II. The Working Principle of a Solar Cell

The conversion of the solar radiation into electricity by photovoltaic (PV) devices is a reliable choice to meet the global energy demand. Solar cells or Photovoltaic cells use the photoelectric effect to produce direct current by absorbing solar radiation. The photovoltaic effect allows cells to directly convert light energy from photons into electricity through a semiconductor material that carries electric charges (electrons and holes). The creation of charges will cause the creation of a potential difference at the terminals of the electrodes and of an electric current in a circuit connected to the electrodes. Fig.I.1 shows the operating principle of a photovoltaic electricity generator. The Photovoltaic effect is based on three principal processes:

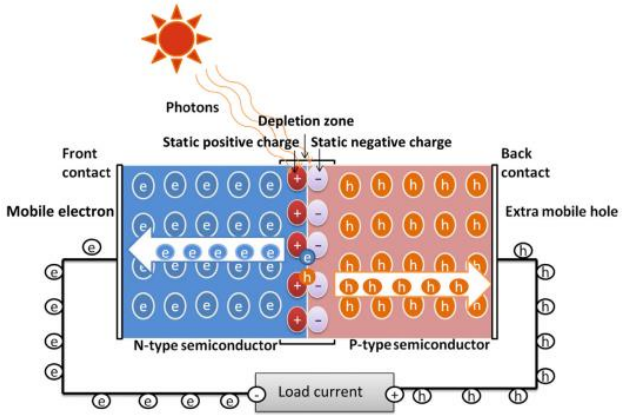

Fig.I. 1. Schematic representation of a simple photovoltaic cell[20].

6. The generation of electron-hole carries due to the absorption of the radiant light coming from sun

The absorption of a photon excites the electron, going from a low energy level E_i to a high energy level E_f where the difference between these two levels represents the energy of the absorbed photon; $E_{Ph}= h\nu= E_f - E_i$. The semiconductor has an almost filled energy bands called the valence band E_v and an almost empty band called the conduction band E_c; the energy difference between this two bands is called energy gap or band gap $E_G= E_c-E_v$, that cannot be occupied by electrons based on quantum theory. If the maximum of the conduction band and the minimum of the valence band occur at the same k-vector, the gap energy is called direct. In the opposite case the gap energy is called indirect. The energy gap is the amount of energy that the electron needs to jump from the valence band to the conduction band. Absorbed photon with a higher energy than the band gap allows the electron to jump across this band to reach the conduction band. When the electron moves to the conduction band, it leaves a vacancy in the valence band. This vacancy behaves like a particle with a positive elementary charge and it is called a hole. Thus, the creation of an electron-hole pair.

7. Charge carrier's separation in the junction

The electron-holes pairs have to be collected before their recombination in the solar cell. The recombination can occur when an electron in the conduction band loses energy and falls back into a hole in the valence band, resulting in the emission of a photon in a radiative recombination, or transferred to other carries inducing the elevation of their kinetic energy in the case of Auger recombination[21]. Recombination can also take place through defects, this recombination is known as Shockley-Read-Hall (SRH) recombination[22-23]. The separation of charge carrier in a solar cell can be made through two mechanisms: diffusion and drift. The diffusion is controlled by the density of the majority carries caused by the density gradient difference, whereas, the drift is driven by an electrostatic field established across the device and it is controlled by the minority carries. Once the carries are separated they are extracted by the electron transport layer (ETL) and the hole transport layer (HTL), and by the end collected by the electrodes[24].

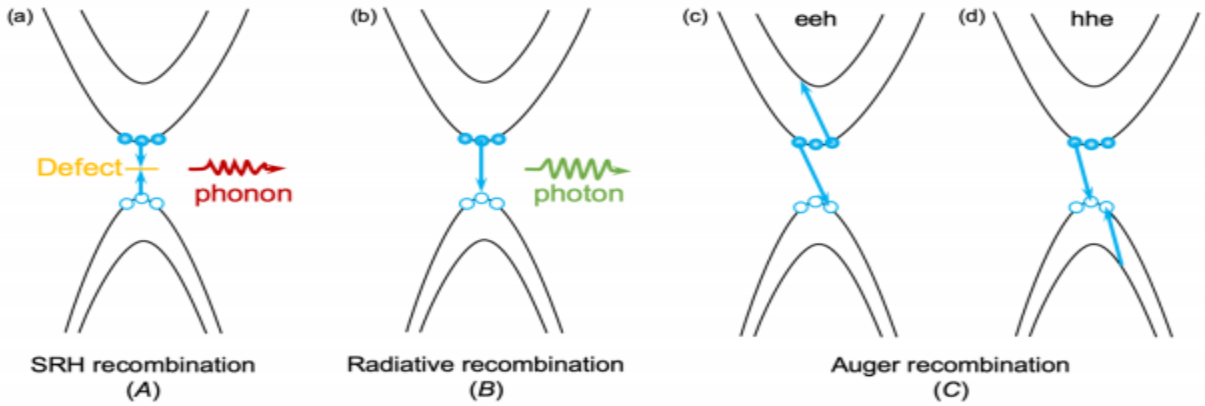

Fig.I. 2. Schematic illustration of different recombination processes: a) Shockley-Read Hall (SRH) recombination, b) Radiative recombination, and c,d) Auger recombination including electron-electron-hole (eeh) and hole-hole-electron (hhe) processes. The light-blue solid and open spheres denote electrons and holes, respectively.

8. Collection of the photo-generated charge carriers

The charge carriers collected by the electrodes can perform work in an external circuit. The movement of the free electron in conduction band is called electron current. Current can also be generated in the valence band by the movement of hole. Electrons in the valence band are not free to move as in the conduction band; however, with a little change in its energy level the valence electron can recombine with a nearby hole leaving a hole in the energy level where it came from. Thereby, a movement of hole from one place to another is established resulting in a hole current in the valence band. Thus, the solar energy is finally converted to electric energy via the photovoltaic effect.

III. External solar cell parameters

The solar cells performances are determined by measuring the power conversion efficiency (PCE). The calculation of the PCE is evaluated using the following equation:

$$\eta = \frac{V_{oc} \times J_{sc} \times FF}{P_{sun}} \times 100 \qquad (1)$$

These important parameters provided for the PCE calculation are the short-circuit current density (J_{sc}), the open-circuit voltage (V_{oc}), fill factor (FF) and the incident power from the solar irradiation (P_{sun}). The solar spectrum received over a certain area on earth changes throughout the rotation of

the earth, geographical location and the inclination angle of the earth's axis. The path length of light is defined by the optical air mass (AM). Fig.I. 3 shows the power of the sun corresponding to the standard spectrum for space applications (AM0), the AM1.5 Global spectrum designed for flat plate modules and the AM1.5 Direct spectrum defined for solar concentrator work. Solar cells can be described by an equivalent circuit containing one diode as represented in Fig.I. 4a where I is the terminal current, I_L is the light-generated current with illumination, I_0 is the saturation current and V is the terminal voltage[25]. The equivalent circuit parameters are the shunt resistance (R_{sh}) and the series resistance (R_s).

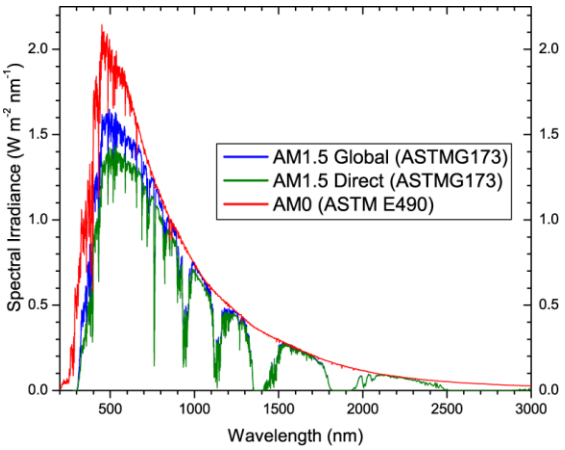

Fig.I. 3. Spectrum of sunlight (sun spectrum) outside the earth's atmosphere (air mass (AM) 0, thick solid line), on earth for a zenith angle of 48.2◦ (AM1.5, thin solid line) and of a blackbody with a temperature of 5800 K (dashed line)[26].

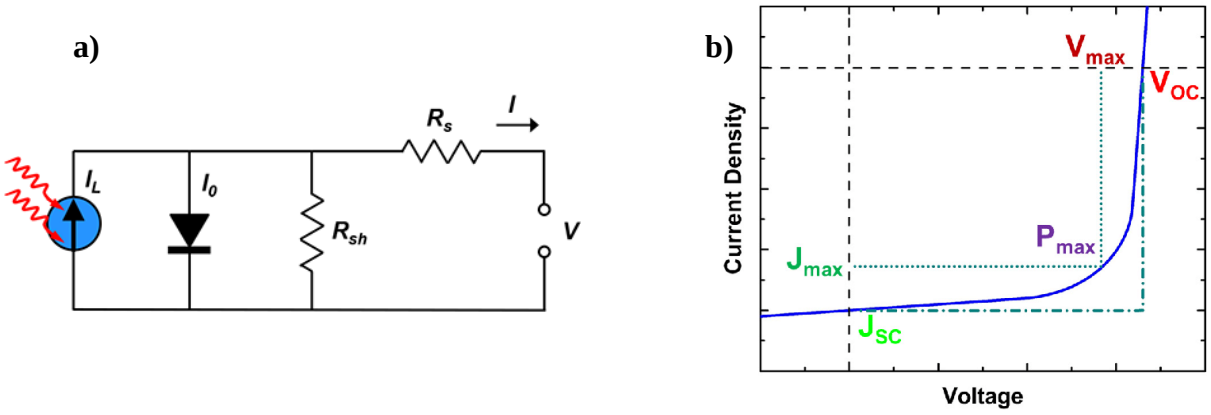

Fig.I. 4. a) Equivalent circuit of a front junction n-type silicon solar cell with parasitic series resistance (Rs) and shunt resistance (Rsh)25, b) Idealized J-V curve for photovoltaic devices[27].

The sun power is converted into electrical power (P) via the solar cell. Electrical power represents the product of electric current (I) and electric potential or voltage (V).

$$P = I \times V \quad (2)$$

When the terminals of the photovoltaic cell are disconnected, the voltage is called open circuit voltage, in this situation the solar cell does not produce any current but solely produce voltage. The open circuit voltage depends on many factors:

- The band gap of the absorber material
- The amount of doping of the doped layers
- The material quality
- The light generated current density
- Temperature

Once the electrodes of the solar cell are short circuited, the illuminated solar cell will produce only a current and no voltage will be produced. This current density is called the short-circuit current and it depends also on a many factors:

- Incident light intensity
- The spectrum of the incident light
- Optical properties

- Collection probability

The diagram represented in Fig.I. 4b demonstrates the relation between voltage and current generated by an illumination[27]. Solar cells achieved the best performances in the maximum power point (P_{max}). P_{max} represents the product of the current density maximum and the maximum voltage. The ratio of the maximum power and the product of V_{oc} with J_{sc} represents the fil factor (FF).

$$FF = \frac{V_{max} \times J_{max}}{V_{oc} \times J_{sc}} \quad (3)$$

Thus, the fill factor is also an important parameter to determine the efficiency of photovoltaic module. To ensure the maximum possible efficiency, the FF should be maximum and approaching to unity on the I-V curve of the photovoltaic module. Therefore, the FF can be reduced by the impact of a parasitic resistance[28]. The most common parasitic resistances are series resistance and shunt resistance represented in the equivalent solar cell circuit by R_s and R_{sh} (Fig.I. 5a). The shunt resistance or also named parallel resistance is caused by macroscopic defect in the solar cell. Shunt current can cause the heating of the solar cell leading to the hotpots in the module[29]. Series resistance are mainly the sum of contact resistance on the front and back surfaces and the ohmic resistances of the bulk and the diffused layers on the front (and back) sides[30]. Solar cells can have additional recombination losses and optical losses such as light transmission and reflection. These losses can be evaluated from the external quantum efficiency (EQE) which represent the ratio of the electron number collected as photocurrent to the number of photons incident to the solar cell[31]. The EQE is related to the short circuit current density by the following formula:

$$J_{sc} = \int_{E1}^{E2} \Phi(E) EQE(E) dE \quad (4)$$

IV. Solar cells evolution

The major challenges in the photovoltaic technologies have always been converting and storing solar energy in an efficient, cost-effective and environmentally friendly manner. Light shining on the solar cell produces both a current and a voltage to generate electric power. This process requires, an active semiconductor material that plays the role of absorbing layer in the solar cell. The first material used as an absorber was crystalline silicon which has dominated the photovoltaic (PV) market for the past half century. The high manufacturing cost of crystalline silicon PV has negatively impacted the PV industry. A lot of efforts have been established to broaden the absorbed

solar spectrum. In this order, different solar cells architectures are proposed. Furthermore, PV technologies can be classified by many factors as typically the photovoltaic cell (PVC) efficiency, active materials used, and manufacturing complexity and cost. In order to optimize the cost/watt of delivered solar electricity and efficiency of solar cells, the above evolved since the discovery of the photovoltaic to reach four generations (Fig.I. 5). Comparison between materials complexity and efficiencies demonstrated by these different generations are depicted in Fig.I. 6.

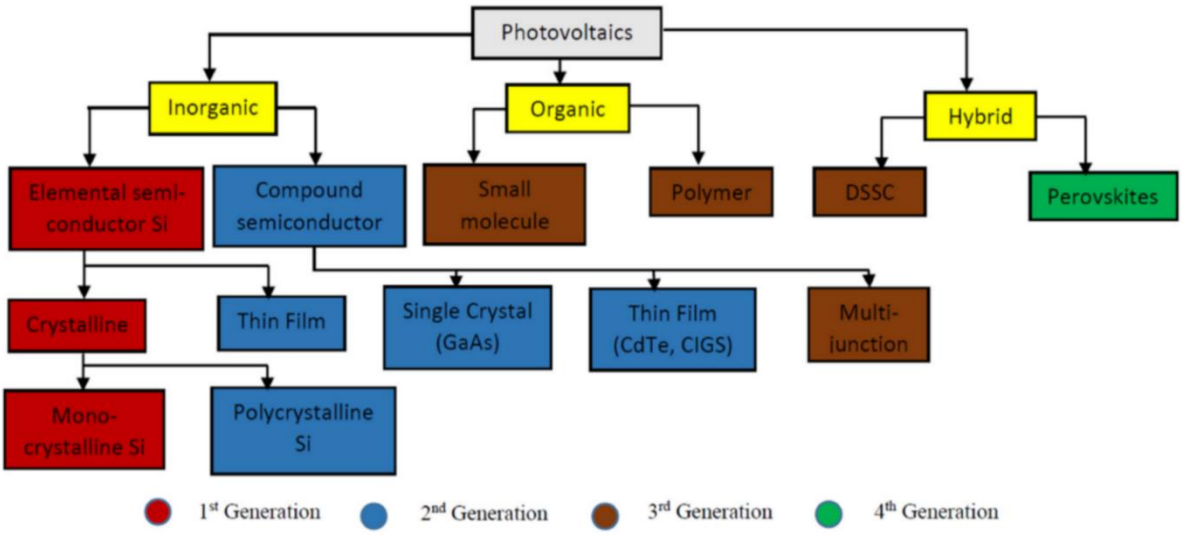

Fig.I. 5. Evolution of photovoltaic solar cells[32].

1. First Generation of Solar PVC-Crystalline Silicon

The first generation of solar cells technology has been developed in 1958[33]. Crystalline Silicon constituted this first generation formed by a p-n junction. This p-n junction is formed by sandwiching two layers of Si semiconductor material types, namely n-type Si semiconductor layer and p-type semiconductor layer. The n-type or p-type silicon are established by doping silicon with impurity atoms such as boron or phosphorus, thus changing their electronic properties. The solar PVC based on monocrystalline silicon material have widespread the world and dominated the largest commercial PV installations, meanwhile their production cost reminds expensive and it required a relatively thick absorber layer due to its indirect character of electron transitions. The largest high efficiency pronounced by monocrystalline silicon to date has attend 25.25%[34] . In order to reduce the production costs of solar PV cells, the polycrystalline silicon was developed and investigated since the mid-1970s[35]. The difference between the monocrystalline and polycrystalline silicon appears in the production mechanism of the solar cell. Monocrystalline solar cells are cuts

from a single pure crystal of silicon, instead of the polycrystalline solar cells that are composed of fragments of silicon crystals melted together in a mold before being cut into wafers[36]. The production of polycrystalline cell modules is more economical, however, it presents a low efficiency rantings regarding the monocrystalline solar cells.

2. Second Generation of Solar PVC – Thin films

Thin films solar cells were proposed for the same reason of reducing the production costs and rising the efficiency of cells. This generation used less expensive material with a less thickness of 1–10 µm[37]. Copper indium gallium selenide (CIGS), cadmium telluride (CdTe), and amorphous silicon (a-Si:H) were used as an active semiconductor material in this second generation. Contrary to silicon, these semiconductor materials present a direct band gap that reduce energy losses, rise the absorption coefficient thus harvesting more photons from the sun. The record efficiency, to date, for a-Si:H, CIGS, and CdTe are 13.4%, 22.5%, and 22.1% respectively[38]. These materials have also prone to produce lower greenhouse gas emissions during production and use than c-Si PV[39]. However, the manufacturing of thin-film solar cells represents more complexity than C-Si which makes them more challenging. Improving the efficiency of solar thin films and reducing their manufacturing complexity remains a challenge for future thin film-based photovoltaics.

3. Third Generation of Solar PVC – Emerging technology

Solar cell technologies based on the third Generation have shown a potential for large scale deployment in the future[40]. The big advantages of these solar cells is that they can be produced very cheap, in a variety of colors, they are flexible, and transparent. The shifting to organic solar cells in this generation allowed to exceed the maximum light conversion coefficient in semiconductor systems termed as Shockley-Queisser limit[41] (which is around 32% for an optimal bandgap value of 1.2–1.3 eV). These categories of solar cells include multi-junction or tandem structures, polymer, and dye-sensitized solar cells (DSSCs). The first heterojunction has been reported in 1986 with an efficiency of 1%, consisting of two semiconductors in a bilayer architecture solar cell[42]. Multi-junction (tandem) solar cells comprised multiple light absorbers with considerably different band gaps designed to absorb the entire range of the solar light[43]. A high efficiency confirmed for multi-junction structure has so far reached 47%[44]. In the other hand, compared to traditional cells, the producing of dye-sensitized solar cells is considered as a new paradigm for the low-cost and high-efficiency solar cells. Dye-sensitized solar cells (DSSCs)

convert sunlight into electricity using an electrolyte through electron injection of excited dye molecules into a wide band gap of semiconductor[45]. In 1991, using TiO_2 as semiconductor material Grätzel invented a DSSCs with an efficiency of 7%. The performances of DSSCs depend on dye molecules used as photosensitizers due to dyes photo-excitation.

4. Fourth Generation of Solar PVC – Perovskite

In 2009, Kojima et al have introduced the organic-inorganic lead halide perovskite compounds as visible-light sensitizers in photoelectrochemical cells[46]. They achieve an efficiency of 3.8%. Changing the Electrolyte Formulation and perovskite deposition method by Hyeok Im et al was able to increase the performance and stability of the perovskite device to a yield of 6.5%[47]. However, hybrid perovskite sensitized solar cell dissolved gradually into the redox electrolyte giving a rapid decrease in energy production over time. To relate, they substituted the liquid electrolyte with a solid hole conductor (or hole transport material, HTM), yielding a PCE of 9.7%[48] and since, the hybrid perovskite solar cells have become a key challenge toward the evolution of solar PVC technologies called “fourth-generation solar cell”. These solar cells demonstrated remarkably high efficiencies, and high open-circuit voltages (Voc), also they offer great potential for low costs of production. Nevertheless, the fourth-generation solar cell remains a part of research in the laboratory that is still not yet commercialized.

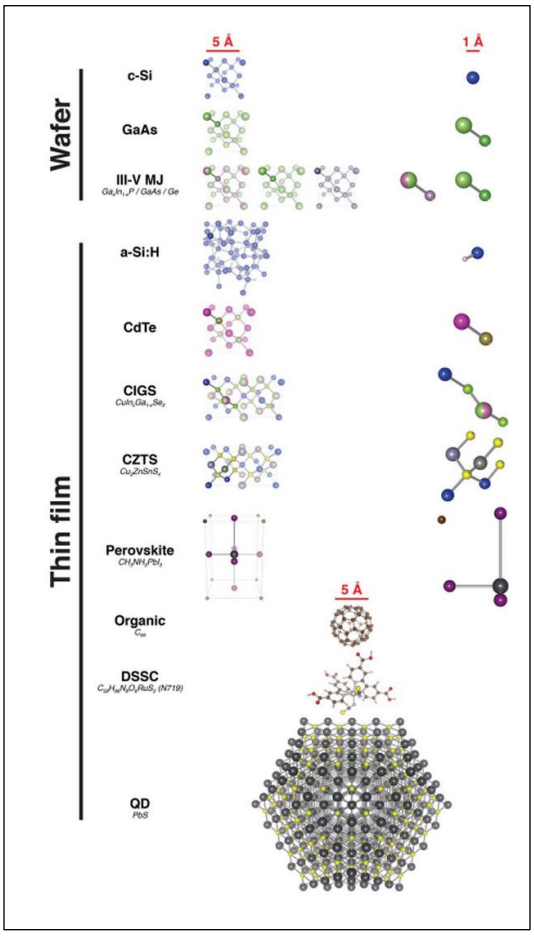

PV Technology		Cell Conversion Efficiency	Module Conversion Efficiency
Crystalline	Monocrystalline silicon (Si)	27.6%	24.4%
	Multicrystalline Si	23.3%	20.4%
	Multi-junction Gallium arsenide (GaAs)	47.1%	38.9%
Thin film	Cadmium telluride (CdTe)	22.1%	19.0%
	CIGS	23.4%	19.2%
Emerging	Perovskite	25.5%	17.9%
	Organic	18.2%	11.7%

Fig.I. 6. a) Material complexity of various materials in solar PVC[49]. b) PV Technology Types and Efficiencies[50].

Chapter II

Solar cell based hybrid perovskite

I. Introduction

The aim of this chapter is to introduce a detailed description of hybrid perovskite material. For this purpose, firstly we give a description of solar cells based hybrid perovskite as well as the synthesis, and deposition method used for their fabrication. The hybrid perovskite material properties, their different structure, and the important effect of the organic molecule on the structure performance will be discussed also in this chapter.

II. Hybrid Perovskite Solar Cells Structure

Photovoltaic solar cells based on hybrid perovskite are mainly constituted of five essential layers. Firstly, the most important element is the hybrid perovskite absorbing layer, sandwiched in between the electron transport layer (ETL) and the hole transport layer (HTL). The sequence of HTL and ETL defines the device architecture[51]. When light penetrates the device through the ETL that is deposited above the hybrid perovskite material, the structure is called n-i-p. While in the inverse arrangement it is defined as p-i-n structure. Here p, i, and n define the HTL, perovskite layer, and the ETL respectively. These transporting layers are localized between two electrodes front contact (FC) and back contact (BC) as shown in Fig.II. 1a. Unlike silicon-based solar cells, perovskite layers do not need to be doped to allow charge exchange and the production of an electric current. The absorption of photons in hybrid perovskite leads to excitons creation (electron-hole pairs) in the heart of the material. The ones on the surface are transported with the HTL and ETL then they join the electrodes, which leads to the production of an electric current. In 2012, and for the first time Etgar et al synthetized a mesoporous $CH_3NH_3PbI_3/TiO_2$ heterojunction and they demonstrated that $CH_3NH_3PbI_3$ can play the role of both light harvester and hole transporter in the PVCs[52]. On the other hand, Lee et al investigated a meso-superstructured $CH_3NH_3PbI_3/Al_2O_3$[53]. They noticed that its efficiency is comparable to that of TiO_2 even though Al_2O_3 shows a wide band gap that will not allow it to extract electrons from the hybrid perovskite. Through these results researchers realized that the hybrid perovskite itself carried the electrons to the collector electrode. In this context, a paper has been published demonstrating that the charge carrier mobility in hybrid

perovskite depends on different parameters such as the organic's cation orientation and the octahedral symmetry of the inorganic part[54]. Perovskite solar cells can be either mesoporous perovskite solar cells or planar perovskite solar cells[55]. Structures depicting both configurations p-i-n, and n-i-p mesoscopic/planar PSC of the device are shown in Fig.II. 1b. Mesoporous p-i-n solar cell structure based on hybrid perovskite was the first to be produced cell among a variety of perovskite cells that were constructed using TiO_2 as a hole-conducting material. It has various advantages namely, a much lower cost and an easier fabrication method[48]. The development of this photovoltaic device has consequently led to the appearance of new planar architecture. The high efficiency of this planar perovskite solar cell can be achieved by controlling the interfaces between the different layers making up the PSC and by varying the electron/hole transporting materials[56]. Nevertheless, planar architectures suffer more than mesoporous devices from the hysteresis behavior. The diminishment of this anomalous behavior is essential for fabricating long-term stable PSCs[57]. In particular, Heo et al were able to fabricate an inverted planar architecture of ITO/PEDOT:PSS/$MAPbI_3$/PCBM/Au offering less hysteresis behavior with a high efficiency[58]. Besides, a key success for the further improvement of the efficiency and long-term stable hybrid solar cells is the development of various synthetic and film deposition techniques to control the morphology and crystallinity of hybrid perovskites.

a)

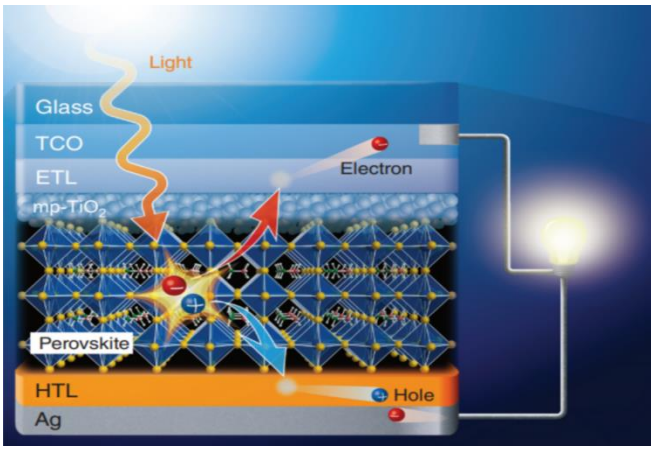

b)

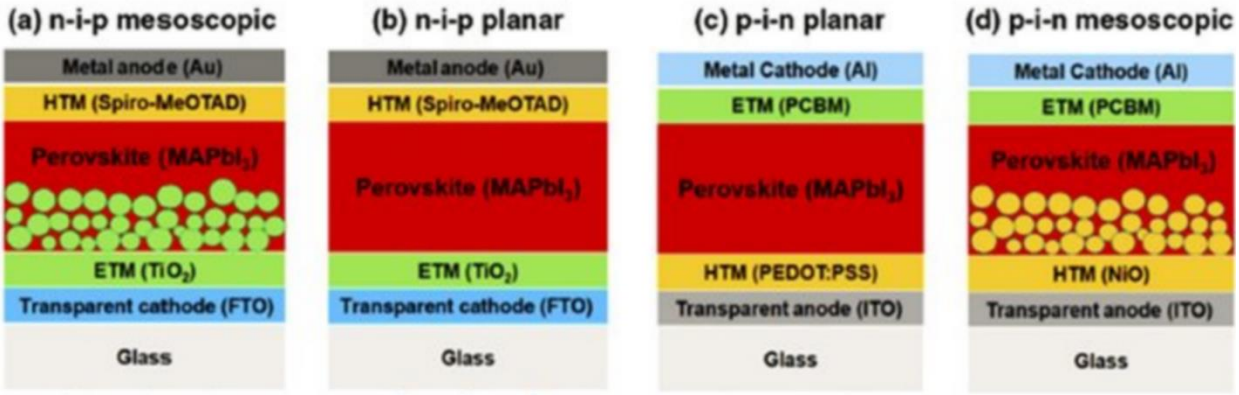

Fig.II. 1. a) Operation of a hybrid perovskite solar cell consisting of a glass/transparent conductive oxide (TCO)/electron transport layer (ETL)/mesoporous TiO_2 (mp-TiO_2)/ perovskite layer ($CH_3NH_3PbI_3$)/hole transport layer (HTL)/metal electrode (Ag)structure[59], b) Schematic showing the layered structure four typical of perovskite solar cells[60].

III. Hybrid solar cells Fabrication

The synthesis, as well as the deposition of hybrid perovskites, are very important elements for the device performance and stability-enhancing as well as increasing the efficiency of the solar cell. Synthesis of hybrid perovskites is simple and less expensive compared with the synthesis of III-V or II-VI inorganic semiconductors. It is done by a soft chemistry at room temperature and is relatively unrestrictive[61]. One-step or two-step deposition process can be performed for the hybrid perovskite fabrication as depicted in Fig.II. 2. To obtain 3D perovskites involving the one step method, the ammonium salt CH_3NH_3I and the inorganic salt PbI_2 will be dissolved, then the solution is followed by spin coating to form the molecular crystal[62]. For $CH_3NH_3PbI_3$ perovskite, the solvent used is γ-butyrolactone or dimethylacetamide[63]. However, this approach generally leads to uncontrolled morphological variations, which resulted in low reproducibility of photovoltaic performance. To achieve better control of crystal formation and growth, a sequential deposition method based on the two step coating was developed[64]. Lead iodide PbI_2 was first loaded by spin coating dimethylformamide on the mesoporous titanium dioxide film and then exposed to a solution of CH_3NH_3I in isopropanol; after annealing the solution, the formation of the final perovskite pigment which penetrated the porous TiO_2 film is obtained. Furthermore, hybrid perovskite layers can also be created using MA gas as precursor[65]. In this process CH_3NH_2 gas in the presence of H_2O from air are exposed to a pristine PbI_2 thin film, resulting in the reaction of the MA molecules with the PbI_6^{4-} octahedral forming a high-quality, uniform $CH_3NH_3PbI_3$[66]. For mixed halide hybrid perovskite, solvothermal synthesis method is highly advised as an approach for easy synthesis of this type of hybrid perovskite[67]. Further, the fabrication process of hybrid perovskite PVCs can be involved based on other techniques including, vapor assisted, solvent engineering, hot casting, and direct dropping. Recently, the synthesis of high-quality organic-inorganic hybrid perovskite films using green solvent engineering has been adopted for a safe environment[68]. The vapor assisted synthesis method can help to achieve a steady enhancement of perovskite solar cells performance by a complete covering of the surface to avert low-resistance shunting paths between the n and p type contacts[69]. Low-pressure vapor-assisted technique is used also in the formation of the multidimensional 2D/3D organometallic halide perovskite[70]. The presence of defects states in hybrid perovskite films affects the stability of the device which, in return, affects the growth of the power conversion efficiency. Future studies on the synthesis

process of this material have to provide essential regard to the defect states and grain-boundary passivation of hybrid perovskite films for high-performance heterojunction solar cells.

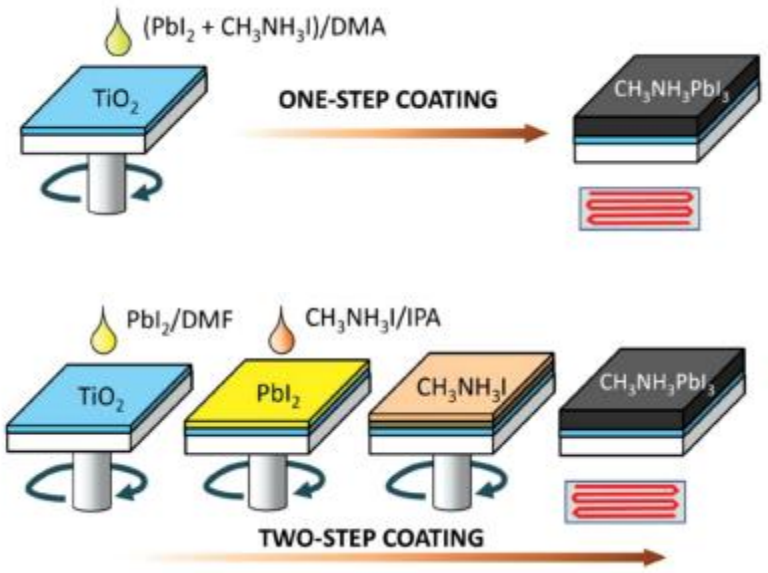

Fig.II. 2. One-step deposition and two-step deposition of solution processing technique[62].

IV. Hybrid perovskite

Hybrid perovskites materials are considered as the most promising materials for the new PV generation[71]. These materials benefit from a high absorption coefficient, suitable bandgap matching the solar spectrum, long carrier lifetime and diffusion length, low cost manufacturing[72-73-74]. The unique features and properties of hybrid perovskite encourage the continuous research and development of hybrid organic inorganic perovskite (HOIP) solar cells which has led to the rapid growth of their efficiency. A high efficiency of 25% has been assigned for HOIP solar cells within a few years, an efficiency that took 25 years for silicon solar cells to reach this level[75]. Additionally, the strong HOIP absorption coefficient allows the use of a thinner layer compared to other organic semiconductor materials. The hybrid perovskites systems are so far more complicated than the CiGs, Si and other materials used in PVC application. Organic-inorganic hybrid perovskites are organized in an ABX_3 structure (A= MA (CH_3NH_3), FA ($CH(NH_2)_2$), Cs; B= Pb, Sn, Ge, Be; X=

I, Br, Cl) where A represents the cation organic, B the metal cation, and X the anion halogen. The inorganic octahedra BX_6 forms a cage framework that encloses the A-site cation. To keep the stability of the 3D ABX_3 perovskite structure, the Goldschmidt tolerance factor (t) has to conform the $0.8 < t < 1.0$, where $t = \frac{r_A + r_X}{\sqrt{2}(r_B + r_X)}$ is calculated from the ionic radii (r_i) of each ion (A, B, X)[76]. At the time of the temperature's increasing, orthorhombic- tetragonal-cubic phase transition occurs for lead halide perovskite[77]. At a high temperature, in cubic phase the organic molecule can freely rotate under the framework as depicted in Fig.II. 3. The hybrid perovskite solar cells have shown a large interest in different applications. The use of this new generation materials in the building-integrated photovoltaic (BIPV) is a fascinating approach that can be exploited by the current and future generations[78]. This integration replaces the traditional building envelopes such as windows, roofs, walls and offset building construction cost[79]. These new BIPV envelopes generate power and also protect the building interior from harsh external ambient. The possibility to extend the use of perovskite in different application categories is one of particularly relevant aspects of this class of material. This is established by tuning the physical and chemical hybrid perovskite properties by changing or mixing different elements in perovskite materials[80-81].

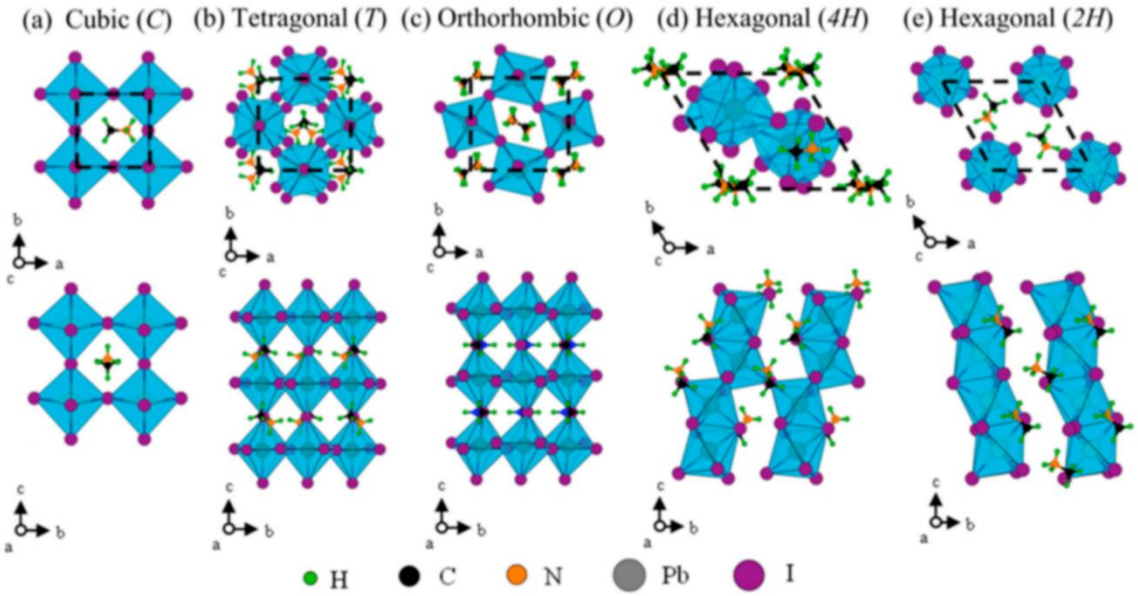

Fig.II. 3. Crystal structure of (a) cubic (C), (b) tetragonal (T), (c) orthorhombic (O), (d) hexagonal (4H), and (e) (2H)-phases of MAPbI3. The top and bottom panels represent [001] and [100] crystallographic directions, respectively[82].

V. Structural transition in hybrid perovskite

The nature of organic cation in hybrid perovskite plays a sensitive role in identifying the crucial properties of these materials[83]. The latter are also effected by varying the corner-sharing, face-sharing and edge-sharing between the inorganic part and the organic molecule[84]. Also, the displacement of the B cation from the center of the octahedron BX_6 causes the loss of the symmetry elements. Depending on the temperature, hybrid perovskite can exhibit a diversity of structural phase transitions. At the high temperature of 350k the $MAPbI_3$ crystalizes in a cubic phase and it adopts the P4mm space group where lead atom displacement occurs along the tetragonal c-axis[85]. The transition from 350K to less of 300K causes $MAPbI_3$ structure to turn from a cubic phase to a tetragonal phase during which it adopts the I4cm space group and shows an out-of-phase tilting of the polyhedron. At the low temperature of 165 K, $MAPbI_3$ undertakes again a first-order phase transition into the orthorhombic phase with a Pnma symmetry, where the MA molecules follow a certain shape order, and the PbI_6 cage shows a tilting in all the three spatial directions[86]. These tilting of the PbI_6 cage was described in literature by Glazer notation which was used as a tool to express in-phase and out-of-phase tilt of the octahedral BX_6[87]. The in-phase tilt, out-of-phase tilt or no tilt are represented by the notation "+","-"and "0" respectively. When the tilt angles around multiple axes are the same, the tilts are represented by the same letter. Tetragonal phase of $MAPbI_3$ (see Fig.II. 3b) denoted as $a^0a^0c^-$, shows a tilting in out-of-phase around the c axes (expressed by the minus sign c^-) and no tilting in both the a and b axes (expressed by the 0 sign a^0), whereas their orthorhombic phase (see Fig.II. 3c) is denoted by $a^-b^+a^-$, indicating an in-phase rotations in the b axes (b^+) and out-of-phase rotations in both a and c axes (a^-)[88]. One of the common tilting patterns in the cubic phase of $MAPbI_3$ is induced by the imaginary phonon modes at the gamma and the R points of the Brillouin zone and it is attributed to the antiferrodistortive distortion (AFD)[89]. The substitution of the cation organic MA with the larger molecule FA also undergoes a phase transition with the effect of temperature. Multiple discussions about the $FAPbI_3$ structural phase transition have and are still taking place in the present time. The first phase reported by Stoumpos et al. showed a trigonal p3m1 α–$FAPbI_3$ at 293k[85], while subsequent studies using the neutron powder diffraction discerned a black cubic α–$FAPbI_3$ phase structure belonging to the Pm3m space group where the Pb cation represents an ordering[90-91]. A phase transition from the cubic α to the tetragonal β occur at 151 K, showing a distortion of octahedral in the in-phase mode with $a^0a^0c^+$ Glazer notation adopting the P4/mbm symmetry[92]. Furthermore, β–$FAPbI_3$ undergoes a phase transition

to the γ- $FAPbI_3$ maintaining the same symmetry with a discontinuous change in the structure parameters. The determination of the $FAPbI_3$ symmetry by both neutron and synchrotron X-ray diffractions have demonstrated a tetragonal P4bm at 140K[93]. Nevertheless, by neutron diffraction, Chen et al. have obtained a P_{63}/mmc hexagonal structure for a deuterated $FAPbI_3$ at 220 K while at 15K, an hexagonal phase with P_{63}/m space group was obseved[94]. Mixing the FA and MA cations is noted to successfully form the α–$FA_{1-x}MA_xPbI3$[95]. The cubic lattice parameters increase with the incorporation of the FA cation in the $MAPbI_3$ system, this A-site cation mixture improves the stability of the mixed phases $FA_xMA_{1-x}PbI_3$ compared to the pure $MAPbI_3$.The lattice parameters of both $FAPbI_3$ and $MAPbI_3$ at different temperature are regrouped in table.II. 1.

Table.II. 1. Lattice parameters of both $FAPbI_3$ and $MAPbI_3$

	Phase	Temperature	a (Å)	b (Å)	c (Å)	Space group
	Cubic[85]	**400 K**	**6.31**	**6.31**	**6.32**	**P4mm**
$MAPbI_3$	**tetragonal**[85]	**293 K**	**8.85**	**8.85**	**12.64**	**I4cm**
	orthorhombic[96]	**150 K**	**8.82**	**12.68**	**8.60**	**Pnma**
	α–trigonal[85]	**293 K**	**8.98**	**8.98**	**11**	**P3m1**
$FAPbI_3$	**α–cubic**[90]	**> 328 K**	**6.36**			**Pm3m**
	β–tetragonal[92]	**151 K**	**8.89**	**8.89**	**6.30**	**P4/mbm**
	γ- tetragonal[92]	**91 K**	**8.87**	**8.87**	**6.27**	**P4/mbm**
	cubic[94]	**293 K**	**6.38**			**Pm3m**
D-$FAPbI_3$	**hexagonal**[94]	**220 K**	**8.62**	**8.62**	**7.94**	**P_{63}/mmc**
	hexagonal[94]	**15 K**	**8.51**	**8.51**	**7.95**	**P_{63}/m**

D-$FAPbI_3$ demonstrates the deuterated $HC(ND_2)_2PbI_3$ that contains a heavy hydrogen denoted D (deuterium) or ^2H

VI. Orientation of organic molecule in $APbI_3$

At room temperature, the cations organic in hybrid perovskite are free to rotate, causing the orientational disorder and polarization in the system. It has been shown that the organic dipole orientation in both $MAPbI_3$ and $FAPbI_3$ are the source of polarization associated to the ferromagnetic character present in hybrid perovskites[97-98]. The rotation of the organic cation allows to establish different bonds between iodine and hydrogen atoms with different lengths. This bonding is the main cause of the octahedra BX_6 tilting[99]. The nature of MA-I bonding, it's length and the amount of bonds, play a decisive role in identifying the physical properties of hybrid perovskite. When no hydrogen iodine bonding is formed, the $MAPbI_3$ remains untitled at all temperatures, this high symmetry structure does not show any band gap. Thus, tilting of the halide frame has an accurate effect on the optical band gap and carrier effective masses[88]. Hybrid perovskite can also undergo a phase transition by the effect of octahedral tilting[100]. Chandrappa et al studied the relation between tilting of BX_6 octahedra and barrier ion migration in hybrid perovskite. They showed that lower migration barrier results from the decline in the energy of hybrid perovskite provided through the octahedral rotation[101]. For the $MABX_3$ compounds, the organic cation MA represents an asymmetric charge distribution leading to a net dipole moment[102]. The dipole moments calculated in Debye for both FA and MA show a value of 2.29 D and 0.21 D respectively[103]. Due to its dipole moment MA cation's dielectric properties become strongly dependent on temperature. In comparison with $FAPbI_3$, due to the low effective radius of the organic MA and to compensate the space filling between the organic and the inorganic part, $MAPbI_3$ shows larger tilting of PbI_6 frame. MA cation (CH_3NH_3) can move freely under the PbI_6 frame where the CH_3 rotation is induced by the rotation of NH_3 via the torsion potential[104]. The organic molecule FA in hybrid perovskite can rotate around two axis of rotation (Fig.II. 4), the preferential one (φ) is along the line connecting the two nitrogen atoms (the almost rotation that occur at room temperature). The second axis of rotation is the sum of the two C-N bonds θ and it takes place at high temperature[105]. Kanno et al. through the potential energy surface (PES) examination noted that the organic FA orientation represents a strong anisotropy and can rotate freely around φ-axis contrary to the θ -axis[106]. In their study they explain that the strong anisotropy is due to the diminution of the number of hydrogen bonds with the iodine in the cage of the PbI_6 which is caused by the reorientation of FA cation. In their research, Karthick and all showed the

structural parameters variation function of the 12 possible orientation of FA in the pseudo-cubic $FAPbI_3$[107]. Hydrogen-iodine bonds in both $MAPbI_3$ and $FAPbI_3$ are shown in Fig.II. 4.

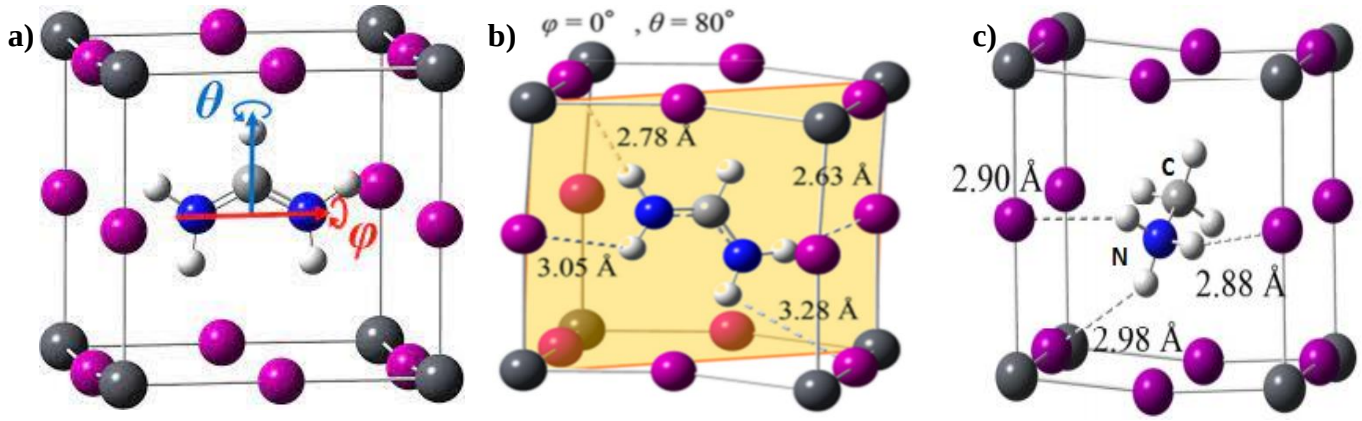

Fig.II. 4. a) FA orientation in cubic $FAPbI_3$[106], b) H-I hydrogen bonds in the $FAPbI_3$ structure at φ = 0°and θ = 80°, c) H-I hydrogen bonds in the $MAPbI_3$ structure[108]. White, gray, blue, purple, and black spheres represent H, C, N, I, and Pb atoms, respectively.

Chapter III

Degradation, toxicity of perovskite and technical solution

I. Introduction

Hybrid perovskite suffer from a degradation in different environmental conditions. The above adding to toxicity are the underlying drawbacks that block the commercialization of these materials. In this chapter we give a deep understanding of the mechanism degradation of hybrid perovskite material as well as we introduced some technology used to improve the perovskite solar cells stability. Research progress summary on the performance of lead-free PSCs will be also provided in this chapter.

II. Degradation of hybrid perovskite under different environmental conditions

The commercialization of hybrid perovskite has been facing many constraints such as their degradation under humidity, in the presence of ultrat violet (UV), and Oxygen. To understand the reason of this degradation an examination at the atomic level may be necessary. Ion migration in hybrid perovskite are believed to be the most important reason of the degradation of this material. This degradation can be identified in the $MAPbI_3$ perovskite by the change of the films color from the dark brownish to yellow. This decomposition can also take place through the statistical formation of molecular defects with a non-ionic characters, whose volatility at surfaces should break the thermodynamic defect equilibria[109]. Different pathways degradation can be possessed for hybrid perovskite depending on the environmental conditions, resulting in several degradation products. These pathways can be assigned as irreversible or reversible degradation reactions[110]. The crystallinity and quality of hybrid perovskite films have in turn proven to affect the stability of this compound. Various methods have been employed to investigate the degradation mechanisms of hybrid perovskite under different environmental conditions. Hence, the important external factors that are responsible for triggering the perovskite's degradation will be discussed in what follow.

1. Degradation of hybrid perovskite in moisture

By the presence of water molecules, the bonding interactions between organic and inorganic parts in the hybrid perovskite can easily be destroyed resulting in a significant decline of the solar cell performance. Lu el Al have demonstrated that no matter what the initial position or the orientation

is of the water molecule, it can be adsorbed in the corner of Pb-I square[111]. They demonstrated also that the adsorption energy and the migration energy barrier of adsorbed water from the surface to another decreases with the increase of the Pb-I-Pb angles. Numerous studies have been focused on the degradation mechanism of hybrid perovskite in water and contradictory observations have been reported. Leguy et al show that a single crystal $MAPbI_3$ exposed to 70 % relative humidity demonstrates a monohydrated phase at the first stage followed by a dehydrated phase. They believed that when exposed to water vapor, hydrated crystal $MAPbI_3$ phases changes are fully reversed when the material is subsequently dried contrary than when it is exposed to liquid water[112]. However, the monohydrated $MAPbI_3 \cdot H_2O$ phase results from the interaction between MA and H_2O through hydrogen bonding, where H_2O and MA are locked to each other[113]. Surprisingly, it has been discovered that the reversibility decomposition of $CH_3NH_3PbI_3$ is due to the fact that CH_3NH_3I is stable in water. Therefore, the hydrogen bonds are shown to initiate the decomposition of this hybrid perovskite[114]. As reported by Wang et al, the interaction between H_2O and CH_3NH_3 breaks down the N−H−I bonds, this hydrogen bond perturbation breaks the $CH_3NH_3PbI_3$ structure, which turns it into a PbI_2 fibrous and CH_3NH_3I. Secondly, CH_3NH_3I reacts with OH^- in water, forming CH_3NH_2 and HI gas, making the water slightly acidic. Contrary to the previous reports, Zheng et all found that the ion I^- of the CH_3NH_3I-terminated surface triggered the initial step of the $CH_3NH_3PbI_3$ dissolution[115]. The dual synergy between the trapped electrostatic charges and humidity in hybrid perovskite are discovered also to trigger the irreversible degradation of this compound[116]. Most recently, the precursors used in hybrid perovskite fabrication are found to improve the stability against moisture degradation[117]. Here Fig.III. 1 shows the positives effects and negative effects of water on PSCs[118].

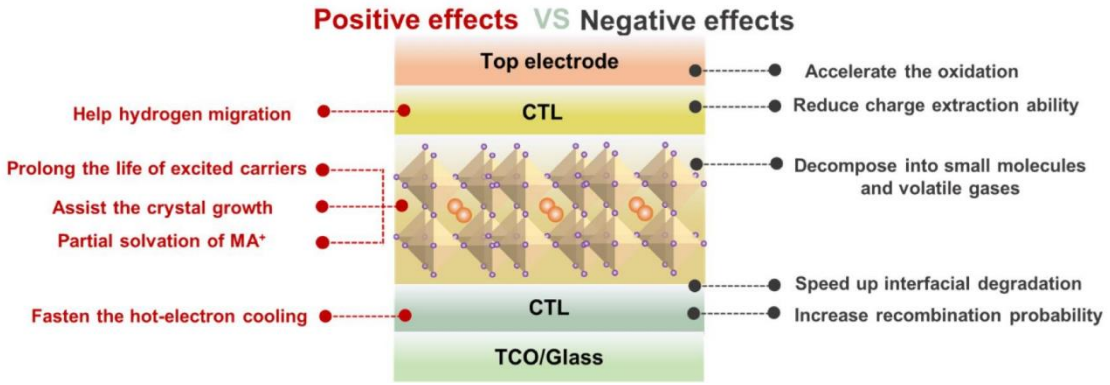

Fig.III. 1. Positive and negative effects of water on PSCs[118].

2. Degradation of hybrid perovskite induced by oxygen

Organic inorganic hybrid perovskites can undergo a chemical reaction with oxygen resulting in their fast degradation. Oxygen interacts differently with hybrid perovskite systems. Reported study showed that oxygen in hybrid perovskite remains near to the surface regardless of the net charge, and the degradation arises along the grain boundaries[119]. In the presence of both oxygen and trapped charge, the crystal structure demonstrates a disruption, and the I–O, Pb–O, and O–O bonds show a chemical interaction. This results have been also confirmed by Zhidkow et al where they demonstrate that hybrid perovskite undergoes a photochemical degradation due to the oxidation of lead atoms that chemically interact with oxygen[120]. In particular, the crystallinity of hybrid perovskite films is prone to define the yields of superoxide formation in the structure[121]. In general, different results have shown that the decomposition of this compound under the effect of the oxygen can take place only on presence of light[122-123] . The incorporation of oxygen into the lattice is strongly enhanced under illumination contrary to the dark when the incorporation is limited and the system is kept metastable. Under the presence of oxygen, the $MAPbI_3$ degrades resulting in water and iodine products. This reaction occurs as followings[122]:

$$CH_3NH_3PbI_3 + \frac{1}{4}O_2 \rightarrow \frac{1}{2}H_2O + CH_3NH_3 + PbI_2 + \frac{1}{2}I_2 \qquad (1)$$

An analogous degradation study demonstrates that photo-oxidative degradation in $MAPbI_3$ only occurs on the surface because oxygen at room temperature can hardly diffuse spontaneously into the network[124]. The surface degradation can be accelerated furthermore by the exposal to intense I_2 vapor[125]. Nevertheless, exposure to iodine partial pressure is shown to slow down the deterioration of the hybrid perovskite (Fig.III. 2). Theoretical studies reveal that the main photo-oxidation product is the PbO, that has been detected experimentally after the perovskite's degradation[126]. In addition, a reported study suggests that the photo-induced degradation process includes three key steps: generation of superoxide on the surface under light, fast oxidation of the $MAPbI_3$ surface and production of water, and slow hydration of inner $MAPbI_3$[127].

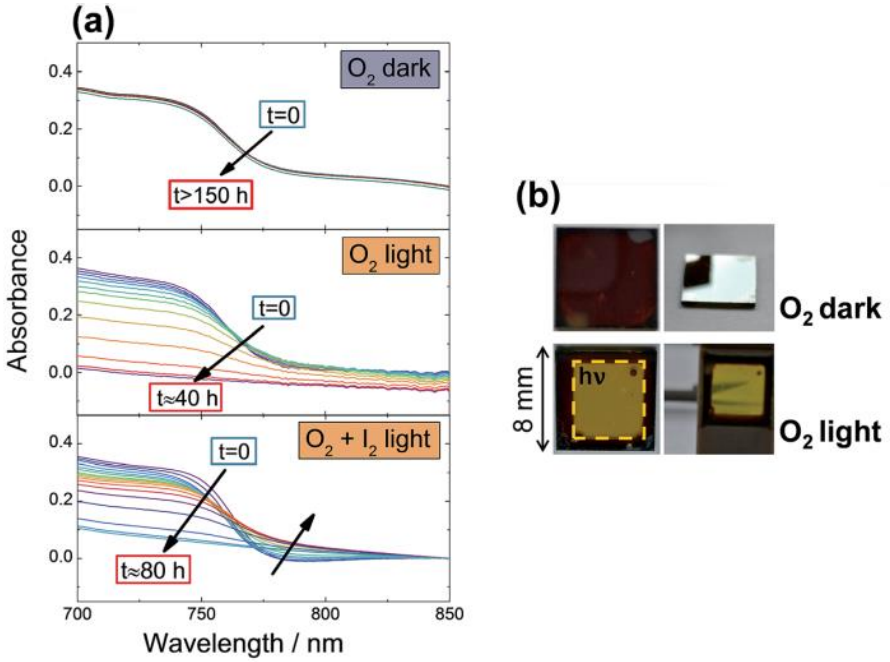

Fig.III. 2. (a) Stability of MAPbI3 films under O_2 exposure, in dark and under illumination (4.6 mW cm^2), monitored by UV-Vis spectroscopy. (b) Photos of the sample after the O_2 exposure under dark and light[122].

3. Photo-thermal degradation of hybrid perovskite

It is unmistakably paradoxical that the most vulnerable aspect of the photoactive organic–inorganic hybrid perovskite is its instability against light. Nevertheless, an experimental study reveal that annealing of hybrid perovskite is a stronger degrading factor than the visible light[128]. This return to the fact that the relaxation of thermal excitations of the system is carried out only by the phonons. Perez et al have used a thermal gravimetric and differential thermal analysis (TG-DTA) combined with a mass spectrometer (MS) to identify the mass loss, and the released gases during hybrid perovskite thermal degradation. They assigned that NH_3 and CH_3I are the gas products identified during the thermal $CH_3NH_3PbI_3$ decomposition that occurs as follows[129]:

$$CH_3NH_3PbI_3 \xrightarrow{\Delta} NH_3 + CH_3I + PbI_2 \quad (2)$$

Other studies have observed that this decomposition can take other ways under different conditions[130-131]. They demonstrate that the process 2 is favored at high temperature. In contrast, at low temperature the thermal decomposition releases CH_3NH_2 and HI gases as products[131]. Furthermore, it has been discovered that illumination leads to the increase of the PbI_2 content in

the thin films which lead to the further device degradation[132]. Additionally, Dawood et al showed that PbI_2 undergoes a photodecomposition which turns it into I_2 gas and Pb atom in the presence of visible light[133]. The two degradation pathways CH_3NH_2 + HI and Pb + I_2 are shown to be reversible paths, in contrast with the photodecomposition NH3 + CH3I which is identified as an irreversible decomposition[134]. Also an exposition of hydrated hybrid perovskite to light leads to their irreversible decomposition[135]. Unlike $MAPbI_3$, $MAPbBr_3$ when subjected to a temperature lower than 300 °C it only releases CH_3NH_2 and HBr (reversible decomposition) which makes of the $MAPbBr_3$ more stable than the $MAPbI_3$ compound. Nevertheless, the organic cations in hybrid perovskite have also a potential effect on the thermal stability of perovskite thin films. In particular, the various compositions of organic cations are proven to affect the material crystallinity and PSCs performances under the effect of thermal stress. It is believed that the combination between formamidinium and cesium in $FACsPbI_3$ thin film produces the most stable perovskite for the PSCs future research[136]. Hybrid perovskite shows also a dependence on excitation wavelengths that affect their photostability[137]. Subsequently, a careful choice of both the halogen anion and the organic cation of the hybrid perovskite is crucial to avoid irreversible reactions.

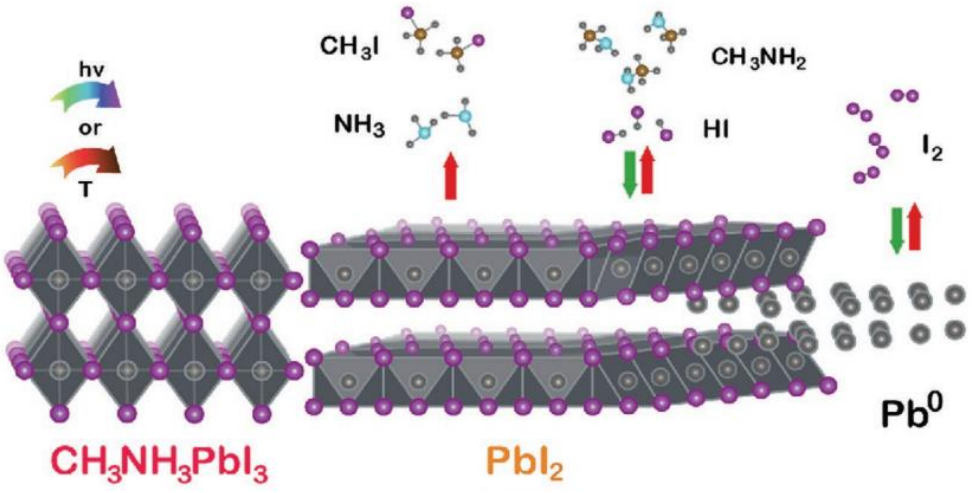

Fig.III. 3. The photodegradation of $MAPbI_3$ under light and mild heat conditions[134].

III. Research progress technology to improve the perovskite solar cells stability

The improvement of hybrid perovskites stability has been a topic under intense investigation. Different strategies have been investigated to enhance the stability of these materials. The various

remedies investigated to mitigate the degradation (Fig.III. 4) were the charge transporting layer modification, composition engineering, additive engineering, encapsulation, preventing electrode inducing degradation. Charge transporting layer (CTL) has important implications on the stability of the device as they represent the interfaces among the contacts and the active layer, it can furthermore prevent external moisture or oxygen to reach the perovskite. Their deposition method can induce the active material degradation[138]. Hence, atomic layer deposition (ALD) technology was adopted for the deposition of very thin and uniform films of solar cells based hybrid perovskite, it is a powerful tool to improve the stability of these devices[139]. Enhancing stability of hybrid perovskite can also be established through the composition engineering. Varying or mixing of different halogen anions (I, Br, Cl), or/and organic cations (MA, FA, Cs, IM) improves the stability of perovskite units by enhancing the films crystallinity and the improvement of moisture tolerance[140-141]. Herein, however, in section 3 we describe the stability and optical absorption enhancing through the doping of the halide ions by bromine in variety of sites. Additives are proven to be a successful approach to enhance the efficiency and stability of this system. They established a strong ion bonds in the crystal which enhance the Pb-I bonding and MA-I bonding, leading to the reduction and passivation of defects[142]. The additives can be both organic or inorganic compounds, and they can be used with precursors or as posttreatment additives[110-143]. Encapsulation is processed to limit the photochemical and thermal damage and results in moisture, oxygen resistant filtration. Three encapsulation strategies have been reported: Glass-to-Glass Encapsulation, polymer Encapsulation, and thin-film encapsulation[144]. Another suggestion evolved by Ramez et al, is to protect hybrid perovskite materials using sputtered barrier coating. They demonstrate that SiO_2 barrier films can improve the tolerance of the devices to extreme humidity conditions and extend their lifetimes without significantly affecting the initial device performance[145]. Finally protecting perovskites with barrier layers was proven to be an effective way to prevent the contact between the mobile halogen vacancies, of the perovskite created by the effect of light, and the metal contacts[146].

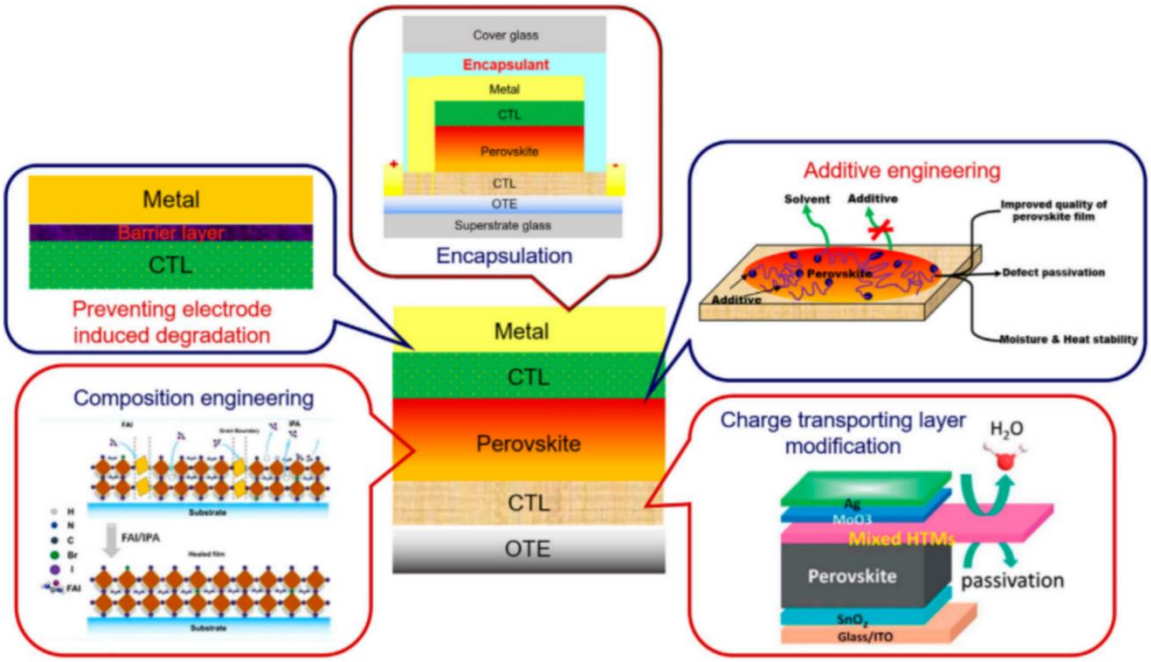

Fig.III. 4. Various remedies to prevent degradation and enhance the efficiency and stability of perovskite solar cells[110]

IV. Toxicity in hybrid perovskite

Hybrid perovskite is an emerging material in the photovoltaic technology in the recent years. It is recognized as a new rising star in the PVCs that has shown large progress in this domain reaching high efficiency of 29% in a few years. The most efficient hybrid perovskite active layer based solar cells was the hybrid lead halide perovskite. The efficiency that it represents makes of him a competitive material with the silicon solar cells. One of the main bottlenecks towards the commercialization of these materials is the highly toxic character of lead (Pb). Lead is potentially harmful to the environment, to plants, to humans, and to animals through consumption of contaminated crops[147]. On the other hand, studies reveal that not only lead causes damages to the ecosystem but also the iodine halogen of the hybrid perovskite. Recent studies have investigated the effect of iodine on the plant, they showed that iodine causes greater harm to plants than the lead[148]. To prevent the spread of lead in the environment, Horvath et al have used transparent phosphate salt in hybrid perovskite based solar cells that forms a highly insoluble compound with lead in a wet environment, thus hindering the Pb^{2+} release[149]. Besides, the key challenge imposed for this material is finding a new alternative that is a low in toxicity or non-toxic metal/halogen

perovskite which will allow to save the unrivaled advantageous optoelectronic and optical properties of lead halide perovskite. Numerous studies in this regard have been reported, in this context double-charged cations, such as Sn^{2+}, Ge^{2+}, and their combination or also other metals such as Bi^{3+}, Sb^{3+}, Cu^{2+}, and Mn^{2+}. The metal substitution of lead by tin and germanium constituted of a compound with a direct bandgap well matches with the photovoltaic application. Furthermore, their band gap energy can be fine-tuned by controlling the composition choice of metal halogen and organic cation[150]. So far, the other substitute metals (Sb^{3+}, Cu^{2+}, Mn^{2+} etc.) have shown a good device stability but low performance regarding the metal group IV (Sn^{2+})[151]. Table.III.1 illustrates the power conversion efficiency (PCE) of lead-free perovskite. Among these candidates, tin (Sn) has emerged as a potential divalent cation that shows similar properties and high performance, however, it suffers from low stability due to the oxidation of Sn^{2+} to Sn^{4+} [152]. The PCE of Pb-Sn-Ge alloy with different halogen will be discussed in details in section 3. Despite all the effort and study attributed to the free lead halide perovskite, they are still not yet approaching the spectacular performance of $APbI_3$ materials. The understanding of the photo-dynamics and underlying working mechanism of Pb free perovskites is vital for helping the future research to reach an ecofriendly material that is both affordable and produces clean energy.

Table.III. 1. Photovoltaic Performance Summary of Lead-Free PSCs[153].

Perovskite	Device structure	Fabrication process	PCE (%)
$MASnI_3$	c-TiO_2/m-TiO_2/absorber/spiro/Au	Spin coating	6.4
$MASnI_3$	c-TiO_2/m-TiO_2/absorber/PTAA/Au	Vapor assisted	1.86
$MASnI_3$	c-TiO_2/m-TiO_2/absorber+ 20%SnF_2/PTAA/Au	Spin coating	1.94
$MASnI_3$	c-TiO_2/m-TiO_2/absorber+ 20%SnF_2/spiro/Au	Solvent engineering	2.33
$MASnI_3$	PEDOT/TPD/absorber/C_{60}/BCP/Ag	Thermal	1.7
$MASnI_3$	PEDOT/absorber/PCBM/Al	Hot casting	3.2
$MASnI_3$	PEDOT/absorber+ 10%SnF_2/C_{60}/BCP/Ag	Solvent engineering	4.29
$MASnI_3$+hydrazine	c-TiO_2/m-TiO_2/absorber+ 20%SnF_2/PTAA/Au	Hot casting	3.89
$MASnIBr_2$	c-TiO_2/m-TiO_2/absorber/spiro/Au	Spin coating	5.73
$MASnI_2Br$	c-TiO_2/m-TiO_2/absorber/spiro/Au	Spin coating	5.48
$MASnBr_3$	c-TiO_2/m-TiO_2/absorber/spiro/Au	Spin coating	4.27
$MASnBr_3$	c-TiO_2/absorber/P3HT/Au	Thermal evaporation	1.12

$MASnI_{3-x}Br_x$	c-TiO_2/m-TiO_2/absorber/PTAA/Au	Vapor assisted	1.1
$MASnBr_3$	c-TiO_2/m-TiO_2/absorber/PTAA/Au	Spin coating	0.14
$MASnCl_3$	c-TiO_2/absorber/CuSCN/Ag	Spin coating	3.41
$MASnIBr_{1.8}Cl_{0.2}$	c-TiO_2/m-TiO_2/m-Al_2O_3/absorber/C	Direct dropping	3.11
$FASnI_3$+pyrazine	c-TiO_2/m-TiO_2/absorber+ 10%SnF_2/spiro/Au	Solvent engineering	4.8
$FASnI_3$	c-TiO_2/m-TiO_2/absorber+ 20%SnF_2/spiro/Au	Spin coating	2.10
$FASnI_3$	c-TiO_2/m-TiO_2/absorber+ 20%SnF_2/spiro/Au	Solvent engineering	5.27
$FASnI_3$	c-TiO_2/m-TiO_2/absorber+ 15%SnF_2/TPE/Au	Spin coating	7.23
$FASnI_3$+TMA	SnO_2/C_{60}/absorber/spiro/Ag	Sequential deposition	4.34
$FASnI_3$+TMA	PEDOT/absorber+ 10%SnF_2/C_{60}/bis-C_{60}/Ag	Sequential deposition	7.09
$FASnI_3$	PEDOT/absorber+ 10%SnF_2/C_{60}/BCP/Ag	Solvent engineering	6.22
$FASnI_3$	PEDOT/absorber/C_{60}/BCP/Ag	Sequential deposition	3.98
$FASnI_3$	PEDOT-PEG/absorber+ 12%SnF_2/PCBM/BCP/Ag	Solvent engineering	5.12
$FASnI_3$+ 2.5%N_2H_5Cl	PEDOT/absorber+ 10%SnF_2/PCBM/BCP/Ag	Solvent engineering	5.40
$FASnI_3$+PEABr	PEDOT/absorber+ 10%SnF_2/C_{60}/BCP/Cu	Solvent engineering	7.05
$FASnI_2Br$	PEDOT/absorber/C_{60}/Ca/Al	Solvent engineering	1.72
$CsSnI_3$	ITO/absorber/Au/Ti	Thermal evaporation	0.88
$CsSnI_3$	NiO/absorber/PCBM/Al	Spin coating	3.31
$CsSnI_3$	c-TiO_2/absorber/spiro/Au	Quantum rods	12.96
$CsSnI_3$	c-TiO_2/absorber/spiro/Au	Spin coating	0.77
$CsSnI_3$	c-TiO_2/m-TiO_2/absorber+ 20%SnF_2/spiro/Au	Spin coating	1.66
$CsSnI_2Br$	c-TiO_2/m-TiO_2/absorber+ 20%SnF_2/spiro/Au	Spin coating	1.67
$CsSnBr_3$	c-TiO_2/m-TiO_2/absorber+ 20%SnF_2/spiro/Au	Spin coating	2.17
$CsSnIBr_2$	c-TiO_2/m-TiO_2/absorber+ 20%SnF_2/spiro/Au	Spin coating	1.56
$MA_3Bi_2I_9$	c-TiO_2/m-TiO_2/absorber/spiro/MoO_3/Au	Spin coating	0.42
$MA_3Bi_2I_9$	PEDOT/absorber/C_{60}/BCP/Ag	Sequential deposition	0.39
$MA_3Bi_2I_9$	c-TiO_2/m-TiO_2/absorber/spiro/Au	Solvent engineering	0.36

$Cs_3Bi_2I_9$	c-TiO_2/m-TiO_2/absorber/P3Ht/Ag	Spin coating	0.02
$Cs_3Bi_2I_9$	c-TiO_2/m-TiO_2/absorber/spiro/Ag	Spin coating	1.09
$Cs_2AgBiBr_6$	c-TiO_2/m-TiO_2/absorber/spiro/Au	Spin coating	2.43
$MA_3Sb_2I_9$	PEDOT/absorber/PCBM/ZnO/Al	Solvent engineering	0.49
$MA_3Sb_2I_9$	PEDOT/absorber+HI/PCBM/C_{60}/BCP/Al	Spin coating	2.04

First Section-conclusion

In this section the working of photovoltaic effect has been introduced. We showed that crystalline silicon was the first material used as an absorbing layer in solar cell, followed by other materials that have been the subject of new photovoltaic generations. The fourth generation based on hybrid perovskite that represent the main interest subject of this thesis have been introduced after. The impressive properties of hybrid perovskite were first initiated. We showed that different solar cell based hybrid perovskite structure exists namely n-i-p or p-i-n solar cell devices. The hybrid perovskite synthesis is less expensive and can be established by the one-step or two-step deposition process. Their photophysical properties diverse depending on temperature and also on the interaction nature between the organic and the inorganic part. The hybrid perovskite presents some drawbacks such as their toxicity and low stability under different environment condition. This instability can be improved by modifying the charge transporting layer or by encapsulation. Furthermore, to eliminate toxicity in hybrid perovskite double-charged cations such as Sn^{2+}, and Ge^{2+} was used, however, they are still not yet approaching the spectacular performance of lead halide perovskite materials.

2nd Section

Design of research

✉ Faculté des Sciences, avenue Ibn Battouta, BP. 1014 RP, Rabat –Maroc
☎ 00212(05) 537 77 18 34/35/38, 🖷 00212(05) 537 77 42 61, http://www.fsr.ac.ma

Second Section-Introduction

The evolution of sciences is based systematically on two distinct levels which are theoretical and experimental studies. Theory was developed based on the investigation of natural phenomena with the aim to explain a much wider variety of effects or phenomena occurring in experiments, in technology, and in industry[154]. In this context, quantum theory manifestation was the key to the transition from macroscopic object to microscopic particle, where it opens the route toward the atomic scale description of objects by using some semi-empirical methods or by ab initio calculations[155]. Both the semi-empirical and ab initio methods are based on the solution of the Schrodinger equation. However, these practical method shows some limits with the evolution of system size[156]. In this, density functional theory has been proposed as it can provide simulation for large systems at modest computational costs[157]. Density functional theory (DFT) express the energy in terms of density, it shows success in predicting the properties of atoms, molecules, and solids. The application of this theory has opened the door to the modeling of diverse materials in different branches such as physics, material science, and chemistry. DFT will be the main method used in this thesis. This chapter presents a brief summary of DFT and Quantum Espresso code that have been involved in the investigation of the hybrid perovskite properties that are the main research subject focus of this thesis. Quantum espresso code is an implementation of density functional theory used in electronic structure, simulation, and optimization research that involve a huge number of atoms

Chapter I

Density functional theory: concepts and approaches

I. Introduction

A description of a particular system in quantum mechanics can be established throughout the Schrodinger equation. Solving this equation proves to be difficult for large systems with N variables. In this chapter we present a definition of the Schrodinger equation as well as the approximation used for simplifying this equation concluding with a simplified Kohn-Sham equation that solves the Schrödinger equation for each one-electron Hamiltonian separately.

II. Schrödinger equation

the non-relativistic time independent Schrodinger equation is a differential equation that describes the behavior of a quantum system with N electrons. It allows the calculation of the energy levels and other properties of atoms and molecules. The major goal of electronic structure calculations is to solve the time independent Schrodinger equation that is good in predicting the wave functions. The solution of these equations is called stationary states or ''orbitals'' since they describe a particular state of the studied system. Time independent Schrodinger equation is given as[158]:

$$E\Psi = \hat{H}\Psi \qquad (1)$$

where E is the system energy, $\Psi(\ r_1, \dots, r_i, R_1, \dots, R_N)$ is a wave function that depends on the position of i electrons {r} and N nuclei {R}, $\hat{H}$ is the Hamiltonian operator, sum of the kinetic (T) and potential energy (V) operators respectively expressed as :

$$\hat{H} = \mathrm{T_N} + \mathrm{V_{N-N}} + \mathrm{V_{e-N}} + \mathrm{V_{e-e}} + \mathrm{T_e} \qquad (2)$$

Where:

- $\mathrm{T_N} = -\frac{\hbar^2}{2\mathrm{m_N}}\sum_{\mathrm{N}} \Delta_{\mathrm{N}}$ The kinetic energy operators of the nuclei.
- $\mathrm{V_{N-N}} = \frac{1}{2}\sum_{\mathrm{N},\dot{\mathrm{N}}\neq\mathrm{N}} \frac{\mathrm{e}^2\, \mathrm{Z_N Z_{\dot{N}}}}{4\pi\varepsilon_0|\vec{\mathrm{R}}_{\mathrm{N}}-\vec{\mathrm{R}}_{\dot{\mathrm{N}}}|}$ The Coulomb repulsion potential between the nuclei.
- $\mathrm{V_{e-N}} = -\sum_{\mathrm{i,N}} \frac{\mathrm{Z_N}\, \mathrm{e}^2}{4\pi\varepsilon_0|\vec{\mathrm{R}}_{\mathrm{N}}-\vec{\mathrm{r}}_{\mathrm{i}}|}$ The Coulomb attraction potential electron-nuclei.

- $V_{e-e} = \frac{1}{2}\sum_{i,j\neq i}\frac{e^2}{4\pi\varepsilon_0|\vec{r}_i-\vec{r}_j|}$ The Coulomb repulsion potential between the electrons.
- $T_e = -\frac{\hbar^2}{2m_e}\sum_i \Delta_i$ The kinetic energy operators of electrons.

For a hydrogen atom with a single particle, the Schrodinger equation can be solved exactly to determine the allowed energy state of the system. For multi electronic systems, its complicated expression makes calculations very demanding in terms of time and computational cost. As such, Bron-Oppenheimer approximations and density functional theory (DFT) methods are provided to simplify the Schrödinger equation.

III. Born-Oppenheimer approximation

The Born-Oppenheimer approximation separates the motion of nuclei from that of electrons. Within this framework, it is considered that nuclei are heavier, and show very slow motion compared to electrons. Thus, the dynamics of the two components can be decoupled and studied separately[159]. For electrons, the kinetic energy of nuclei is considered negligible and the repulsion term between nuclei is considered constant. The total wave function of the system can therefore be written as the product of a wave function describing the nuclei $\Psi_n(R)$ that is only related to the nuclei position R, and another wave function describing the electrons $\Psi_e(r, R)$ related to both R, and r position of nuclei and electron respectively:

$$\Psi(r, R) = \Psi_n(R)\Psi_e(r, R) \quad (3)$$

The electrons, in this approximation instantaneously follow the nuclear motion adiabatically, and the new Hamiltonian resulting from the Born-Oppenheimer approximation is written in the following form:

$$\widehat{H} = T_e + V_{N-N} + V_{e-N} + V_{e-e} \quad (4)$$

Although the double approximation of Born-Oppenheimer and adiabatic allows simplifying the equation in a considerable way, the electronic equation remains a many-body problem. Due to this difficulty, additional approximations are required to effectively solve the Schrödinger equation for real materials.

IV. Density functional theory

The density functional theory was introduced in 1964 by Pierre Hohenberg and Walter Kohn[160]. Hohenberg Kohn demonstrates by this theory that the complicated many body wave-function can be replaced by a much simpler density. Density functional theory provides a simple function of 3 spatial coordinates (x, y, and z) instead of the wave function that depends on N variables, where N is the total number of electrons in the system. In this context, Hohenberg Kohn proved two fundamental mathematical theorems. The first one states that: The ground-state energy from Schrodinger's equation is a unique functional of the electron density. This theorem introduces the energy functional E $[\rho(\vec{r})]$ which maps the electron density ρ(r) to the total energy of the system, usually expressed as:

$$E[\rho(\vec{r})] = T[\rho(\vec{r})] + E_{e\text{-}e}[\rho(\vec{r})] + E_{e\text{-}N}[\rho(\vec{r})] = F_{HK}[\rho(\vec{r})] + E_{e\text{-}N}[\rho(\vec{r})] \quad (5)$$

Where the universal Hohenberg-Kohn functional $F_{HK}[\rho(\vec{r})]$ contains the information about the kinetic energies and electron-electron interactions. The Coulomb interaction between electron and nuclei is treated as an external potential $\hat{V}_{ext}$. The total energy functional can be written

$$E[\rho(\vec{r})] = F_{HK}[\rho(\vec{r})] + \int \hat{V}_{ext}(\vec{r})\rho(\vec{r})d\vec{r} \quad (6)$$

where,

$$E_{e\text{-}N}[\rho(\vec{r})] = \int \hat{V}_{ext}(\vec{r})\rho(\vec{r})d\vec{r}$$

The second Hohenberg –Kohn theorem defines an important property of the function. It states that: The electron density that minimizes the energy of the overall functional is the true electron density corresponding to the full solution of the Schrodinger equation. The Hohenberg-Kohn theorems are extremely powerful as they accord a ground state density that holds in all possible information about the system. Therefore, they do not provide a way to calculate the ground state density of the system due to the lack of knowledge about the functional $F_{HK}[\rho(\vec{r})]$ form. Kohn-Sham put after a forward method to remedy this problem.

V. The Kohn-Sham method

In 1965, Kohn and Sham transform the ground state charge density of the interacting particles into an equivalent system of non-interacting electrons[161]. The fictitious auxiliary non-interacting system

proposed by Kohn and Sham that represents the same density of the interacting electrons system made the density functional theory feasible. By this method, the problem is turned from determining the $F_{HK}[\rho(\vec{r})]$ functional to finding the fictitious system of non-interacting electrons which has the same ground state density as the original system. The Schrödinger equation is therefore reformulated in terms of the so-called Kohn-Sham equation, which is in fact a Schrödinger equation with an effective potential in which Quasi-particles move. The electronic Hamiltonian is expressed as:

$$H\,[\rho(\vec{r})] = -\frac{\hbar^2}{2m_e}\sum_i \Delta_i + \sum_i \widehat{V}_{ext}(\vec{r}) + \frac{1}{2}\sum_{I,j\neq i}\frac{e^2}{4\pi\varepsilon_0\left|\vec{r}_i - \vec{r}_j\right|} \tag{7}$$

By introducing the non-interacting electrons method, the interaction electrons term is replaced by one-electron operator (Potential) V_{av} that describes the "average" effect of the interaction. In this case, the Hamiltonian operator is simply expressed as a sum of one-electron operators:

$$\widehat{H}_{eff}\,[\rho(\vec{r})] = -\frac{\hbar^2}{2m_e}\sum_i \Delta_i + \sum_i \widehat{V}_{ext}(\vec{r}) + \sum_i V_{av}(\vec{r}) \tag{8}$$

$$= -\frac{\hbar^2}{2m_e}\sum_i \Delta_i + \sum_i\{\widehat{V}_{ext}(\vec{r}) + V_{av}(\vec{r})\}$$

$$= -\frac{\hbar^2}{2m_e}\sum_i \Delta_i + \sum_i V_{eff}(\vec{r})$$

$$= \sum_i\{-\frac{\hbar^2}{2m_e}\Delta_i + V_{eff}(\vec{r})\}$$

Thus, The Hamiltonian can be expressed as a sum of one-electron Hamiltonians and the Schrödinger equation can be solved for each one-electron Hamiltonian separately as:

$$\left[-\frac{\hbar^2}{2m_e}\Delta_i + V_{eff}(\vec{r})\right]\psi_i(r) = \varepsilon_i\psi_i(r) \tag{9}$$

with the effective potential

$$V_{eff}(r) = V_{ext}(r) + V_H(r) + V_{xc}(r) \tag{10}$$

where $V_H(r)$ is the Hartree potential, and $V_{xc}(r)$ the exchange-correlation potential functional derivative of $E_{XS}[\rho(\vec{r})]$ ($E_{XS}[\rho(\vec{r})]$ represents the differences between the exact and approximate solutions for the kinetic energy and electron-electron interaction terms)

$$V_{xc}(r) = \frac{\partial E_{xs}[\rho(\vec{r})]}{\partial \rho(\vec{r})} \tag{11}$$

where

$$\rho(\vec{r}) = \sum_{i=1}^{M} |\psi_i(\vec{r})|^2$$

The Kohn-Sham method is a powerful approach to obtain an accurate ground-state density. Therefore defining the exact form of the exchange-correlation potential $V_{xc}(r)$ reminds the biggest challenge of Kohn-Sham DFT. Thus, the calculation of the energy and the exchange-correlation potential is relatively based on a certain number of approximations that can give quite accurate results such as the LDA and the GGA approximations.

VI. Exchange Correlation Approximation

As a first step, for simplification the energy exchange correlation can be written as the sum of two parts: the pure exchange term and the pure correlation term:

$$E_{XC}(n) = E_X(r) + E_C(n) \tag{12}$$

The best understanding of the exact exchange correlation functional can be obtained by the best approximation. Here the two popular local density approximations (LDA), and the generalized gradient approximation (GGA) will be discussed.

1. Local density approximation

The fundamental assumption contained in the Local density approximation (LDA) formalism consists in considering the real system density as the density of the homogeneous electron gas[161]. The LDA functional assumes that the exchange-correlation part of the total ground state energy of the electronic system can be written as:

$$E_{xc}^{LDA}[\rho(\vec{r})] \approx \int \varepsilon_{xc}^{LDA}[\rho(\vec{r})]\, \rho(\vec{r}) d\vec{r} \tag{13}$$

where $\varepsilon_{xc}^{LDA}[\rho(\vec{r})]$represents the exchange-correlation energy per electron in a system of mutually interacting electrons of uniform density $\rho(\vec{r})$. The exchange energy term can be calculated exactly for the LDA approximation by the formula[162]:

$$\varepsilon_{x}^{LDA}[\rho(\vec{r})] = \frac{3}{4}\left(\frac{3}{\pi}\right)^{\frac{1}{3}} \rho(\vec{r})^{\frac{1}{3}} \qquad (14)$$

while the correlation energy is calculated using Monte Carlo simulations of uniform electron gases[163]. The treatment of the exchange-correlation energy from the LDA works well in the case of metals for which the density is strongly uniform or varies slowly. However, the LDA approximation fails in systems characterized by strongly varying electron densities and for the transition metals.

2. Generalized Gradient Approximation

The Generalized Gradient Approximation (GGA) improves the functional's performance by introducing the gradient of the density for the exchange correlation energy calculation[164]. This correction to the LDA approximation allows a good description of the system's energy as the GGA approximation takes into account the non-uniform character of the electron gas. The definition of the GGA functional implies the form:

$$E_{xc}^{GGA}[\rho(\vec{r})] \approx \int \varepsilon_{xc}[\rho(\vec{r}), |\nabla\rho(\vec{r})|]\,\rho(\vec{r})d\vec{r} \qquad (15)$$

where $\int \varepsilon_{xc}[\rho(\vec{r}), |\nabla\rho(\vec{r})|]$ is the exchange-correlation energy per electron in a mutually interacting electron system of non-uniform density. A large variety of GGA functional exist such as PBE[165] which provides several improvements for periodic systems, and is generally used for solids, and PBEsol[166] that is designed to improve equilibrium properties and surface energies. On the other hand, GGA functional are not considered as non-local methods since they only depend on the density at a given point r. Thus, due to the local character, the GGA fails to correctly handle systems characterized by interactions linked to long-range electrons correlations and sometimes overestimates the band gap energy. Further improvements to this correlation function can be made using the Van der Waals correction approximation.

VII. Van der Waals correction

The van der Waals (vdW) interactions or the so called long-range dispersion interactions between atoms and molecules play a crucial role in many chemical systems. Thus, taking into account the vdW interactions within the framework of density functional theory is one of the promising approaches for the theoretical description of organic or layered materials as well as that of physical, chemical, and biological processes[167]. VdW is a non-local approximation that introduces the intermolecular force, it is the sum of the forces of:

$$\mathrm{E_{vdw}} = \mathrm{E_{keesom}} + \mathrm{E_{Debye}} + \mathrm{E_{London}} \quad (16)$$

where the $\mathrm{E_{keesom}}$ results from the interaction between two dipoles (It tends to align the molecular dipoles): orientation effect, $\mathrm{E_{Debye}}$ results from the interaction between a permanent dipole and an induced dipole: induction effect, $\mathrm{E_{London}}$ results from the interaction between 2 induced dipoles: dispersion effect. In the vdW-DF method, the exchange correlation energy is given as[168]:

$$\mathrm{E_{XC}} = E_X^{GGA} + E_C^{LDA} + E_C^{nl} \quad (17)$$

where the pure exchange energy is given by the generalized gradient approximation (GGA): E_X^{GGA}, and the correlation energy term is the sum of the local density approximation (LDA) correlation energy E_C^{LDA}, and the nonlocal electron correlation energy E_C^{nl}. The vdW approximation was employed throughout this thesis to introduce the interaction effect between the organic and inorganic parts of the hybrid perovskite

Chapter II

Implementation of DFT and computation methodology

I. Introduction

The aim of this chapter is to present how Bloch's theorem in combination with pseudopotential can be used for simplifying and describing the system's properties by using a small simple unit cell instead of the full cell. The description of the Quantum espresso code that has been used in the research outcomes investigation (section 3) as well as the definitions of the band structure, density of state, dielectric response and phonon dispersion are provided in this chapter.

II. Plane Wave Basis Set and periodic boundary conditions

As seen previously, the ground state energy can be determined by solving the single-particle Kohn-Sham equations. Moving to the practical application of DFT, the electronic wave function in the Kohn-Sham method or density functional theory is represented as a basis set[169]. This representation is required and needed to be considered to describe infinite large-scale space. The calculation of a large number of electrons with wave function is very difficult, in this regard Bloch's theorem is used[170]. This theorem, based on the periodicity of the crystal structure, allows the use of a small simple unit cell instead of the full cell to calculate the properties needed. The unit cell is the smallest repeating unit in the crystal. Thus, we can move from a large number of one electron wave functions to a minimum of electrons contained in the unit cell. For a given lattice, we can describe two types of unit cells that are primitive and conventional cells. the primitive cell is a unit cell containing only one lattice point, and the conventional cell is the smallest unit cell that contains the same group symmetries as the overall lattice. When Bloch's theorem is applied the wave function of the Schrodinger equation can be written as[171]:

$$\psi(r) = e^{ikr}u(r) \qquad (1)$$

with

$$u(r) = u(r + l)$$

where r represents the position in real space, k is the crystal wave vector in reciprocal space, $\psi(r)$ is the wavefunction of the electron, u(r) is a periodic function; l represents the unit cell length, and

e^{ikr} is the plane wave. Thus, Bloch's theorem dictates the usage of plane waves in calculations involving periodic boundary conditions that will allow moving from the coordinate system in real space to the k-space through fast Fourier transforms, which enables much faster operations. Furthermore, plane waves in combination with pseudopotential are used in order to describe core electron and nuclei interactions. Since the pseudopotential is taken as an approximation accounting for the interaction effect by the core electrons and the valence electrons

III. Pseudopotentials approximation

Solids are a collection of valence electrons and ion cores (nuclei and quite strongly bound core electrons). In the core space, due to the strong Coulomb potential of the electron-ion interaction, the valence electrons wave functions always oscillate fast frequently. To describe this interaction between ions and electrons, a huge number of Basis functions are needed to be accurately represented. Since the potential has the same periodicity as the underlying lattice, it can be represented as a linear combination of plane waves:

$$u_n(\mathrm{r}) = \sum_G C_{n,G} \mathrm{e}^{\mathrm{iG.r}} \tag{2}$$

where the $C_{n,G}$ are one electron wave function in the reciprocal space, and wave vectors G are reciprocal lattice vectors of the crystal. Thus the one electron wave function can be written as[172]:

$$\psi_{\mathrm{n,k}}(\mathrm{r}) = \sum_G C_{n,k+G} \mathrm{e}^{\mathrm{i(k+G).r}} \tag{3}$$

There are of course an infinite number of reciprocal lattice vectors defined by an infinite lattice. In practice, an infinite number of basis functions is required. However, this is not computationally feasible and a plane wave energy cutoff must be introduced. The plane wave energy cutoff is defined by:

$$\mathrm{E_{k+G}} = \frac{\hbar^2}{2\mathrm{m_e}} |k + G|^2 \tag{4}$$

The effect of the cut-off is to produce a less accurate wave-function and hence higher energy of the system. Systems should be tested for convergence to ensure that the effects of the truncation are not affecting the conclusions drawn from the calculation.

The concept of a pseudopotential is to describe in combination with plane waves the strong interactions between core electron and nuclei[173]. In terms of reducing the plane wave number needed to represent the wave-functions and also to reduce the computational cost, the core electrons were removed from the calculation to reduce the number of Kohn-Sham orbitals, thus is made true the pseudopotentials introduction. It is known that the most physical properties of solid are determined by the valence electron as they are the electron involved in bonding. Instead, the core electrons are highly localized around the nucleus and they don't contribute to the formation of chemical bonds. This allows the pseudopotential approach to consider the ion cores as frozen, and take the core electrons in any system to have the same distribution as they would in an isolated atom. Thus, the pseudopotential approximation replaces the strong ionic potential with a weaker pseudopotential. The advantage of this approach is to reduce significantly the electrons number in the system. The pseudopotentials are carefully well represented using only low plane waves and are equal to the corresponding orbital from the all-electron calculation. This combination of pseudo potentials and plane waves is represented by a small number of Fourier components. Plane wave basis sets in combination with pseudopotentials are utilized by the Quantum Espresso code used in this thesis.

IV. Quantum Espresso code

Quantum Espresso code is one of the most widely used open source software for research in electronic structure, simulation, and optimization[174]. It is a density functional implementation using plane wave basis set and pseudopotentials. The Quantum Espresso distribution contains different packages for the calculation of a variety of properties such as electronic-structure properties, energy barriers and reaction pathways, and vibrational properties. Quantum Espresso code executes the self-consistent calculation to find the ground state charge density. A schematic diagram of the self-consistent loop for DFT calculation is given in Fig.II. 1. Self-consistent calculation begins at a first step by constructing a potential from the given atomic positions, then an initial guess for the electron density $\rho(r)$ is assumed. The latter is used for the calculation of the effective potentials $V_{eff}(r)$. One can solve the Kohn-Sham equations, which can be used to calculate new electron densities. The procedure repeats until the charge density and the Kohn-Sham Hamiltonian are consistent with each other (results do not change from one cycle to another). When the criterion is satisfied, energy, forces, and others output quantities are computed.

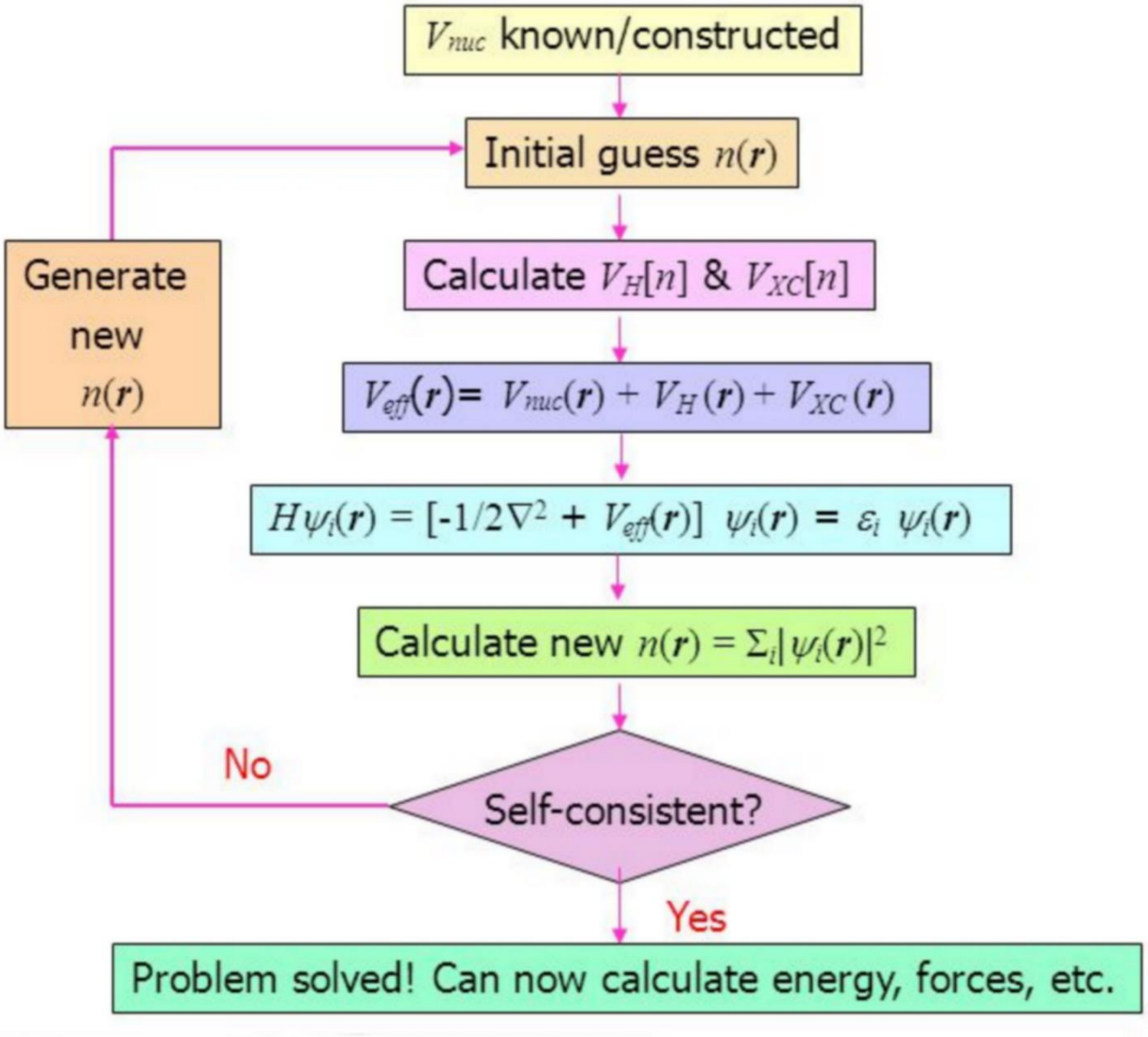

Fig.II. 1. Schematic diagram of self-consistent loop for DFT calculation.

V. Band structure

As seen before the description of the electron properties is reached by solving the Schrödinger equation:

$$\mathrm{H}\psi = \mathrm{E}\psi$$

Under a periodic potential and taking into account the periodicity of the lattice this equation can be rewritten as[175]:

$$\mathrm{H}\psi = \mathrm{H}\psi_{k+G} = E(k)\psi_k \quad (5)$$

$$= E(k)\psi_{k+G}$$

where the wave vector G is described as $G = hg_1 + kg_2 + lg_3$, the g_i are the base vectors and h, k and l are the so called Miller-indices. E(k) represents the dispersion of a free electron that describes how the energy of an electron varies as a function of the crystal wave vector. Considering the translational invariance in the reciprocal space, the electronic dispersion relation can be defined as:

$$\mathrm{E_k} = \frac{\hbar^2|\mathrm{k}|^2}{2\mathrm{m_e}} = \frac{\hbar^2}{2\mathrm{m_e}}|\mathrm{k}+\mathrm{G}|^2 \quad (6)$$

Thus, due to the periodicity of E(k), describing E(k) in the first Brillouin zone is sufficient to describe it in the entire periodic lattice. The energy surface E(k) is shown in Fig.II. 2 which refers to the so called band structure. The band structure gives crucial information about the electrical properties of a system, as well as indicates the magnitude and nature (direct vs indirect) of the fundamental band gap. The E(k) dispersion curvature defines also the effective mass of both holes and electrons, as it is expressed by their second derivative with the formula:

$$m^* = \hbar^2 \left[\frac{\partial^2 E}{\partial k^2}\right]^{-1} \quad (7)$$

Effective masses are inversely proportional to the band structure curvature which demonstrate that a large curvature as depicted in Fig.II. 2.c correspond to a small effective mass instead small curvature define a large effective mass. Extrema shape curvature of the band structure influence also the electrical conductivity of materials as it is related to the effective mass by the equation:

$$\sigma = ne\mu \quad (8)$$

where the carrier mobility μ is expressed by $\mu = \frac{e\tau}{m^*}$, n represents the carrier concentration, τ collision time, and m^* the effective mass.

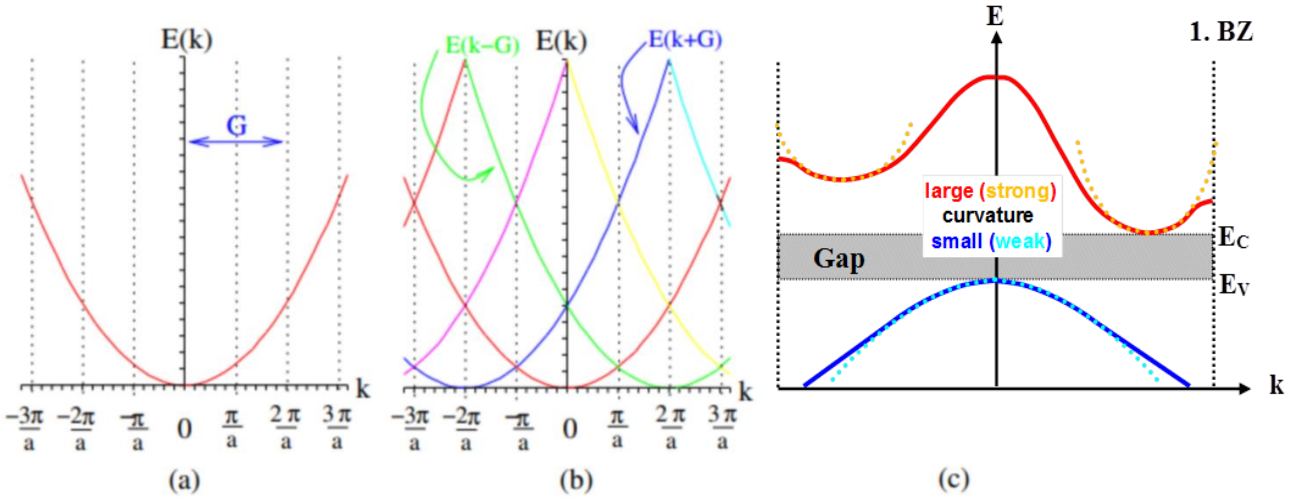

Fig.II. 2. Simple band structure diagrams for a one dimensional periodic solid (a), repeated zone (b), and reduced zone (c) curvature of the dispersion curve at the extrema.

VI. Density of states

The density of states (DOS) measures the number of different electronic states at a particular energy level that electrons are allowed to occupy (The number of electron states per unit volume per unit energy)[176]. The state number achieved by a quantum system is the possible number of available states. Taking into account the spin degeneracy, the total number of states can be written as:

$$N = \frac{V_{System}}{V_{single-state}} \times 2 \qquad (9)$$

where V_{System} is system volume, $V_{single-state}$ is the volume of a single state of that system, a factor of 2 is added to account for the two possible electron spins. At a specific energy level, a high DOS demonstrates that there are many electronic states available for occupation, instead in an energy level when no states are allowed to be occupied the DOS is shown to be zero. The DOS is performed by the energy surface E(k) integration over the first Brillouin zone (BZ) as:

$$\mathrm{Dos(E)} = \frac{1}{\mathrm{V}}\sum_{i=1}^{N} \delta\big(\mathrm{E} - \mathrm{E}(K_i)\big) \qquad (10)$$

E(k) describes the energy levels accessible to electrons can occupy at each point k of the electronic Brillouin zone (BZ).

Thus the density of states per unit volume and per unit energy is expressed as:

$$Dos(E) = \frac{1}{2\pi^2}\left(\frac{2m^*}{h^2}\right)^{\frac{3}{2}}\sqrt{E} \quad (11)$$

The contribution of a particular atom and orbital to the total DOS can be seen by the plot of the partial density of states (PDOS). In the experimental study, the DOS of the conduction band can be investigated by high energy resolution EELS, while The DOS of the valence band is obtained by X-ray emission spectroscopy (XES).

VII. Dielectric response

The dielectric properties of materials are of practical importance since the optical properties are light-wavelength dependent on the dielectric function. The complex electric function demonstrates how a material's optical properties are dependent on the incident wavelength of light. The response of a material to an external electric field is described by frequency dependent dielectric function $\varepsilon(\omega)$:

$$\varepsilon = \epsilon_1 + i\epsilon_2 \quad (12)$$

where ϵ_1 and ϵ_2 are the real and imaginary dielectric functions, respectively. A different observable can be deduced from the dielectric function such as the absorption coefficient, reflectivity, and transmission. The absorption coefficient α and the reflectivity R are calculated using the real and imaginary part of the dielectric function by the standard expressions[177]:

$$\alpha = \frac{4\pi k}{1240}E \quad (13)$$

$$R = \frac{(n-1)^2 + k^2}{(n+1)^2 + k^2} \quad (14)$$

where the extinction coefficient k and the refraction index n are calculated by the formula:

$$k = \left[\frac{\sqrt{{\epsilon_1}^2 + {\epsilon_2}^2} - \epsilon_1}{2}\right]^{\frac{1}{2}} \quad (15)$$

$$n = \left[\frac{\sqrt{{\epsilon_1}^2 + {\epsilon_2}^2} + \epsilon_1}{2}\right]^{\frac{1}{2}} \quad (16)$$

Time dependent density functional theory (TD-DFT) is one of among approaches used to the description of the excited states. TD-DFT establishes a direct relationship between the time-dependent electron density and the time-dependent potential. Similarly, the time-dependent Kohn-Sham equations will need to be derived, thereafter, the time-dependent Schrödinger equation can be solved. In this thesis, optical properties have been described using Yambo code[178] which uses Bethe–Salpeter (BS) equation for the electron–hole Green's function, within the many body perturbation theory (MBPT) framework. This approach provides reasonable agreement with the experiment as it takes into account electron–hole interactions in the quantitative description of the optical response of an interacting electron system. The complex dielectric function is closely connected with the band structure since it results from summing over conduction bands[179]. This function consists of direct and indirect interband transition contribution that are made between electrons and photons only at the same k point or by considering vibrations of the crystal respectively.

VIII. Phonon dispersion

Adiabatic approximation guarantees that ground state configurations are attended by electrons when ionic positions are fixed. Once electrons are not in an equilibrium position, the forces on all atoms in the crystal arise. The force on each atom is supplied within the DFT calculation, then the above is used to provide a series of phonon frequencies. Due to the displacement of atoms around their equilibrium positions, the position of an atom can be decomposed into two terms:

$$R_i = R_i^0 + U_i \tag{17}$$

where R_i^0 and U_i are the ideal lattice position, and the displacement respectively. Crystal potential energy that keeps the atoms together expressed as a function of the U_i displacement are given by:

$$\phi = \phi_0 + \sum_{i\alpha} \phi_\alpha(i) u_{i\alpha} + \frac{1}{2} \sum_{i\alpha j\beta} \phi_{\alpha\beta}(i,j) u_{i\alpha} u_{j\beta} + \cdots \tag{18}$$

Indices α and β denote Cartesian coordinates, while i and j are atom indices. ϕ_0 represents the potential energy of the atom in the frozen position, ϕ_α, and $\phi_{\alpha\beta}$ are the first and second order force constants.

$$F_{i\alpha} = -\frac{\partial \phi}{\partial u_{i\alpha}} = -\phi_\alpha(i) \tag{19}$$

and

$$\phi_{\alpha\beta}(i,j) = \frac{\partial^2 \phi}{\partial u_{i\alpha} \partial u_{j\beta}} \tag{20}$$

$$= -\frac{\partial F_{j\beta}}{\partial u_{i\alpha}},$$

which are the second-order coefficients that correspond to the harmonic approximation.

Thus, the force felt by an atom at site j is given by:

$$F_{j\beta} = -\sum_{i\alpha} \phi_{\alpha\beta}(i,j)\, u_{i\alpha} \tag{21}$$

Atomic vibration is solved with the second-order terms as the harmonic approximation obtained by solving the eigenvalue problem of dynamical matrix D(q). For periodic boundary conditions, the Fourier transform of the force constant matrix is related to the dynamical matrix:

$$D_{k\alpha k'\beta}(q) = \frac{1}{\sqrt{M_k M_{k'}}} \sum_{l} \phi_{\alpha\beta}(lk, 0k') e^{-iq\left(R^0_{lk} - R^0_{0k'}\right)} \tag{22}$$

where l denote the unit cell, k, k' are the atom inside a unit cell, and $M_k, M_{k'}$ are masses of atoms. By the diagonalization of the dynamical matrix, we can determine the equation for the normal modes or phonons as:

$$D(q) e_{qj} = \omega_{qj}^2 e_{qj} \tag{23}$$

where ω_{qj} and e_{qj} give the phonon frequency and polarization vector of the phonon mode determined by the wave vector q and branch index j. Phonon is very useful for accounting variety of properties and behavior of crystalline materials, such as thermal properties, mechanical properties, phase transition, and superconductivity. The lattice vibration frequencies and the phonon dispersion spectrum are also beneficial in the context of predicting new structures (thermodynamic stability study). In this thesis, first principles phonon calculations were performed using Phonopy code[180].

Second Section- conclusion

In this section, we went thoroughly with the description of the computational methods we used in our investigations namely, the density functional theory which is mainly based on the Schrodinger equation. A definition of the different models used for solving the Schrodinger equation has been introduced ending with the Kohn-sham equation a non-interacting Schrödinger equation for one electron. Density functional theory (DFT) is based on this equation and the two theorems given by Hohenberg and Kohn. Thus, DFT is implemented in different codes utilized for theoretical properties meant for the investigation of materials and charge densities. The description of the quantum espresso (QE) code used in this thesis was carefully explained. QE uses the pseudopotentials and plane wave basis sets approaches to provide the electronic structure calculation for materials. Furthermore, approximations such as GGA and LDA are used by QE to express the exchange-correlation potential between atoms. Optical transitions were investigated through the application of an external electric field by using Yambo code. The aspect of phonon frequencies series calculation caused by atoms displacement were studied using the Phonopy code in order to evaluate the dynamic stability of structures.

3rd section

Outcomes of research

✉ Faculté des Sciences, avenue Ibn Battouta, BP. 1014 RP, Rabat –Maroc
☎ 00212(05) 537 77 18 34/35/38, 🖷 00212(05) 537 77 42 61, http://www.fsr.ac.ma

Third Section-Introduction

Hybrid perovskites has emerged as new competing semi-conductor materials in the photovoltaic application[181]. These materials exhibit impressive properties such as the high mobility and diffusion of carriers, low recombination rate, high absorption in the visible region, tunable bandgap, low effective mass, and low-cost manufacturing[182-188]. They have been used as an absorbing layer in solar cells and have demonstrated in just a few years[189] a high efficiency that exceeds 25%. Currently, these compounds' degradation, instability, and toxicity are the shortcomings that lead to the efficiency dwindling of solar cells based on hybrid perovskite[190,191]. Studies reveal that defects, ion migration, moisture, O_2, and light are the main factors causing this degradation, thus, efficiency reduction[192-196]. Different kinds of degradation mechanisms have been suggested and investigated in various studies[197-198]. It is noted that O_2 alone does not induce the perovskite degradation[199]. Studies suggest that hybrid perovskite degrades in dry air in the presence of both oxygen and light[200]. This degradation is due to the formation of superoxide in the perovskite framework which are induced by the light effect. In particular, this degradation process that causes the hybrid perovskite breakdown occurs as follow: the strong Pb-O bonds lead to the disintegration of Pb-I bonds, furthermore, O atoms tend to bond with two Pb atoms by replacing iodine atoms[201]. However, experimental studies discovered that doping iodine (I) with bromine (Br) shows the improvement of the hybrid perovskite stability[202,203]. Meanwhile the understanding of the halogen mixing on the enhanced stability did not undergo any furthermore examination. A deep study on the bromine influence on the $MAPbI_3$ properties will be discussed in this section. On the other hand, Ni el al. have demonstrated the crucial influence of defects in the perovskite layer specifically regarding the stability and hybrid perovskite solar cells performance[204]. In $MAPbI_3$ defect can be either vacancies (V_{MA}, V_{Pb}, V_I), interstitials (MA_i, Pb_i, I_i), cation substitutions (MA_{Pb}, Pb_{MA}), or anti-site substitutions (MA_I, Pb_I, I_{MA}, I_{Pb})[205]. Depending on the defect nature, the above can create a shallow donor or acceptor energy level in the surface band structure[206]. Furthermore, deep trap behavior levels can be also formed close to the middle of the band gap through the formation of vacancies which facilitates the charge carrier recombination resulting in the decrease of both carrier lifetime and the open circuit voltage[207]. However, shallow trapped states positioned near to the CBM or VBM are shown to reduce the charge carrier mobility[208]. Both experimental and theoretical studies show that iodine defect results in the deep

electron and hole trapping levels inside of the band gap (mid-gap states), that act as centers for non-radiative recombination[209]. Besides superoxide ion (O_2^-) species are shown to replace the iodine vacant site in the hybrid perovskite surface which induces the fast degradation of the perovskite system[210]. It is widely recognized that different hybrid perovskite degradation pathways can take place depending on the environment conditions and gas molecule adsorbed leading to reversible or irreversible material destruction[211-212]. Under the effect of water, hybrid perovskite can undergo a decomposition to both organic and inorganic components[213]. Particularly, experimental studies have noticed that $MAPbI_3$ is converted to PbI_2 when it is present in air at 60% ambient humidity at dark conditions, this conversion is less pronounced in vacuum condition[214]. Myriad of studies have focused on investigating the mechanism of moisture-induced hybrid perovskite degradation[215-216]. A study of the water-$MAPbI_3$ interaction by molecular dynamics revealed that the dissociation of $MAPbI_3$ is triggered by the initial step of iodine ions detachment which attempt to detach themselves from the surface of the perovskite[217]. It has been proposed also that the irreversible degradation can be triggered by trapped charges in perovskite crystal at grain boundaries under the presence of moisture[198]. Kwak et al. demonstrated that no degradation occurs for hybrid perovskite in the presence of moisture and absence of charge generation caused by light[218]. In contrast, they showed that in positively or negatively charged crystal, the perovskite underwent a decomposition through the organic cation dissolution or dissociation of iodide anion respectively. Organic cation dissolution occurs due to the H_2O and CH_3NH_3 (MA) interaction through hydrogen bonds leading to the NH_3 deprotonation, thus, the structure destruction[219]. A new approach to mitigate the perovskite water interaction for a stable hybrid perovskite solar cells will be discussed in detail later in this section. Besides the mixture of organic cation plays a crucial role in enhancing the perovskite stability[220]. Organic cation plays a huge role in identifying large properties of hybrid perovskite, furthermore, their incorporation helps in reducing ion migration in the crystal[221]. On the other hand, hydrogen vacancies created by the cation organic are shown to act also as a non-radiative recombination center limiting the hybrid perovskite devices performance[222]. Controlling the formation of this hydrogen vacancies can be established by replacing MA cation in $MAPbI_3$ by the organic FA, where theses vacancies have been known to hardly form, making $FAPbI_3$ more stable and higher performing in photovoltaic applications[222]. The high efficiency achieved by the hybrid perovskite was showed by lead halide perovskites that represent toxicity[223-224], which blocks the commercialization of these compounds. The substitution

of lead by tin in both $FAPbI_3$ and $MAPbI_3$ has demonstrated an efficiency of 5.51% and 3.13% respectively[225], while the substitution of lead by Ge in $MAPbI_3$ shows an efficiency of 0.2% and doesn't show any photocurrent for $FAGeI_3$[226]. So far no substitution of lead has demonstrated a better performance than the $MAPbI_3$. In the following we will discuss the power conversion efficiency of the less free lead halide perovskite $FAPb_{0.5}Sn_{0.25}Ge_{0.25}X_3$ (X= I, Cl and Br) crystals in the case of partial substitution of lead by both tin and germanium, and where the halogen (I, Br, Cl) was swapped for iodine, bromine and chlorine.

Chapter I

Somme approaches for reducing the hybrid perovskite degradation processes

I. Introduction

The main focus of this chapter is understanding the degradation mechanism of hybrid perovskite as well as enhancing and reducing their degradation processes. The first part is devoted to the investigation of the bromine doping effect on $MAPbI_3$. In this research, the $CH_3NH_3PbI_3$ doped by bromine (Br) in different sites was theoretically investigated using the density functional theory (DFT). For this purpose, the electronic, electrical conductivity, and optical properties of $CH_3NH_3PbI_3$ and $CH_3NH_3PbI_2Br$ were studied. In addition, the dynamical properties of the two compounds were studied by the phonon spectrum calculation, in order to acknowledge the stability rate of these doped systems. On top of that, to better understand the influence of the oxygen (O) molecule, on the methylammonium lead halide perovskite degradation, we investigated the interaction of oxygen (O) with both $CH_3NH_3PbI_3$ and $CH_3NH_3PbI_2Br$ compounds. The second part is dedicated to a detailed study of the influence of vacancy and humidity on the degradation of hybrid perovskite. As a rational approach to diminish the toxicity and increase the stability of these compounds, we herein report by simulations within the framework of DFT the doping effect of lead by both tin and germanium on the hybrid perovskite stability. For this purpose, we investigated the energy vacancy formation in different sites of the $CH_3NH_3PbI_3$ and $MAPb_{0.5}Sn_{0.25}Ge_{0.25}I_3$ perovskite compounds as well as we evaluated their influence on the surface band structure. Further, we studied the adsorption energy of water molecule on different sites of both compounds with the presence of vacancies and in the defect free systems. The adsorption of the water molecule has been made above diverse sites positions where the initial hydrogen atom of water molecule is pointing downward. The charge density distribution was also evaluated to illustrate the interactions between H_2O and the perovskite surfaces.

II. Degradation mechanism of $CH_3NH_3PbI_3$ and enhancing its optical absorption through variety of doping sites

1. Structural and physical properties of $CH_3NH_3PbI_3$ and $CH_3NH_3PbI_2Br$

The hybrid perovskites $CH_3NH_3PbI_3$ and $CH_3NH_3PbI_2Br$ structures are illustrated in Fig.I. 1. The pseudo-cubic structure of $CH_3NH_3PbI_3$ consists of an octahedral cluster of lead where each Pb is surrounded by 6 iodine (I) atoms. The Methylammonium CH_3NH_3 cation is surrounded by 8 octahedral PbI_6. The bromine (Br) doping was performed at three non-equivalent iodine (I) sites (Br', Br'', Br''').

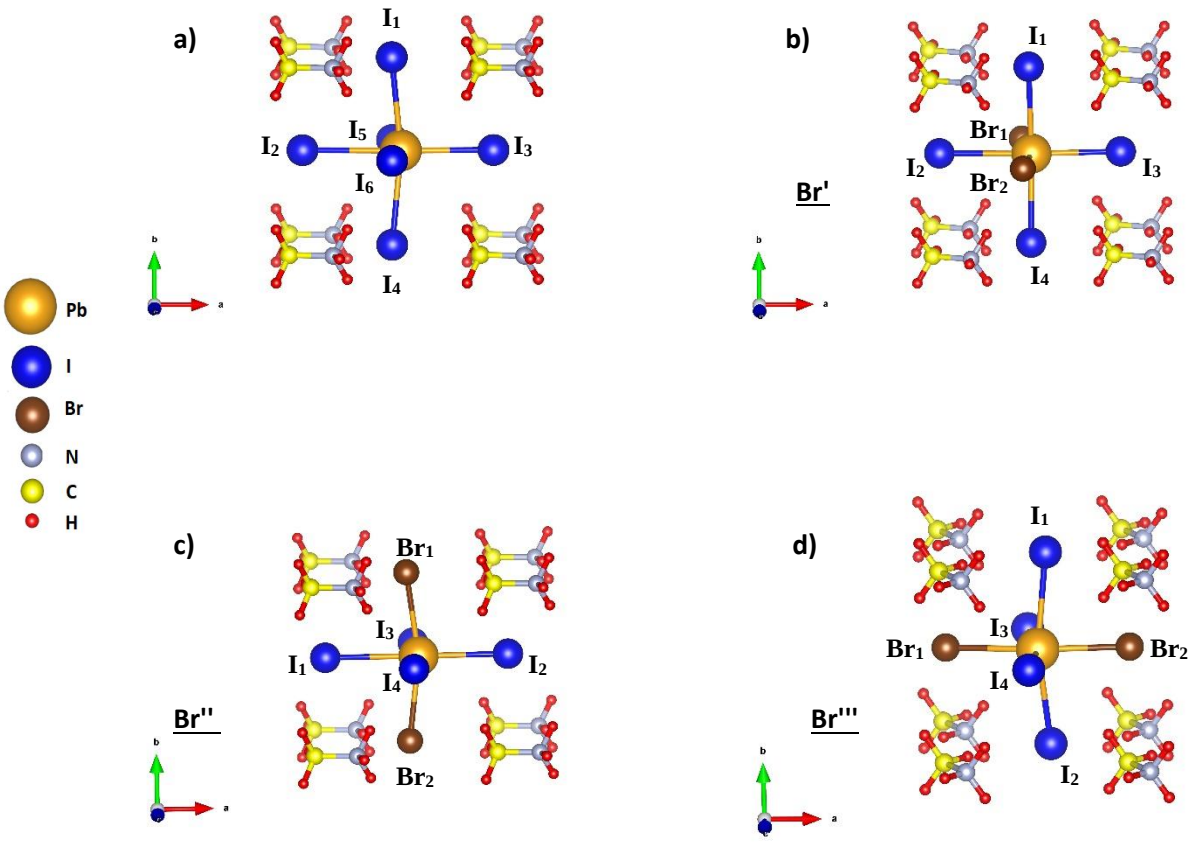

Fig.I. 1. Pseudo-cubic structure of (a) $CH_3NH_3PbI_3$,(b) $CH_3NH_3PbI_2Br'$, (c) $CH_3NH_3PbI_2Br''$ and (d) $CH_3NH_3PbI_2Br'''$

Fig.I. 1a shows the pseudo-cubic structure of $CH_3NH_3PbI_3$, where lead (Pb) occupies the center of the octahedra and is surrounded by six iodine (I) atoms. It is clearly seen from Fig.I. 1 (a) that the PbI_6 cage demonstrates a tilting towards the NH_3 cation. When doping with bromine (Br) in the

Br' site, the diagonal I_1-Pb-I_4 becomes almost untitled (Fig.I. 1 (b)), which comes down to the larger electronegativity of bromine (Br). The doping in Br" site does not show a high effect on the symmetry of the structure. On the other hand, doping in Br"' site shows the rotation of both organic molecule CH_3NH_3 and the I_1-Pb-I_2 angle. Thus, the doping by bromine (Br) in different sites affects the symmetry of CH3NH3PbI3.The cell parameters of the doped structures have decreased as shown in Table.I. 1. This is due to the smaller ionic radius of bromine (Br)[227], and also the shorter Br−Pb bonds when compared with I−Pb bonds as represented in Table.I. 2. The lattice parameters of the structures are in good agreement with other theoretical and experimental studies[228-229].

Table.I. 1. Cell parameters of the pseudo-cubic $CH_3NH_3PbI_3$ and $CH_3NH_3PbI_2Br$ structures

Pseudo-Cubic	Lattice parameters (Å)		
	This work	Other work[228]	Experimental
$CH_3NH_3PbI_3$	a = 6.35 , b = 6.30, c = 6.34	a = 6.33, b = 6.29, c = 6.39	6.27[230]
$CH_3NH_3PbI_2Br'$	a = 6.33, b = 6.25, c = 5.99	a = 6.35, b = 6.27, c = 6.08	6.18[229]
$CH_3NH_3PbI_2Br''$	a = 6.37, b = 5.94, c = 6.33	a = 6.36, b = 5.98, c = 6.41	
$CH_3NH_3PbI_2Br'''$	a = 5.92, b = 6.27, c = 6.39	a = 6.01, b = 6.27, c = 6.44	

Table.I. 2. Bond lengths of $CH_3NH_3PbI_3$ and $CH_3NH_3PbI_2Br$ structures

bond length (Å)	Pb-I_1	Pb-I_2	Pb-I_3	Pb-I_4	Pb-(Br_1 or I_5)	Pb-(Br_2 or I_6)
$CH_3NH_3PbI_3$	3.17	3.27	3.08	3.17	3.19	3.18
$CH_3NH_3PbI_2Br'$	3.13	3.22	3.12	3.13	3.04	2.98
$CH_3NH_3PbI_2Br''$	3.25	3.11	3.18	3.15	2.99	2.99
$CH_3NH_3PbI_2Br'''$	3.15	3.16	3.30	3.12	2.98	2.95

After the optimization of the lattice parameters, we evaluated the band structure. Fig.I. 2 shows that $CH_3NH_3PbI_3$ and $CH_3NH_3PbI_2Br$ have a semiconductor characteristic. With the substitution of bromine (Br), the gap remains direct and shows an increased value of 1.62 eV for the doping in Br' site, 1.6 eV in Br" and 1.7 eV in Br"' with a direct bandgap of 1.58 eV for $CH_3NH_3PbI_3$ at the R point of the Brillouin zone. Table.I. 3 regroups the band gap values calculated for all structures. They are in good agreement with theoretical and experimental studies[203-52-231].

In order to understand the doped bromine's (Br) effect on the electronic structures, the total density of state (TDOS) and partial density of state (PDOS) were calculated for both $CH_3NH_3PbI_3$ and $CH_3NH_3PbI_2Br$ as shown in Fig.I.3.

Table.I. 3. Band gap of $CH_3NH_3PbI_3$ and $CH_3NH_3PbI_2Br$

Pseudo-Cubic	Band gap (eV)		
	This work	Other work[228]	experimental
$CH_3NH_3PbI_3$	1.58	1.54	1.55[231]
$CH_3NH_3PbI_2Br'$	1.62	1.649	1.64[231], 1.68[13]
$CH_3NH_3PbI_2Br''$	1.6	1.644	
$CH_3NH_3PbI_2Br'''$	1.7	1.647	

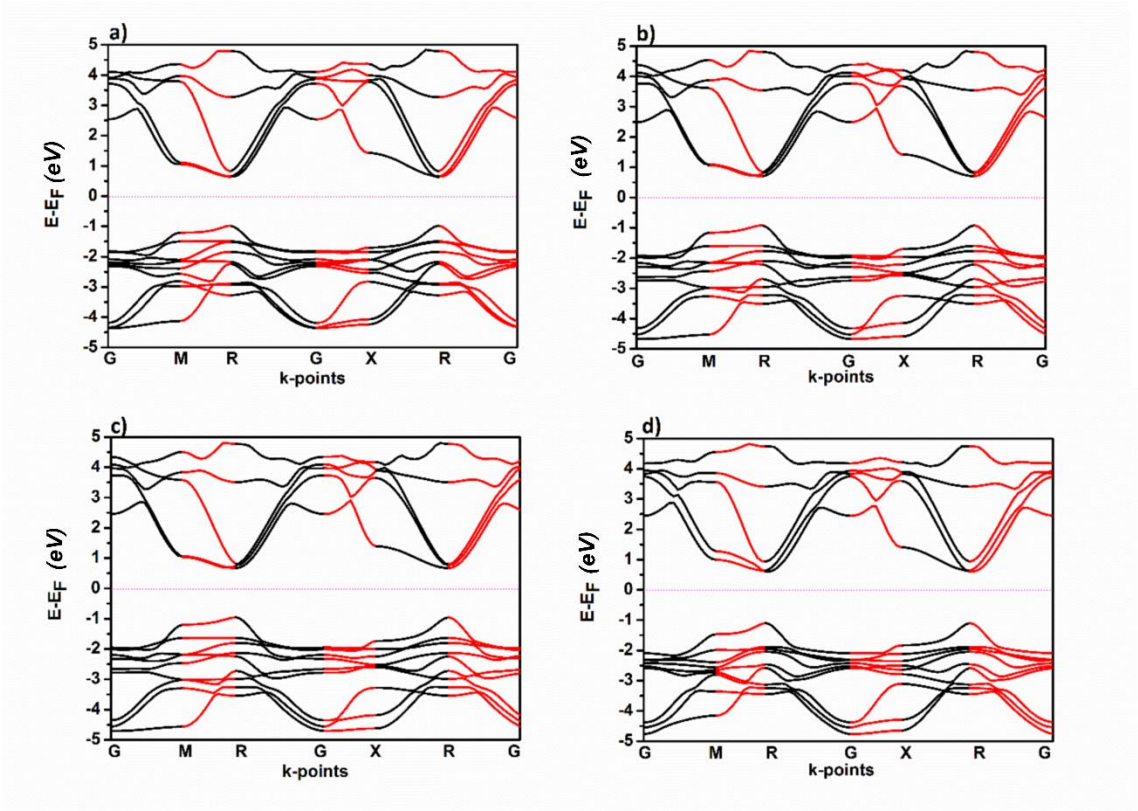

Fig.I. 2. band structure of (a) $CH_3NH_3PbI_3$,(b) $CH_3NH_3PbI_2Br'$, (c) $CH_3NH_3PbI_2Br''$ and (d) $CH_3NH_3PbI_2Br'''$

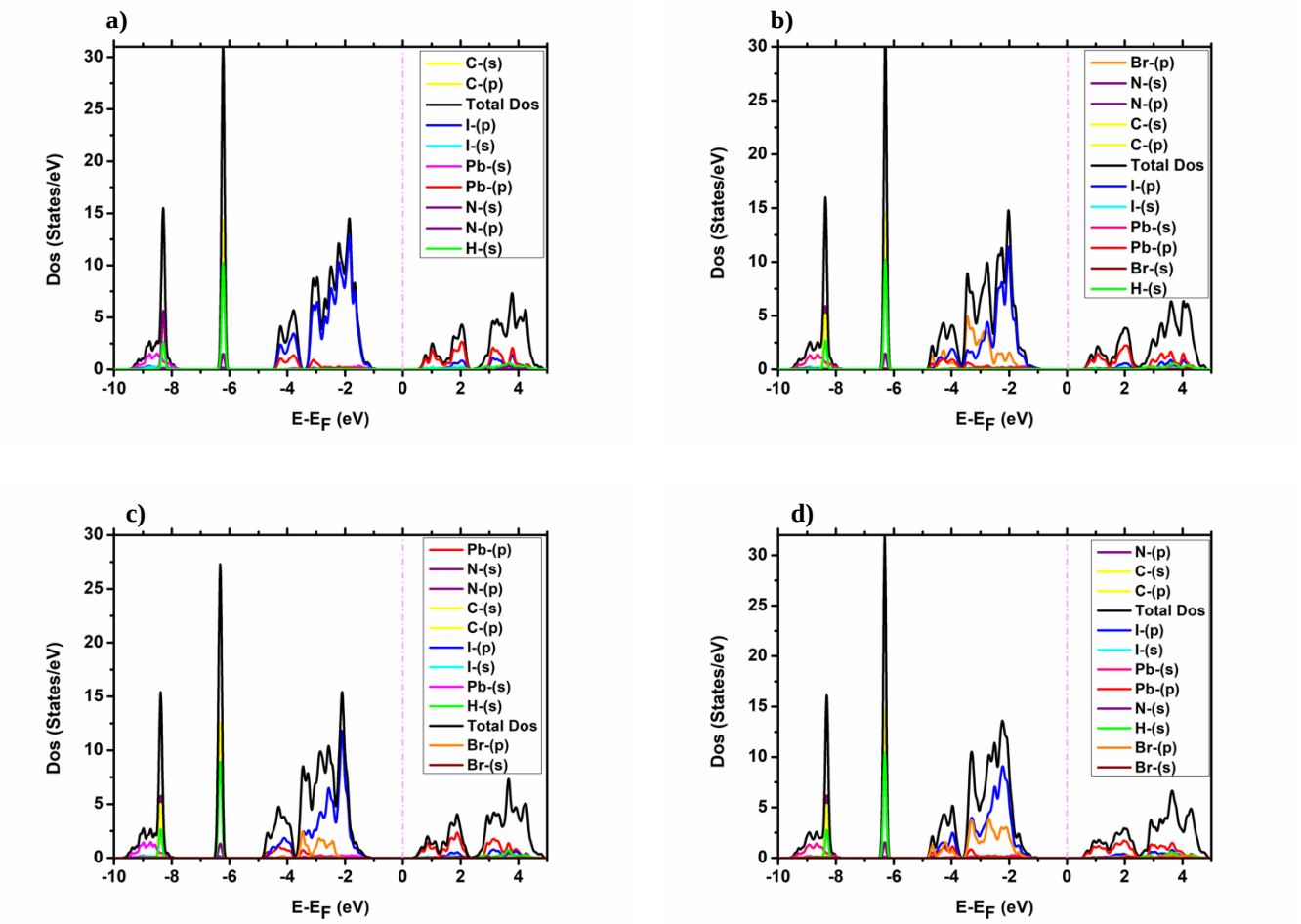

Fig.I. 3. DOS of (a) $CH_3NH_3PbI_3$,(b) $CH_3NH_3PbI_2Br'$, (c) $CH_3NH_3PbI_2Br''$ and (d) $CH_3NH_3PbI_2Br'''$

The Fermi energy level is located in the middle of the conduction and the valence bands and it is represented by the dash-dot in Fig.I. 3, which shows that the density of state (DOS) of the three $CH_3NH_3PbI_2Br$ structures is similar. The main difference appears in the middle gap of the conduction band minimum (CBM) and the valence band maximum (VBM). The CH_3NH_3 cation's states are located far from the CBM and the VBM for all the partial density of state as in the pure compounds[232], suggesting that the role of organic ions in the term of electronic properties is only to maintain neutrality. The orientation of this organic part and the bonding it establishes with the inorganic part plays an important role to defend the properties of this material, and indirectly influences the efficiency of this device[233-234].

The CBM of $CH_3NH_3PbI_3$ is mainly dominated by the Pb-p orbital with negligible coupling with I-s orbital , while the VBM of $CH_3NH_3PbI_3$ is principally constituted of s orbital of lead (Pb) which

hybridizes with the p orbital of iodine (I). The hybridization between these orbitals results in an antibonding state in both the VBM and the CBM of the $CH_3NH_3PbI_3$ compound , making the upper valence bands dispersive, and it also results in small effective masses for the holes and low effective electron mass[235]. The anti-bonding coupling in the VBM and the CBM tends to break the Pb-I bond and forms a vacant site where the charge trips inside[236]. As a result, non-rapid recombination is guaranteed, making this hybrid perovskite an ideal candidate for thin-film solar cells with a p-i-n configuration[237]. The electronic density changes with the doping of iodine (I) by bromine (Br). Adding the new Br states modifies the overlap between the Pb-I orbitals. As depicted in Fig.I. 3 (b, c, and d), by varying the bromine (Br) doping site we can control the interaction between the Pb, I, and Br orbitals which influences the electronic properties, thus, the band gap. Previous studies have also demonstrated the importance of orbital interactions in determining electronic band structures[238]. However, as indicated in Fig.I. 3, the Br state does not affect the CBM while it contributes to the VBM where the P-Br orbital appears, as also noted by previous investigations[228,239]. The contribution of bromine (Br) in the VBM leads to an increase in the band gap. It has been demonstrated that the valence band region is stabilized by the octahedral tilting which has a correlation with the band gap opening[240]. Thus, the $CH_3NH_3PbI_2Br'''$, which shows the high tilting exhibits the larger band gap, and stabilizes the $CH_3NH_3PbI_2Br$ compounds. Fig.I. 4 shows the variation of the lattice parameters, bond length fraction (ratio between the shortest and longest I-Pb–I bonds depending on the position of I), and bandgap of $CH_3NH_3PbI_3$ and $CH_3NH_3PbI_2Br$ compounds. As can be seen from Fig.I. 4 the lattice parameters and the bond length fraction of $CH_3NH_3PbI_3$ decrease with the effect of bromine (Br) doping while the bandgap increases with the presence of bromine (Br).

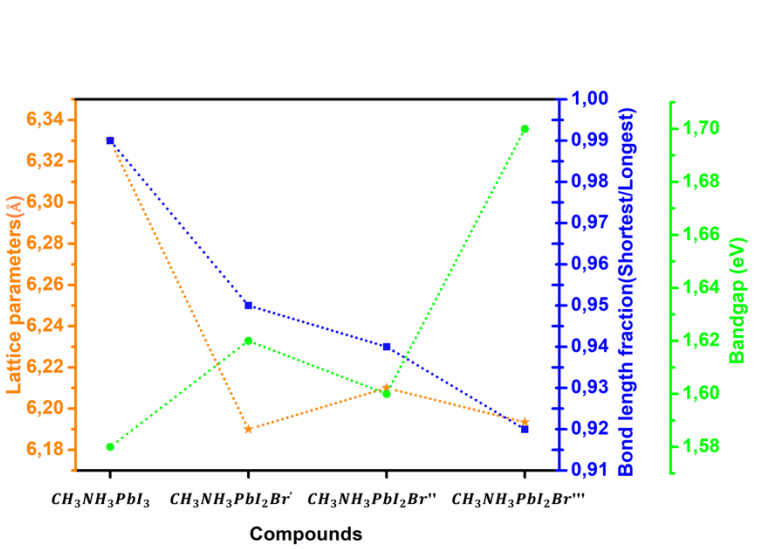

Fig.I. 4. Lattice parameters, bond length fraction, and bandgap variation of $CH_3NH_3PbI_3$ and $CH_3NH_3PbI_2Br$

Furthermore to evaluate the electrical conductivity of these compounds, Boltzmann Transport Theory as implemented in Boltztrap code was used[241]. Fig.I. 5 depicts the electrical conductivity per unit relaxation time (σ/τ) as a function of the carrier concentrations and the chemical potential (μ) at temperatures 300K, 500K, and 800K for $CH_3NH_3PbI_3$ and $CH_3NH_3PbI_2Br$ compounds. The electrical conductivity of all compounds increases with increasing carrier concentration and it decreases with temperature for both electron and hole charge carrier, while it remains constant with the variation of temperature when it is represented as a function of the chemical potential as reported for $CH_3NH_3PbI_3$ in a previous publication[242]. Electrical conductivity was found to decrease upon Br doping. The lowest values are given by the Br''' doping sites while the Br'' doping sites exhibits the largest values, at high values of carrier concentrations. Generally, the electrical conductivity is related to the effective mass by the equation $\sigma = ne\mu$ where $\mu = e\tau/m*$ (n represents the carrier concentration, μ carrier mobility, τ collision time, m^* the effective mass). As shown above, the variation of the effective mass value is related to the band structure (dispersive or flat CBM and VBM), this variation causes the disparity in electrical conductivity value between carrier concentrations. Thus, orbital interaction between atoms which influences the bonding length and the octahedral environment in the compounds have a direct influence on the electrical conductivity[243].

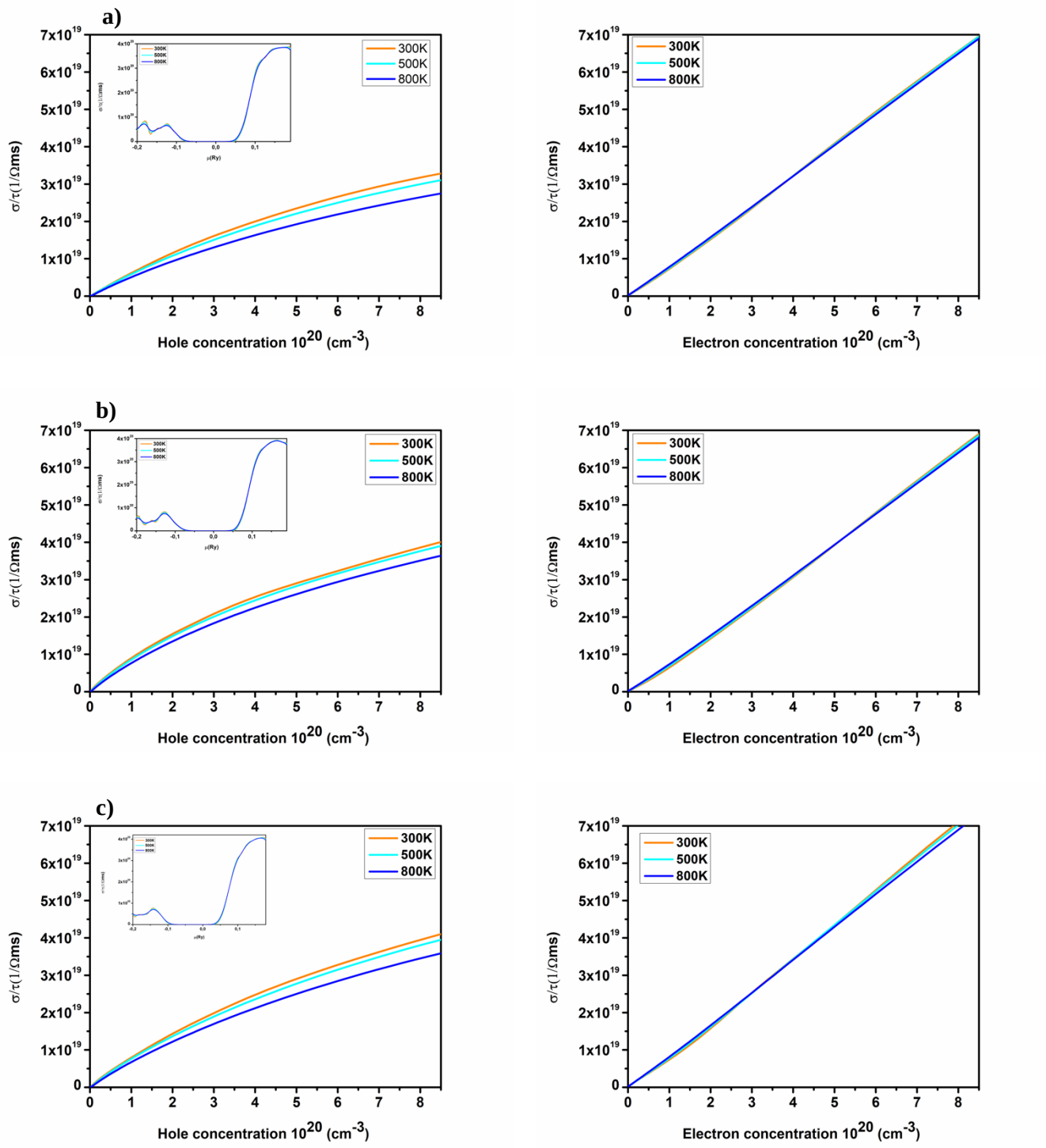
a)
b)
c)
300K
500K
800K
σ/τ(1/Ωms)
Hole concentration 10^20 (cm^-3)
Electron concentration 10^20 (cm^-3)

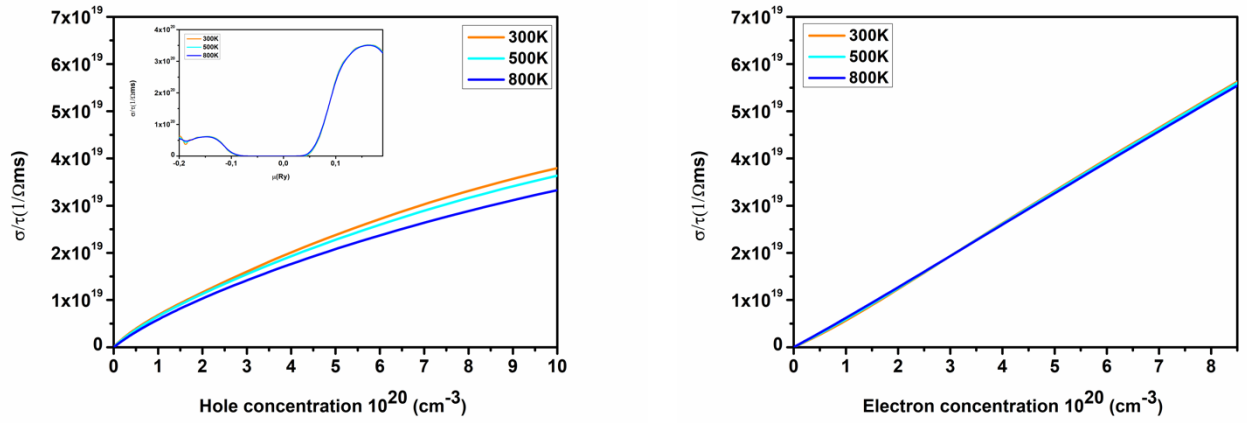

Fig.I. 5. Electrical conductivity of (a) $CH_3NH_3PbI_3$,(b) $CH_3NH_3PbI_2Br'$, (c) $CH_3NH_3PbI_2Br''$ and (d) $CH_3NH_3PbI_2Br'''$

2. Optical properties of non-doped $CH_3NH_3PbI_3$ and doped $CH_3NH_3PbI_2Br$ systems

The calculation of the optical property requires the calculation of the system's disturbance by an electromagnetic wave. The dielectric function has been used for this aim, and is given by the formula; ε= ε'+ i ε'' Where ε' and ε'' represent respectively the real and the imaginary part of the dielectric function. Fig.I. 6 shows the imaginary part of the dielectric function and the absorption coefficient which are given by the equation[244]; $\alpha = \frac{4\pi K}{1240} E$ where $k = \frac{\varepsilon''}{\sqrt{2\varepsilon' + 2\sqrt{\varepsilon'^2 + \varepsilon''^2}}}$

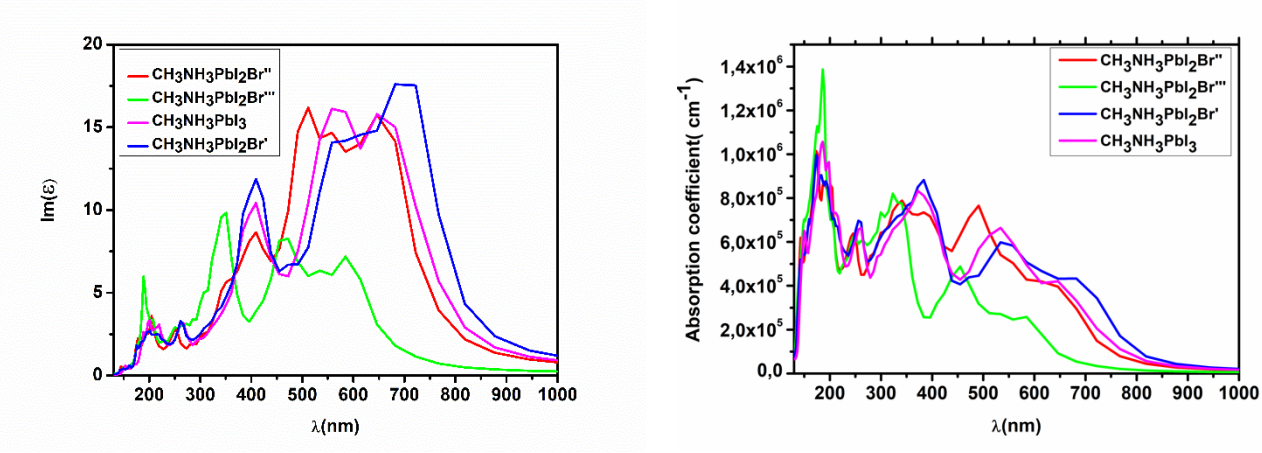

Fig.I. 6. a) Imaginary dielectric function Im(ε) and b) Absorption coefficient of $CH_3NH_3PbI_3$ and $CH_3NH_3PbI_2Br$

The dielectric function describes the response of the material to the incident photons as a function of energy, whereas the absorption coefficient is indicated by the highly localized interband transitions and it gives important information about the efficiency performance of materials. Fig.I. 6 shows that the maximum absorption of all compounds is positioned in the region of the visible light except the $CH_3NH_3PbI_2Br'''$compound. The $CH_3NH_3PbI_3$ demonstrates a high absorption coefficient of 7×10^5 cm^{-1} in the visible light range. This result is in good agreement with theoretical and experimental studies[232-245-246]. The high absorption capacity that exhibits $CH_3NH_3PbI_3$ refers to the transition between the valence mixed states of iodine (I) and lead (Pb) and the conduction states of lead (Pb), both of them demonstrate a high state density that leads to a strong optical absorption[247]. As depicted in Fig.I. 6, the doping by bromine (Br) modifies the optical spectra obtained. As can be seen from the Figure the presence of bromine (Br) leads to a slight shift of the absorption with the stepwise increase of the band gap as reported also by the previous study[248]. The absorption coefficient represented by the doping in Br''' site is low concerning visible light. However, it increases in the region of ultra-violet and shows a maximum absorption coefficient value of 1.4×10^6 cm^{-1}in this range. The doping in Br'' site presents practically similar absorption character of the pure phase in the region from 150 nm to 375 nm and from 650 nm to 1000 nm. The absorption coefficient of the doping in this site (Br'') shows a maximum value of $7{,}6 \times 10^5$ cm^{-1} in the region of the visible light. The doping in the Br' site increases the absorption compared to the pure phase. From the optical absorption coefficient, it can be noted that Br' takes a maximum value of 8×10^5 cm^{-1} in the visible light range and presents the higher value of all compounds in this region. Consistent with previous reports, the band gap and the optical spectra of hybrid perovskite can be tuned by changing the ratio I/Br[249]. In addition, this study reveals that they can be furthermore tuned by varying the doping site to raise the absorption coefficient Thus, the spectrum absorption analysis shows that the doping site position is an important factor to enhance the optical properties and the power conversion efficiencies. Also, due to the strong absorption, these compounds need less thickness to capture solar energy[250]. Because visible light is the most efficient part of the complete solar spectrum, and the high absorption in this range is essential to obtain high efficiency's cells, the doping in Br' and Br'' sites remains the best candidate to enhance the stability of this material and to take advantage of the solar spectrum.

3. Mechanical stability study of both $CH_3NH_3PbI_3$ and $CH_3NH_3PbI_2Br$ systems

The study of mechanical stability is primordial to understand the properties of crystalline materials. Thus, the phonon calculation was investigated to study the system's stability. After the generation of displacement and constant force, a harmonic approximation was used to solve the eigenvalue problem of dynamical matrix D(q) which gives the phonon frequency[251]. Harmonic approximation showed a negative eigenvalue when the system demonstrated an instability, and a positive eigenvalue in the contrast case[251].

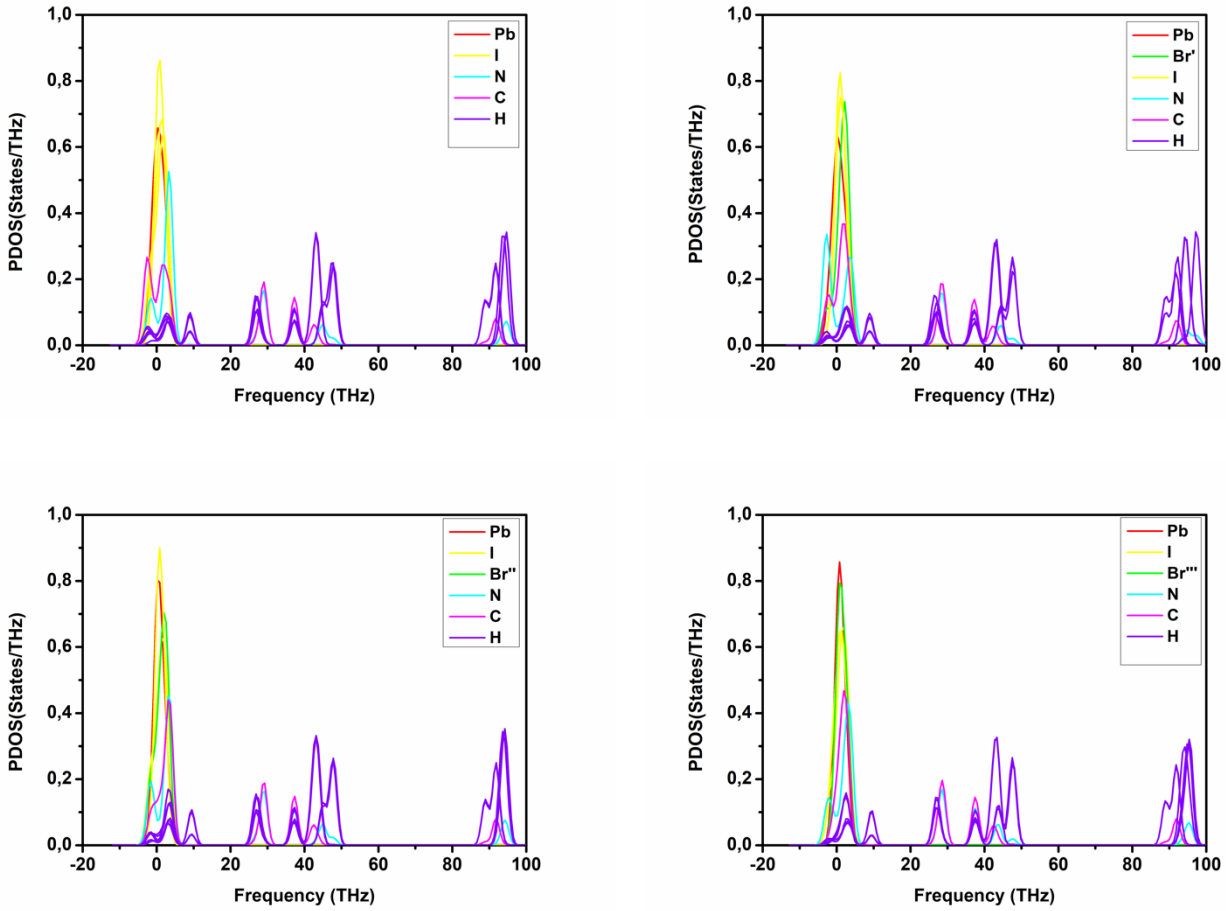

Fig.I. 7. partial phonon density states of $CH_3NH_3PbI_3$ and $CH_3NH_3PbI_2Br$

In this section the partial phonon density of $CH_3NH_3PbI_3$ and $CH_3NH_3PbI_2Br$ have been studied, the results are plotted in Fig.I. 7. The partial phonon density shows three branches due to the mass difference and the bonds between the atoms. The low frequency systems are caused by the vibration

of both organic and inorganic parts. In all states, there is a very small contribution of negative frequency which demonstrates that the three positions doped can exist experimentally. These results show that even in doped $CH_3NH_3PbI_3$, the mechanical stability of the system is not affected, which makes it easy for the experimental process, because there is no phase transition.

The $CH_3NH_3PbI_2Br$ and $CH_3NH_3PbI_3$ have respectively the same dynamical stability, and even with the substitution of iodine (I) by bromine (Br) , there is a presence of a weak imaginary mode. From this last result, we may deduce that this dynamical instability does not have a great influence on the materials degradation.

4. Unraveling oxygen degradation mechanism in hybrid perovskite

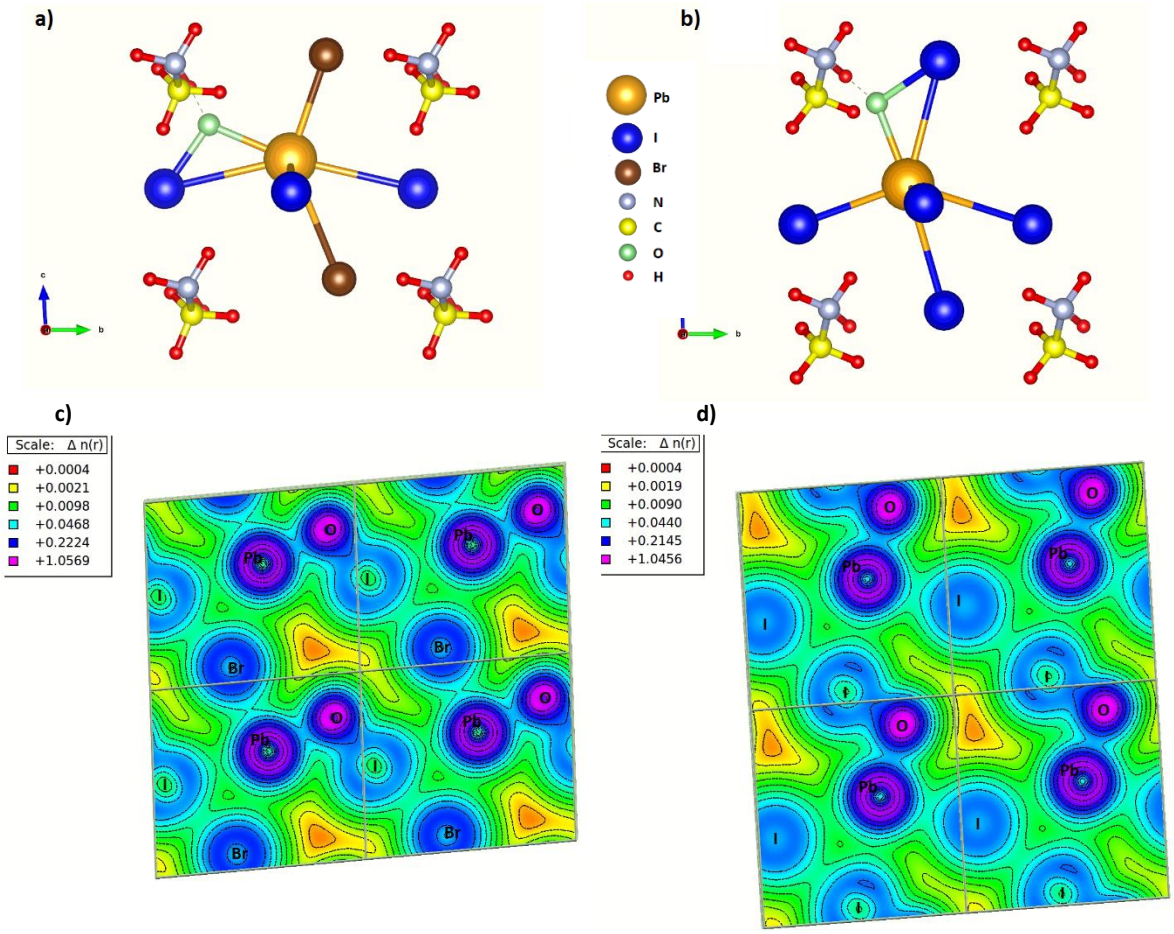

Fig.I. 8. structure of (a) $CH_3NH_3PbI_2Br$'-O, (b) $CH_3NH_3PbI_3$-O, and charge density of (c) $CH_3NH_3PbI_2Br'$-O, (d) $CH_3NH_3PbI_3$-O

In this section, in order to study the interaction between oxygen (O), iodine (I), and bromine (Br) we used an interstitial site in the tetrahedral site of $CH_3NH_3PbI_3$ and $CH_3NH_3PbI_2Br$ at the (0.5 0.25 0.75) position. Structural properties and the charge density of the $CH_3NH_3PbI_3$-O and $CH_3NH_3PbI_2Br$-O structure were investigated and represented in Fig.I. 8. Fig.I. 8 (b) shows that oxygen (O) in the $CH_3NH_3PbI_3$ system tends to interact with iodine (I), lead (Pb) and hydrogen (H), resulting in the displacement of inorganic element toward the organic molecule. With bromine (Br) doping in the $CH_3NH_3PbI_2Br$ system (Fig.I. 8-a), we can clearly notice that the O-Br bond is not favorable, and the displacement of the inorganic part becomes limited. Fig.I. 8 (d) represents the charge density between the inorganic element of $CH_3NH_3PbI_3$, it shows that oxygen (O) makes an ionic bond with iodine (I), confirming that oxygen (O) acts under this hybrid perovskite as an acceptor dopant[252] that can also be seen in Table.I. 4. Comparing the charge density of Fig.I. 8 (c) to 8 (d) shows a decrease of charge around lead (Pb), due to the transfer of charge between bromine (Br) and lead (Pb). Thus, bromine (Br) tends to make a covalent bond with lead (Pb), which makes an electrostatic equilibrium in this structure, thus, improving the system stability.

Table.I. 4. Bader atomic charges of $CH_3NH_3PbI_3$, $CH_3NH_3PI_3$-O and $CH_3NH_3PbI_2Br$-O

Element	$CH_3NH_3PbI_3$	$CH_3NH_3PI_3$-O	$CH_3NH_3PbI_2Br$-O
Pb	**+ 0.9**	**+ 1.01**	**+ 1.07**
I_1/Br	**- 0.55**	**+ 0.75**	**- 0.58**
I_2	**- 0.54**	**- 0.47**	**+ 0.81**
I_3	**- 0.57**	**- 0.55**	**- 0.54**
O	**----**	**- 1.49**	**- 1.50**
CH_3NH_3	**+ 0.76**	**+ 0.74**	**+ 0.74**

III. New approach to mitigate the perovskite water interaction for a stable hybrid perovskite solar cell.

1. Structural properties and vacancy in both $MAPbI_3$ and $MAPb_{0.5}Sn_{0.25}Ge_{0.25}I_3$

In this work we have been interested in the orthorhombic $MAPbI_3$ ($MA=CH_3NH_3$) with a Pnma symmetry and the doped system $MAPb_{0.5}Sn_{0.25}Ge_{0.25}I_3$, where the MA molecules are fully ordered and the PbI_6 cage shows a tilting in all three spatial directions (see Fig.I. 9).

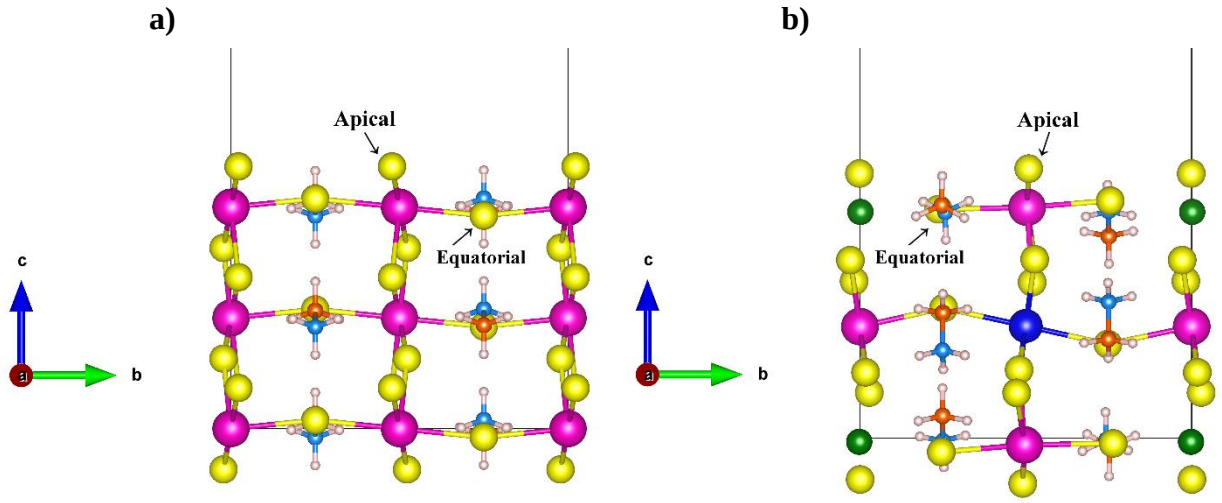

Fig.I. 9. Thin film orthorhombic structures of a) $MAPbI_3$ and b) $MAPbSnGeI_3$ compounds showing the apical and equatorial sites of the iodine ions.

Orthorhombic phase of $MAPbI_3$ is denoted in Glazer notation by $a^-b^+a^-$, indicating an in-phase rotation in the b axes and out-of-phase rotation in both a and c axis[88]. The coordination number of lead (Pb) is six and Pb atom is chelated by six iodine (I) forming an BX_6 octahedra with Pb-I distances of 3.18 Å. Tilting of the halide frame BX_6 has a significant effect on the perovskite optical band gap and carrier effective masses[88]. The octahedral rotation in hybrid perovskite causes the energy to diminish thus lowering the barrier ion migration in hybrid perovskite[101]. This in turn leads to the $MAPbI_3$'s degradation to PbI_2 only. In this context thermodynamic degradation mechanisms have been involved by the creation of iodine molecular defects. Studies suggest that the dissociation of molecular vacancies in the $MAPbI_3$ compound is more favorable for the HI and MAI vacancies[253]. In this order we calculated the dissociation of iodine (I) atom in four different sites. The two positions V_{I1} and V_{I2} are located between two Pb (Pb-I-Pb) in the surface and subsurface respectively. The V_{I3} position is for an iodine positioned between Pb and Ge (Pb-I-Ge),

the last position V_{I4} is for iodine positioned between Pb and Sn (Pb-I-Sn). Structures depicting the different iodine vacancies (V_I) in both $MAPbI_3$ and $MAPbSnGeI_3$ are shown in Fig.I. 10. Table.I. 5 shows the formation energy of the four iodine vacancies.

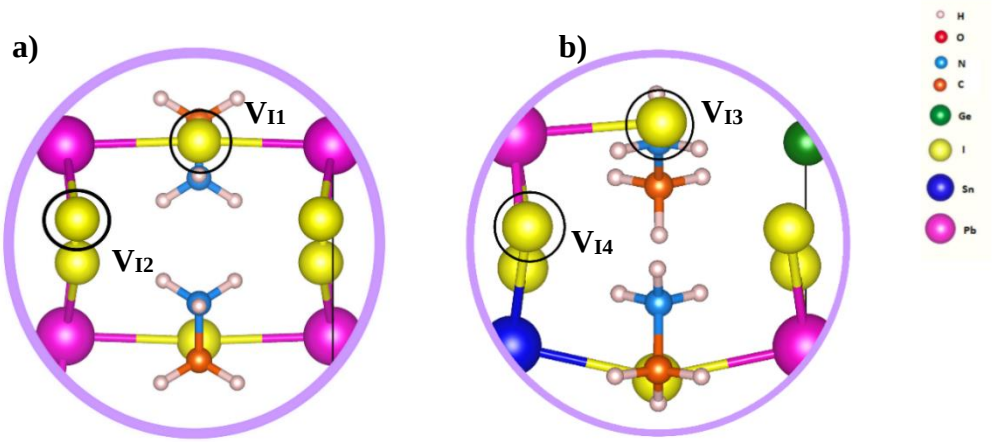

Fig.I. 10. Different Iodine vacancy position in a) $MAPbI_3$ and b) $MAPbSnGeI_3$ compounds.

Table.I. 5. Formation energy of the different iodine vacancies (V_I)

Sites	Formation energy (eV)
V_{I1}	3.10
V_{I2}	3.16
V_{I3}	3.85
V_{I4}	3.72

Results show that V_{I1} at the surface exhibits a low formation energy compared to other iodine vacancies. This discovery matches the previous reports which argue that V_I prefers to occupy the surface of hybrid perovskite layer[254]. It has been observed that the dissociation of $MAPbI_3$ is triggered by the initial step of iodine ions detachment which attempt to detach themselves from the surface of the perovskite[217]. Here, in our simulations we demonstrate that the half doping of Pb by

Sn and Ge leads to a higher energy formation of iodine vacancy at the surface of the $MAPbSnGeI_3$ enhancing their stability. As can be seen from Table.I. 5, I vacancy site at the surface of $MAPbSnGeI_3$ (V_{I3}) shows a higher formation energy than V_I at the subsurface and surface of $MAPbI_3$. The presence of Ge at the $MAPbSnGeI_3$ surface has strengthened the Pb-I-Ge bond resulting in the rising of the V_I energy formation suggesting a relatively limited iodine dissolution from the surface. Furthermore, to gain a clear understanding of the V_I defect on degradation mechanism of this materials, we investigated the band structure associated with the $MAPbI_3$ and $MAPbSnGeI_3$ in the pure and defect phase. The $MAPbI_3$ defect-free phase depicted in Fig.I. 11 shows that $MAPbI_3$ (001) has a direct bandgap of 1.68 eV at the Γ point. The calculated band gap of $MAPbI_3$ is consistent with the experimental report[255]. The doping of lead (Pb) in the $MAPbSnGeI_3$ increases the band gap to a value of 1.72 eV (Fig.I. 11). However, it is apparent that the conduction band maximum (CBM), and valence band minimum (VBM) in the presence of different iodine vacancies shifted toward a lower value. The iodine vacancy defect creates a new shallow energy levels in the CBM. Furthermore, in the case of V_{I4} it appears a manifestation of a new deep traps state located in the middle of the CBM and VBM not far away from the conduction band. The anion vacancy is shallow donor**,** in contrast to V_{Pb} and V_{MA} that are prone to cause the formation of shallow acceptor level[256]. The presence of V_I leads to a delocalized CBM state due to the extension of Pb-6p orbitals (extension of Pb-6p, Ge-4p, Sn-5p in the case of $MAPbSnGeI_3$) around V_I as suggested in a previous study[257]. The p-type V_I originates mainly from the ionic bonding nature of Pb ions and MA. It is also reported that the charges localized inside the deep trap state where carriers get trapped inside making of V_{I4} a nonradiative recombination center[258]. Given these results about the formation energy of V_I and their influence on the surface band structure in the hybrid perovskite $MAPbI_3$ and $MAPbSnGeI_3$, we then investigate the adsorption of water in both defect- free systems and in the presence of these different vacancy sites.

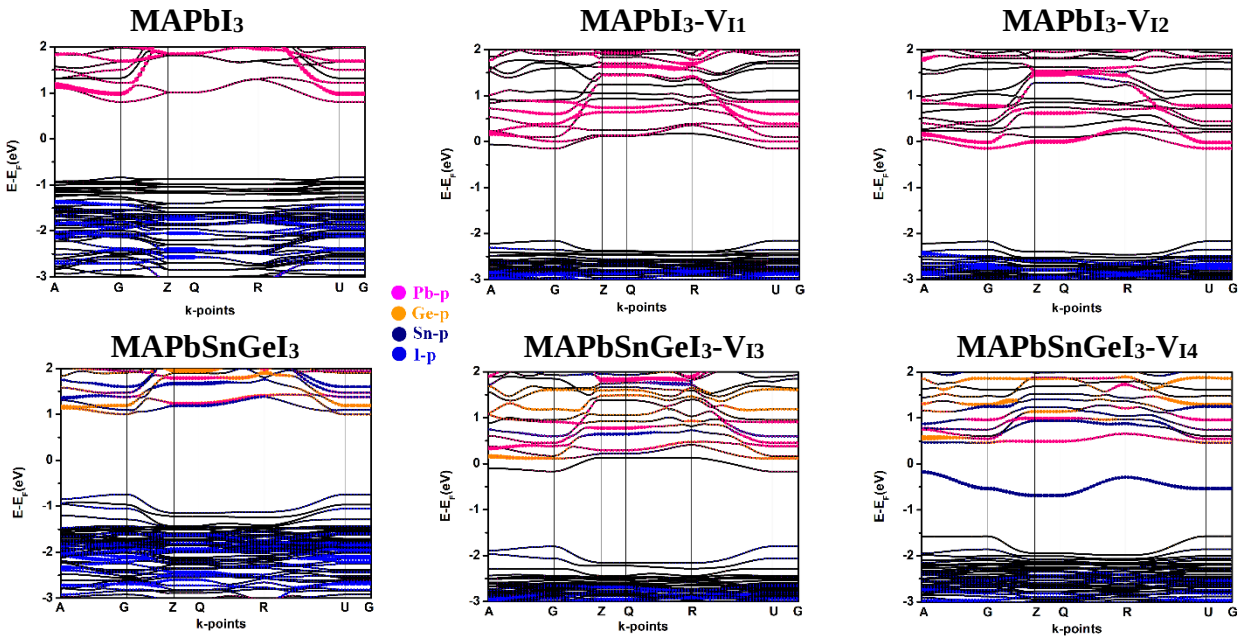

Fig.I. 11. Band structure of $MAPbI_3$ and $MAPbSnGeI_3$ in the pure and defective phase

2. Water adsorption onto $MAPbI_3$ and $MAPb_{0.5}Sn_{0.25}Ge_{0.25}I_3$ structures

The bonding dissociation and the decomposition of hybrid perovskite can be determined by the effect of the water molecules interaction and their dissociation in these materials. As reported in previous studies, the water molecules can be adsorbed easily at the surface of $MAPbI_3$ compound[259]. It can be denoted that two kinds of surface characterize the $MAPbI_3$ compound: The Pb-I terminated surface and the MA-I terminated surface. In our study we have been interested in the MA-I terminated surface where two MA molecules occupy the $MAPbI_3$ surface whom orientation differs. CH_3 is pointing upward for the first MA and downward for the second. The adsorption of water molecule has been calculated for different sites of $MAPbI_3$ and $MAPbSnGeI_3$ surfaces. As depicted in Fig.I. 12 the adsorption positions are Pb, I, Ge, hydrogen atom of CH_3 (H_{CH3}), and hydrogen atom of NH_3(H_{NH3}). Fig.I. 12 demonstrates the after and before interaction between the H_2O molecule and the adsorption sites as well as the calculated charge density distribution in order to concretely illustrate the interactions between H_2O and the perovskite

surface. The adsorption energy calculated and summarized in Table.I. 6 shows negative values which demonstrates that the water molecule can be adsorbed in all of the sites. In the case of CH_3 adsorption on $MAPbI_3$ (Fig.I. 12-CH_3 (a)), we can clearly see that the CH_3NH_3 starts to rotate, and the H_2O molecule moves toward the hydrogen of NH_3 to form an O- H_{NH3} bond of 2.6 Å. Electron density analysis shows that H_2O movement is also motivated by the I-H_{H2O} interaction. This interaction is suppressed in the case of $MAPbSnGeI_3$ system, where H_2O are shown to be static (Fig.I. 12-CH_3 (b)) resulting in the adsorption energy reduction from -0.4 eV to -0.19 eV. Noteworthy, water length bonding diminishes upon the adsorption onto the NH_3 site to 1.7 Å in both compounds. The adsorption on the NH_3 (Fig.I. 12-NH_3) position demonstrates a shorter and stronger O- H_{NH3} bonding, and shows that oxygen tends to attract the H_{NH3} atom than the H_{CH3} atom as reported by previous studies[260,261]. In all adsorption configurations oxygen atoms (O) of water molecules are pointed to the surface except for the iodine atom (I) where the hydrogen atoms are pointing downwards confirming that H_{H2O} prefers to bond with iodine (I) atoms. H_2O adsorbed on I site of $MAPbI_3$ is shown to move towards the apical iodine located at the surface instead of the equatorial iodine site that is positioned between two Pb atoms. It can be noticed that for the $MAPbSnGeI_3$ system, the doping by Ge increases the charge transfer between equatorial I and Ge, thus, strengthening the I bond that makes I atoms stable, leading to the mitigation of the H_{H2O}-I bonding resulting in the diminishment of the adsorption energy in I site of $MAPbSnGeI_3$ (see table 6). Water adsorbed onto Pb site results in both H_{H2O} and O_{H2O} bonding with I and Pb respectively. The charge density between Pb-O (Pb-O = 2.7 Å) in $MAPbI_3$ is mainly shared by the O and Pb atoms forming a covalent bond (Fig.I. 12-Pb(a)). Moreover, it could be seen in Fig.I. 12-Pb(b) that in the doping system ($MAPbSnGeI_3$) a strong interaction Ge-I appears, which induces the reorientation of H_{H2O} that tends to rotate and interacts with the neighboring I atom leading to the break of the N-H_{NH3}-I bonds in $MAPbSnGeI_3$. In comparison with the Pb site, the Ge adsorption site (Fig.I. 12-Ge) showed only a covalent H_{H2O}–Ge bonding, meanwhile the interaction H_{H2O}–I does not occur due to the strong Ge-I bonding and therefore implies the weakness of the adsorption energy in the $MAPbSnGeI_3$ (see Table.I. 6).

- NH_3

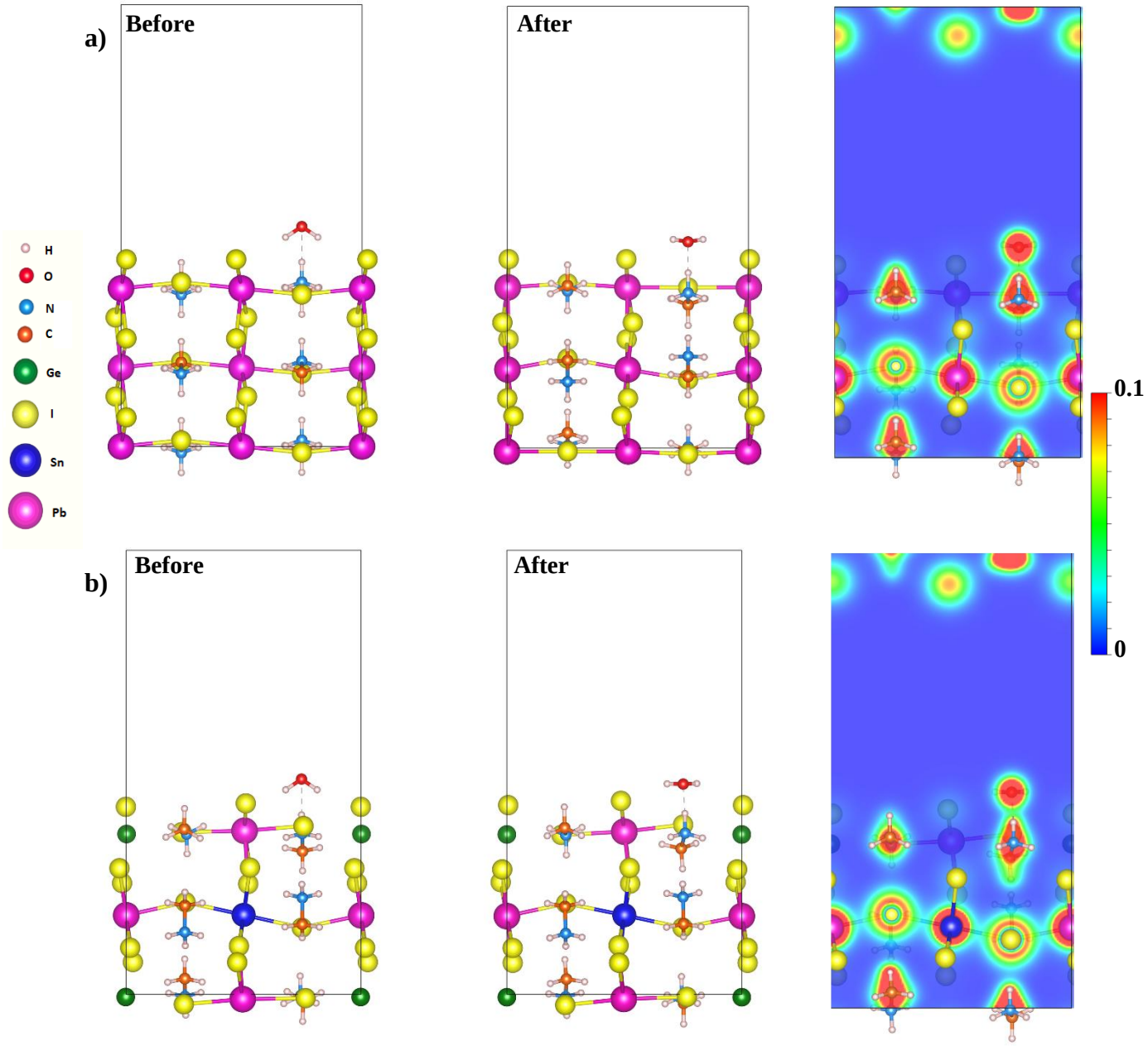

Fig.I. 12. After and before interaction between the H_2O molecule and the NH_3 adsorption site as well as the calculated charge density distribution for a) $MAPbI_3$ and b) $MAPbSnGeI_3$

- CH_3

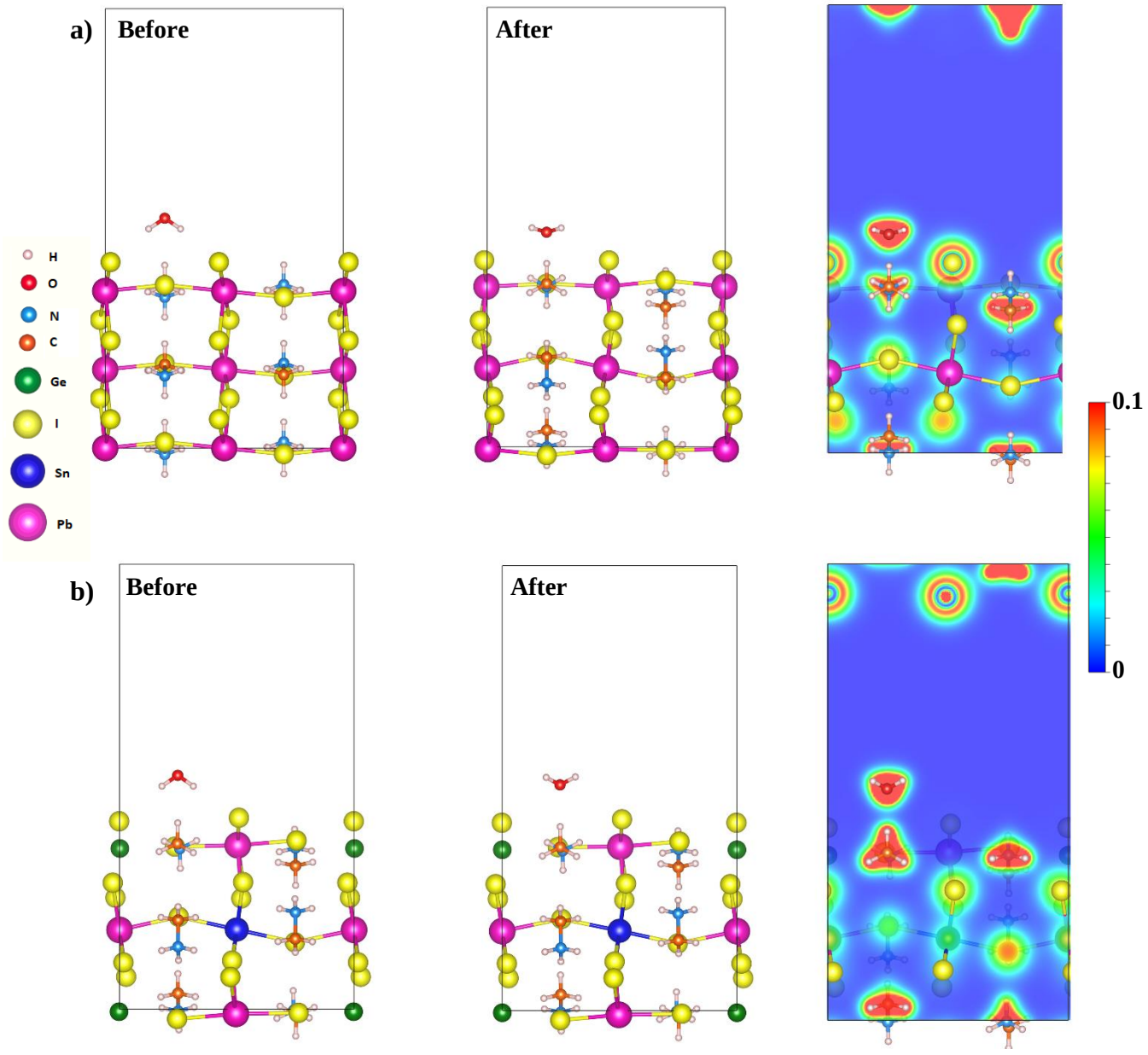

Fig.I. 12. After and before interaction between the H_2O molecule and the NH_3 adsorption site as well as the calculated charge density distribution for a) $MAPbI_3$ and b) $MAPbSnGeI_3$

- I

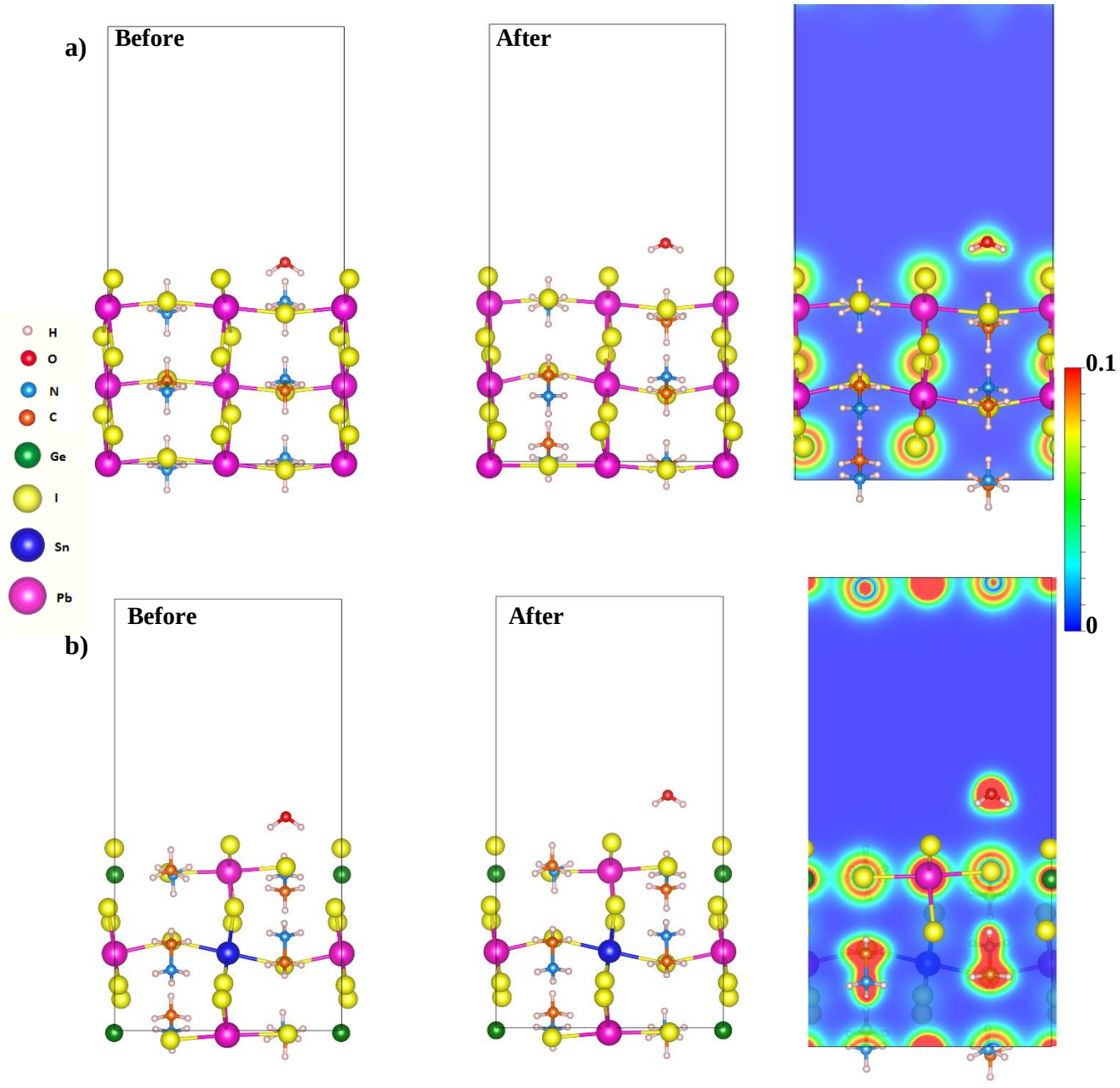

Fig.I. 12. After and before interaction between the H_2O molecule and the NH_3 adsorption site as well as the calculated charge density distribution for a) $MAPbI_3$ and b) $MAPbSnGeI_3$

- **Pb**

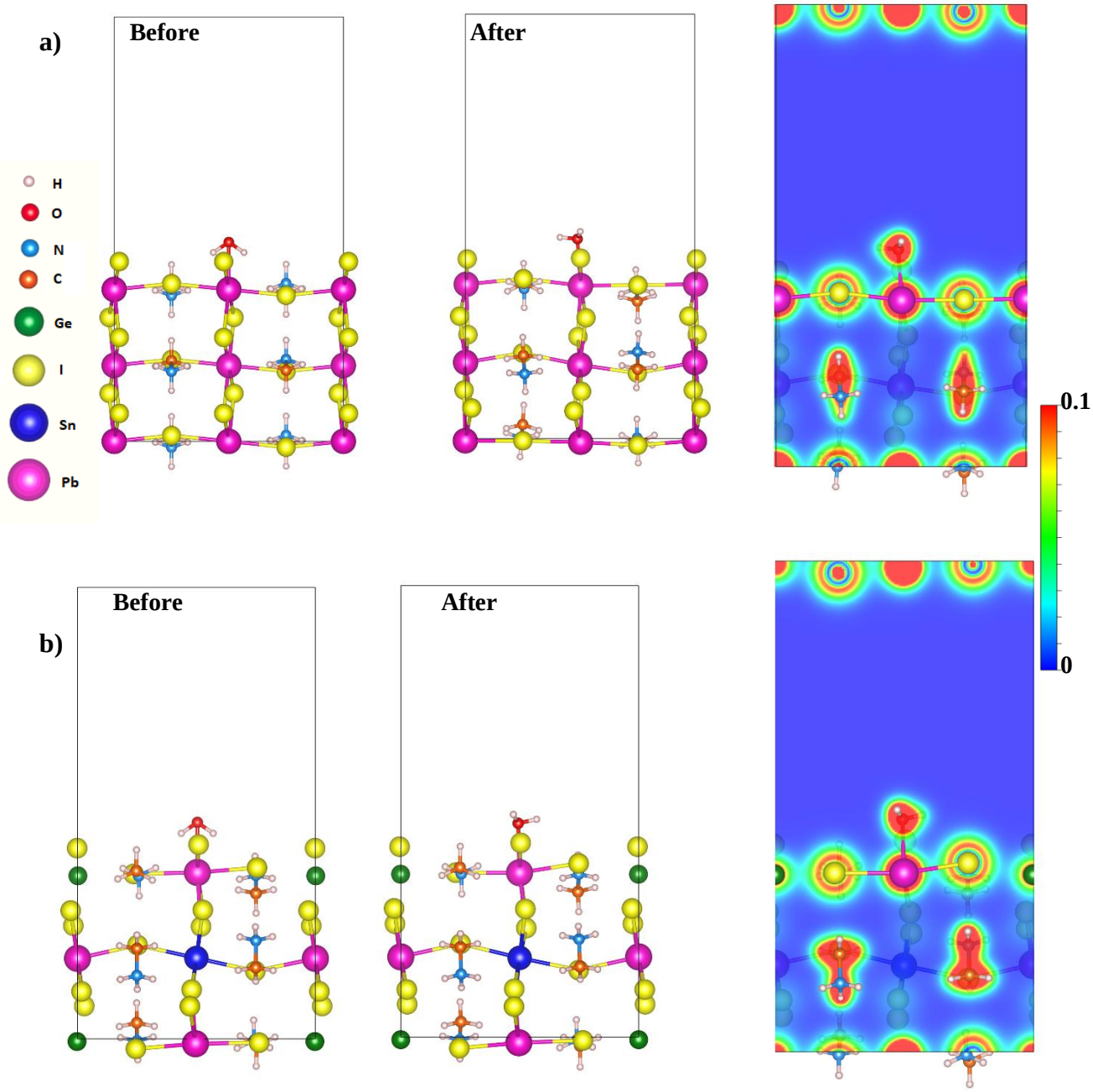

Fig.I. 12. After and before interaction between the H_2O molecule and the NH_3 adsorption site as well as the calculated charge density distribution for a) $MAPbI_3$ and b) $MAPbSnGeI_3$

- **Ge**

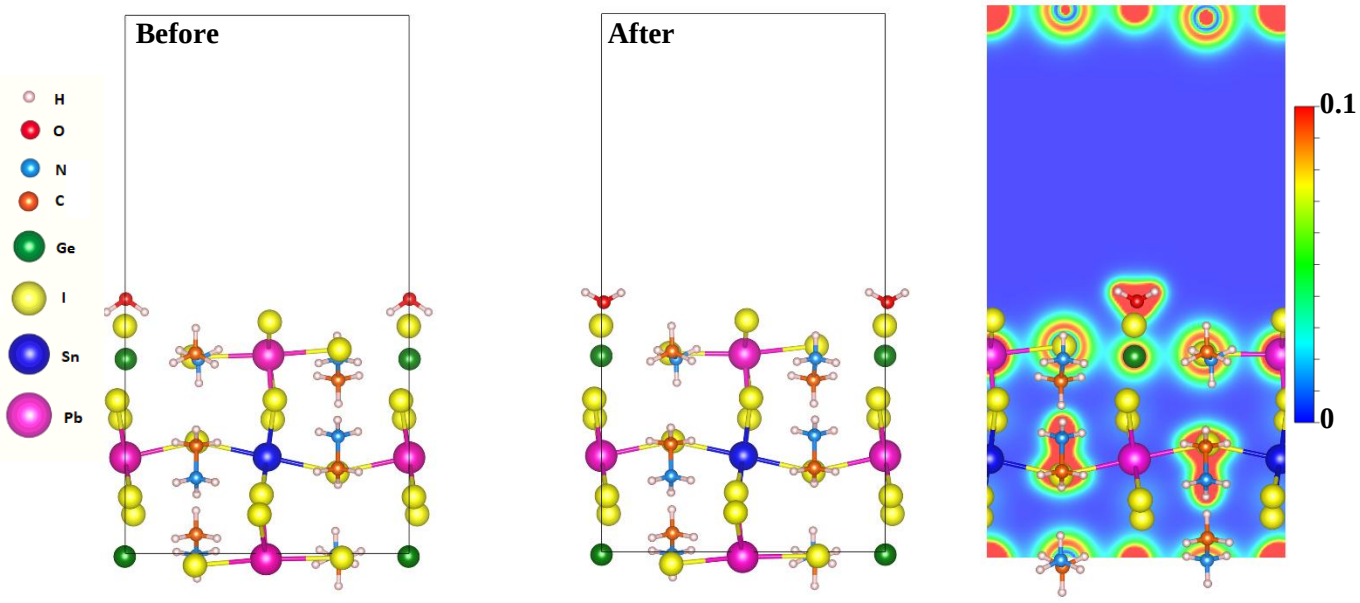

Fig.I. 12. After and before interaction between the H_2O molecule and the NH_3 adsorption site as well as the calculated charge density distribution for a) $MAPbI_3$ and b) $MAPbSnGeI_3$

Table.I. 6. Adsorption energy calculated in the different sites of $MAPbI_3$ and $MAPbSnGeI_3$ compounds.

	Calculated Adsorption energy (eV)	
Sites	**$MAPbI_3$**	**$MAPbSnGeI_3$**
CH_3	**-0.40**	**-0.19**
NH_3	**-0.70**	**-0.70**
I	**-0.24**	**-0.14**
Pb	**-0.56**	**-0.54**
Ge	**----**	**-0.48**
Pb(V_{I1} or V_{I3})	**-0.54**	**-0.50**
Pb(V_{I2} or V_{I4})	**-0.49**	**-0.44**

In summary, results indicate that water adsorption is more favorable in Pb and NH_3 sites suggesting a chemisorption including O- H_{NH3} and O-Pb bonding in the NH_3 and Pb adsorption sites respectively. The strong interaction O-H_{NH3} leads to the deprotonation of the NH_3 forming the volatile CH_3NH_2 that accelerates the perovskite degradation system[262]. Furthermore, we calculated the adsorption energy on Pb site with the presence of iodine vacancy to evaluate their effect on the system degradation (see table 6 (Pb-V_I)). The adsorption energy onto Pb site with the presence of iodine vacancy shows a comparable value with a slightly small difference. This result suggests that water molecules play an indirect role in the degradation of the system. Water molecules can induce the iodine vacancies creation that in turn represents a center of molecule trap which is responsible of the fast hybrid perovskite distortion. In order to further investigate the interaction between water molecule and Pb adsorption site in the presence of iodine defect, the charge density difference of H_2O adsorption was calculated and represented in Fig.I. 13. The system charges density is redistributed mostly around the first layer of the perfect hybrid perovskites ($MAPbI_3$ and $MAPbSnGeI_3$) or the defective perovskite ($MAPbI_3$-V_I and $MAPbSnGeI_3$-V_I) surfaces and H_2O molecules. Negative charge is observed in H_2O molecules and positive one in the perfect and defective perovskite frameworks. As can be seen from Fig.I. 13 the presence of a vacancy defect in the surfaces modifies the charge transfer between the surfaces and H_2O molecules stems from orbital mixing. Some electron charges have been observed to move toward the iodine atoms, which is the result of the binding of H_2O molecule with the iodine atoms forming an I-H_{H2O} bond.

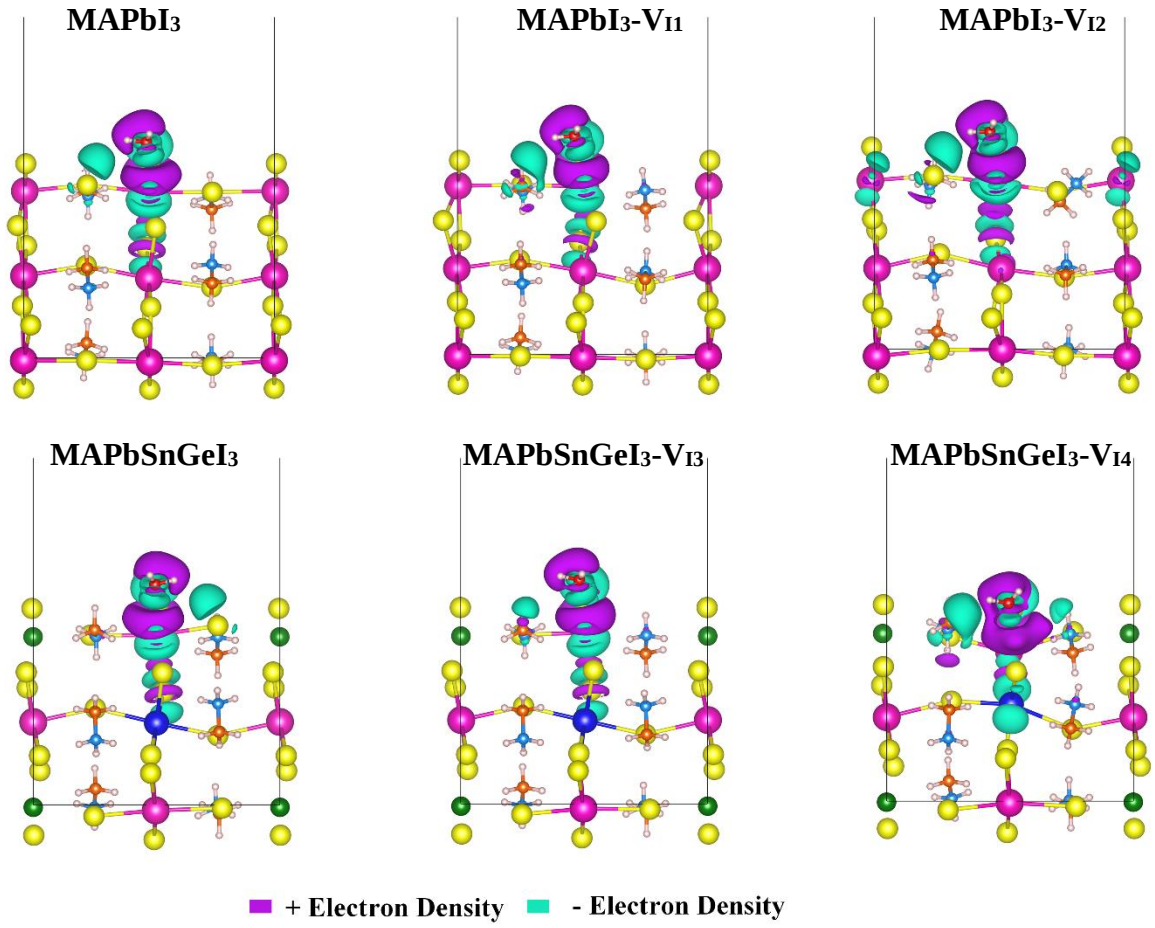

Fig.I. 13. The calculated charge density difference of H_2O adsorption in the perfect and defective $MAPbI_3$ and $MAPbSnGeI_3$ compounds.

3. Conclusion

In summary, we present in this chapter some approaches for reducing the hybrid perovskite degradation processes. The first approach demonstrates that bromine doping in $MAPbI_3$ reduces the hybrid perovskite degradation. This is due to the unfavorable oxygen-bromine bonding that limits the oxygen perovskite interaction. The second approach where the Plomb was half doped by tin and germanium showed the reduction of vacancy formation as well as mitigate the water-perovskite interaction thus enhancing of the structure stability.

Chapter II

$FAPbSnGeX_3$ as potential candidate for photovoltaic application

I. Introduction

This chapter is devoted to the study of new potential materials candidates for photovoltaic application. In order to diminish the toxicity of hybrid perovskite we have been interested in the study of the less lead halide perovskite $FAPb_{0.5}Sn_{0.25}Ge_{0.25}X_3$ (X= I, Cl and Br) where the lead was doped with both Sn and Ge. This study was made using the density functional theory, where the properties of the $FAPb_{0.5}Sn_{0.25}Ge_{0.25}X_3$ (X= I, Cl and Br) were investigated and compared with those of the $FAPbX_3$ (X = I, Br, Cl) compounds. In this work, we systematically studied the structural, electronic, and optical properties of the $FAPbX_3$ (X = I, Br, Cl) compounds and the less lead halide perovskites $FAPb_{0.5}Sn_{0.25}Ge_{0.25}X_3$ (X = I, Br, Cl). We, therefore, discussed their power conversion efficiency. For this purpose, the photovoltaic parameters open circuit voltage and the short circuit current density were investigated.

II. Structural and physical properties of $FAPbX_3$ and $FAPbSnGeX_3$

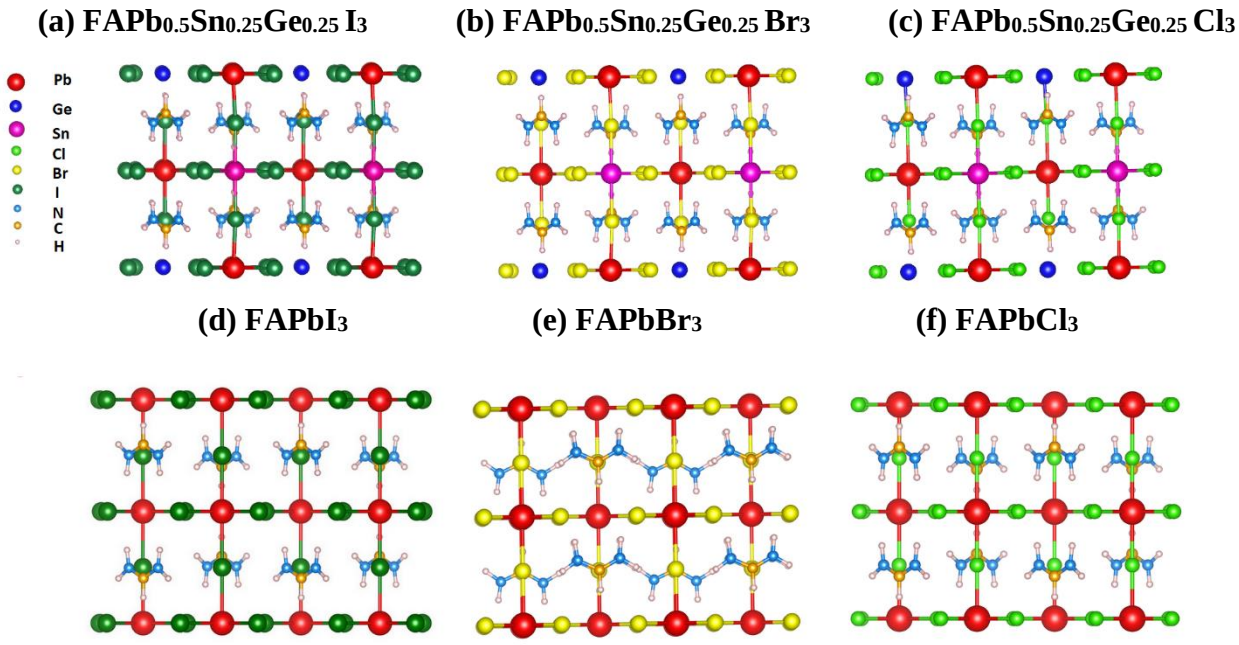

Fig.II. 1. Optimized tetragonal structures $FAPb_{0.5}Sn_{0.25}Ge_{0.25}X_3$, and $FAPbX_3$ structures

The $FAPb_{0.5}Sn_{0.25}Ge_{0.25}X_3$ structures were created by the substitution of 50% of lead (Pb) in $FAPbI_3$ with 25% of tin (Sn) and 25% of germanium (Ge). The halogen (I, Br, Cl) was swapped for iodine, bromine and chlorine. The optimized tetragonal structures and lattice parameters calculated for the $MAPbI_3$, $FAPbX_3$ and $FAPb_{0.5}Sn_{0.25}Ge_{0.25}X_3$ compounds are represented in Fig.II. 1 and Table.II. 1 respectively. Table.II. 1 shows clearly that the substitution of MA with FA changes the lattice parameter from a = 8.75 Å to a = 8.99 Å due to the geometry of FA. The lattice parameters have been reduced with the half substitution of lead by both tin and germanium, and further reduced with the replacement of the halogen with bromine and chlorine. The calculated lattice parameters of $MAPbI_3$, and $FAPbX_3$ are in good agreement with previous experimental and theoretical reports[263,264].

Table.II. 1. Lattice parameters and formation energy of $MAPbI_3$, $FAPb_{0.5}Sn_{0.25}Ge_{0.25}X_3$, and $FAPbX_3$ structures

Compounds	a (Å)	b (Å)	c (Å)	$E_{formation}$(eV)/A
$MAPbI_3$	8.75	8.77	12.89	-4.26
$FAPb_{0.5}Sn_{0.25}Ge_{0.25}I_3$	8.89	8.84	12.34	-4.66
$FAPb_{0.5}Sn_{0.25}Ge_{0.25}Br_3$	8.42	8.36	11.58	-4.8
$FAPb_{0.5}Sn_{0.25}Ge_{0.25}Cl_3$	8.10	8.04	11.14	-4.93
$FAPbI_3$	8.99	8.99	12.72	-4.66
$FAPbBr_3$	8.47	8.47	11.98	-4.76
$FAPbCl_3$	8.17	8.17	11.26	-4.93

The electronic structure study of the compounds consists of analyzing the partial density of states, the band structure and the effective mass. The band structures and the partial state density of the $FAPbX_3$, and $FAPb_{0.5}Sn_{0.25}Ge_{0.25}X_3$ compounds are represented in Fig.II. 2, and 3. The band structures show a semiconductor character with a direct bandgap in the gamma points of the brillouin zone. The difference between the band structures appears in the gap between the valence

band maximum and the conduction band minimum. The calculated energy gap of the $FAPbX_3$ frameworks are 1.5 eV, 1.67 eV, and 2.14 eV for $FAPbI_3$, $FAPbBr_3$, and $FAPbCl_3$ respectively. The valence of $FAPbX_3$ is formed by p-orbital of halogen (I, Br, Cl) while the p-orbital of Pb formed the conduction band. The calculated effective mass of each structure is represented in Table.II. 2. $FAPbCl_3$ presents a larger gap compared to other compounds, a larger effective mass of electrons (Table.II. 2) therefore a low mobility. The latter has improved its performance for photovoltaic application through the half doping of Pb by Sn and Ge, which modified their electronic structures and electronic properties, and slightly altered the energy gap.

The electronic properties of the less free lead halide perovskite $FAPb_{0.5}Sn_{0.25}Ge_{0.25}X_3$ where the lead was doped with both Sn and Ge are depicted in Fig.II. 3. The band structures represent a band gap of 0.98 eV, 1.22 eV and 1.7 eV for $FAPb_{0.5}Sn_{0.25}Ge_{0.25}I_3$, $FAPb_{0.5}Sn_{0.25}Ge_{0.25}Br_3$ and $FAPb_{0.5}Sn_{0.25}Ge_{0.25}Cl_3$ respectively. The valence band maximum (VBM) and the conduction band minimum (CBM) for both compounds $FAPb_{0.5}Sn_{0.25}Ge_{0.25}I_3$ and $FAPb_{0.5}Sn_{0.25}Ge_{0.25}Br_3$ represent a shape curvature indicating a low effective mass of carriers (electron-hole). In contrast the bands of the $FAPb_{0.5}Sn_{0.25}Ge_{0.25}Cl_3$ structure are almost flattened, thus the effective mass is greater when compared to the two other compounds as represented in Table.II. 2. $FAPb_{0.5}Sn_{0.25}Ge_{0.25}I_3$, $FAPb_{0.5}Sn_{0.25}Ge_{0.25}Br_3$ structures represent an effective hole mass lower than $MAPbI_3$. The effective mass is inversely proportional to the mobility of carriers, therefore the mobility carriers of $FAPb_{0.5}Sn_{0.25}Ge_{0.25}I_3$ and $FAPb_{0.5}Sn_{0.25}Ge_{0.25}Br_3$ are large which will allow the electrons to easily cross the band gap. The CBM is mainly contributed by the p orbital of Pb in the $FAPb_{0.5}Sn_{0.25}Ge_{0.25}I_3$ structure, while it is dominated by the p orbital of the three elements Pb, Ge and Sn for the $FAPb_{0.5}Sn_{0.25}Ge_{0.25}Br_3$ and $FAPb_{0.5}Sn_{0.25}Ge_{0.25}Cl_3$. The VBM of the $FAPb_{0.5}Sn_{0.25}Ge_{0.25}X_3$ structures does not show any obvious difference, it is mainly derived from the p orbital of I, whereas the deep valence band is mainly contributed by the p orbital of N and the s orbital of Pb, Ge and Sn. The organic cation is positioned far from the VBM and the CBM. We notice that the co-doping by both Sn, and Ge elements shift the p states of halogen (I, Br, Cl) towards the lowest levels, which reduced the gap energies. We point out that this co-doping also adds additional energy levels, which allows more optical transitions.

a) $FAPbI_3$

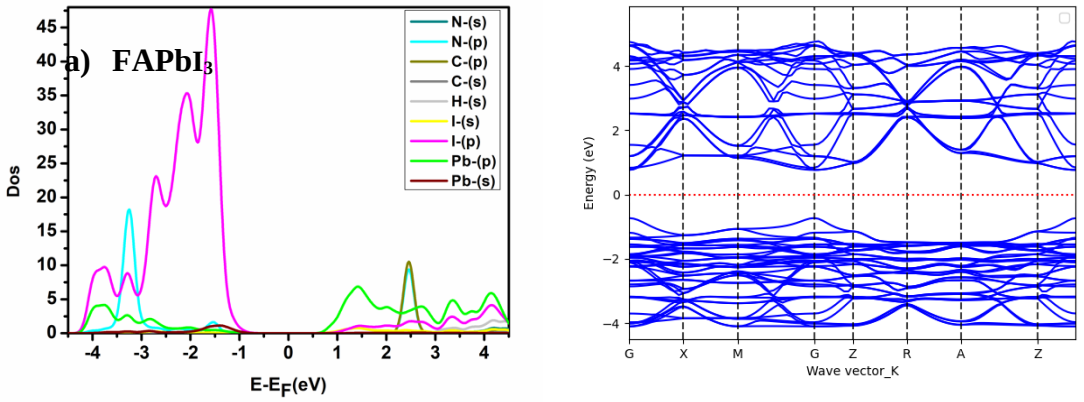

b) $FAPbBr_3$

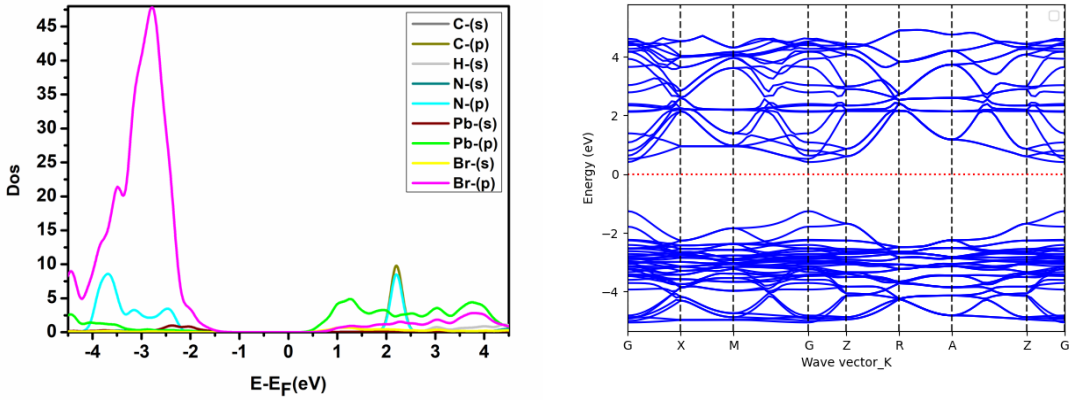

c) $FAPbCl_3$

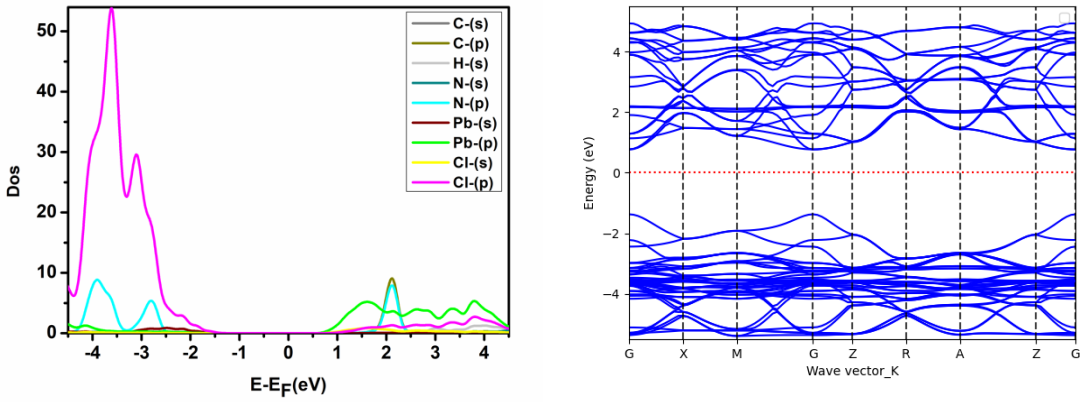

Fig.II. 2. Band structure and partial state density of $FAPbX_3$

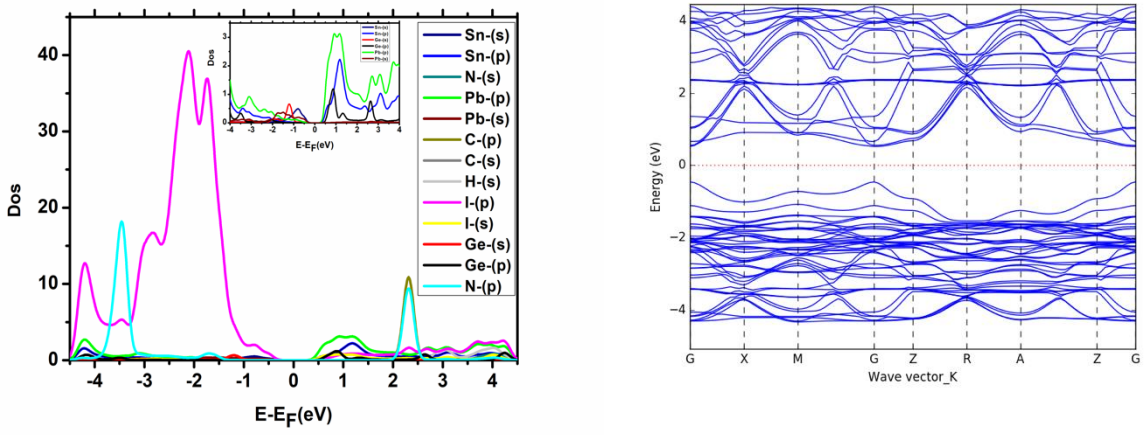

b) $FAPb_{0.5}Sn_{0.25}Ge_{0.25}Br_3$

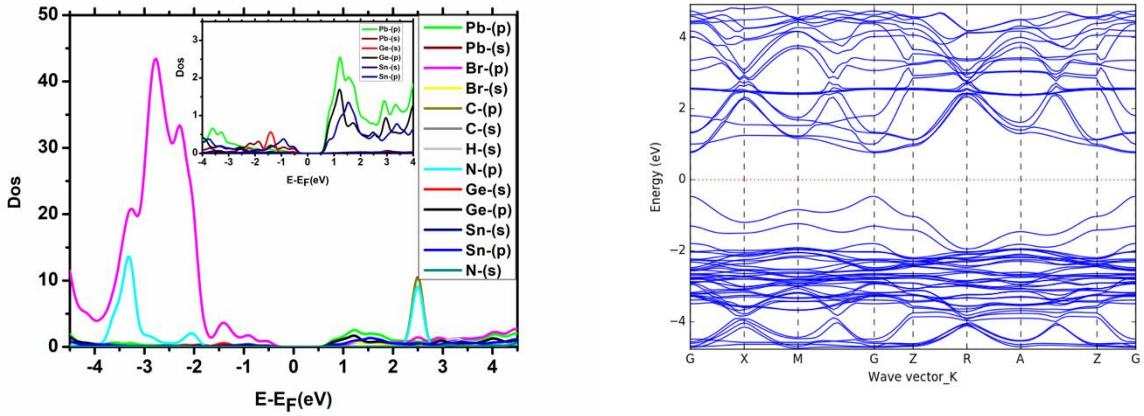

c) $FAPb_{0.5}Sn_{0.25}Ge_{0.25}Cl_3$

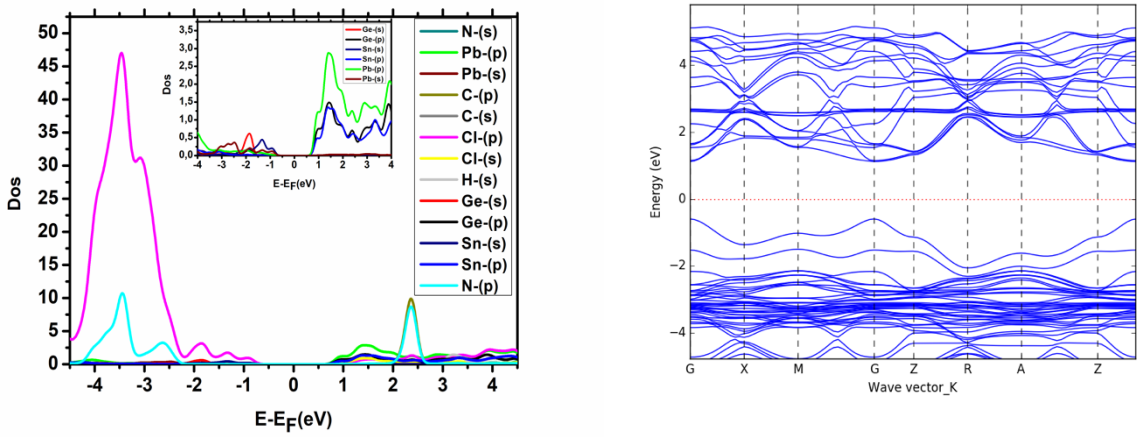

Fig.II. 3. Band structure and partial state density of $FAPb_{0.5}Sn_{0.25}Ge_{0.25}X_3$

Table.II. 2. Effective mass of $MAPbI_3$, $FAPb_{0.5}Sn_{0.25}Ge_{0.25}X_3$, and $FAPbX_3$ structures

Compounds	Eg (eV)	m_e	m_h
$MAPbI_3$	1.6	0.19	0.34
$FAPb_{0.5}Sn_{0.25}Ge_{0.25}I_3$	0.98	0.29	0.07
$FAPb_{0.5}Sn_{0.25}Ge_{0.25}Br_3$	1.22	0.24	0.08
$FAPb_{0.5}Sn_{0.25}Ge_{0.25}Cl_3$	1.7	1.13	0.36
$FAPbI_3$	1.5	0.44	0.19
$FAPbBr_3$	1.67	0.35	0.11
$FAPbCl_3$	2.14	0.72	0.19

III. Optical properties of $FAPbI_3$ and $FAPb_{0.5}Sn_{0.25}Ge_{0.25}X_3$ structures

The absorption coefficient determines how far into a material light of a particular wavelength can penetrate before it is absorbed. The absorption coefficient and the reflectivity of the three compounds were calculated from the dielectric constant $\varepsilon = \varepsilon_1 + i\,\varepsilon_2$, where ε_1 and ε_2 represent the real and imaginary part of the dielectric function, respectively.

As Shown in Fig.II. 4, $FAPbI_3$ has a larger absorption coefficient in visible spectra than $FAPbCl_3$ and $FAPbBr_3$, the co-doping with Sn and Ge improves the optical properties. As can be seen from the same Figure, the three $FAPb_{0.5}Sn_{0.25}Ge_{0.25}X_3$ compounds represent a high absorption coefficient in the visible range where the $FAPb_{0.5}Sn_{0.25}Ge_{0.25}I_3$ structure shows the highest absorption in this region, while the $FAPb_{0.5}Sn_{0.25}Ge_{0.25}Br_3$ and $FAPb_{0.5}Sn_{0.25}Ge_{0.25}Cl_3$ structures revealed the best absorption coefficient in the ultraviolet region. In physics and electrical engineering, the reflection coefficient describes how much of a wave is reflected by an impedance discontinuity in the medium transmission. According to Fig.II. 4b, all the investigated perovskite materials show a medium reflectivity in the IR-Visible-UV region of the spectra. This reflectivity suggests that the materials

have high absorptivity and/or transmissivity. Absorption coefficient and the reflectivity are the main parameters for the calculation of the short circuit current density.

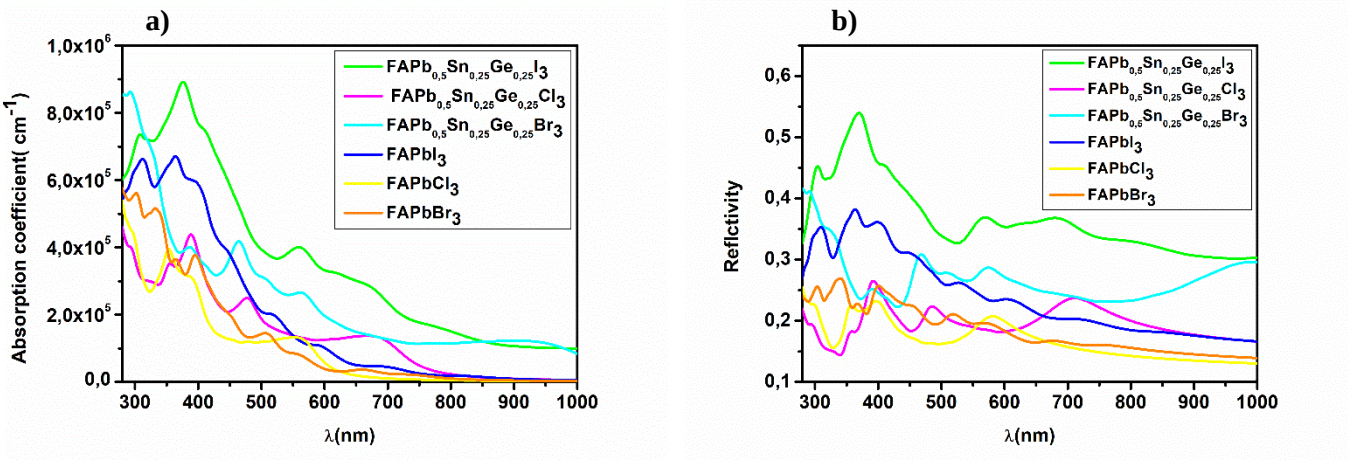

Fig.II. 4. Spectral (a) absorption coefficient and (b) reflectivity of $FAPb_{0.5}Sn_{0.25}Ge_{0.25}X_3$.

IV. Photovoltaic performances of $FAPbX_3$ and $FAPbSnGeX_3$

The power conversion efficiency of solar cells is related to the materials electronic and optical properties. In order to calculate the efficiency of these compounds we firstly start by the determination of the photovoltaic parameters: short-circuit current density and the open circuit voltage. The calculated power conversion efficiency (η) of the $MAPbI_3$ with an open circuit voltage (V_{oc}) of 1.1 V, a J_{sc} of 17.14 $mA.cm^{-2}$, and a fill factor (FF) of 60% gives a value of η =11% , this value matches the experimental results[265,266]. The current density characteristics of the $FAPbX_3$, and the $FAPb_{0.5}Sn_{0.25}Ge_{0.25}X_3$ compounds under AM1.5G solar irradiation are displayed in Fig.II. 5. The current density of all compounds is calculated at their gap energy value. $FAPb_{0.5}Sn_{0.25}Ge_{0.25}I_3$ structure represents the highest one with a value of 31.5 $mA.cm^{-2}$. The short-circuit current density shows a monotonically decrease from $FAPb_{0.5}Sn_{0.25}Ge_{0.25}I_3$ to $FAPbCl_3$ that represents the lowest Jsc. In particular, the calculated short-circuit current density for the $FAPbX_3$ shows lower values regarding those of $FAPb_{0.5}Sn_{0.25}Ge_{0.25}X_3$ compounds, revealing that the doping of lead has largely improved the J_{sc}. On the other hand, the halogens (I, Br, Cl) variation increase the band gap enticing the rise of the open circuit voltage. Yet, the open circuit voltage is expressed for perovskites solar cells as follows: $eV_{oc}= E_g-E_{loss}$, where E_{loss} = 0.7 or 0.5 eV represents a variable parameter loss in potential[267].

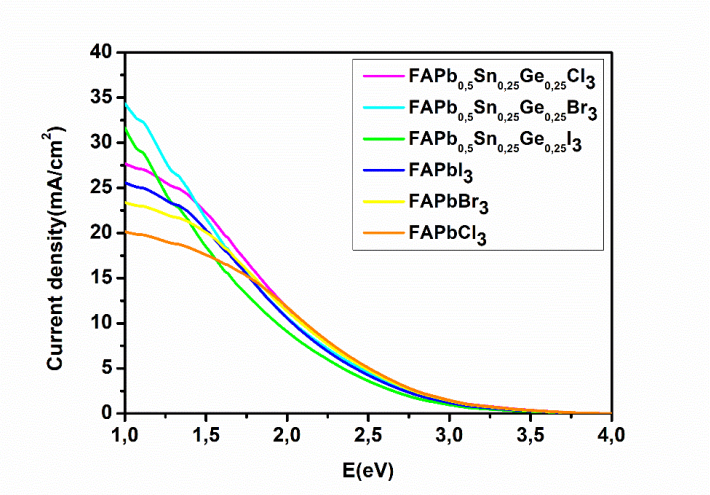

Fig.II. 5. Short-circuit current density of $FAPbX_3$, and $FAPb_{0.5}Sn_{0.25}Ge_{0.25}X_3$

The calculated open circuit voltage and the efficiency for both E_{loss} of 0.7 and 0.5 are represented in Table.II. 3. Although the high current density of $FAPb_{0.5}Sn_{0.25}Ge_{0.25}I_3$, this compound demonstrates the lowest efficiency among the three compounds due to its lower V_{oc} that can be improved by reducing the E_{loss}. Thus, as we can conclude from Fig.II. 5 and Table.II. 3, a high short circuit current density is not the only parameter that determines the power of producing a high efficiency. To summarize, Fig.II. 6 shows the variation of the efficiency as a function of the $FAPbX_3$, and $FAPb_{0.5}Sn_{0.25}Ge_{0.25}X_3$ bandgaps. $FAPb_{0.5}Sn_{0.25}Ge_{0.25}Cl_3$ reaches the high efficiency of 19.3% proving that this compound is a promising material for photovoltaic application with less toxicity.

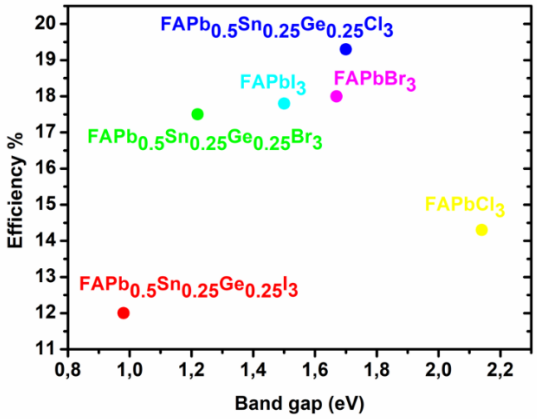

Fig.II. 6. Efficiency as a function of the $FAPbX_3$, and $FAPb_{0.5}Sn_{0.25}Ge_{0.25}X_3$ bandgaps

Table.II. 3. The calculated bandgap E_g, short-circuit current density J_{sc}, open circuit voltage V_{oc} and power conversion efficiency η of $FAPb_{0.5}Sn_{0.25}Ge_{0.25}X_3$ structures

Compounds	E_g	V_{oc}		J_{sc}	η %	
		E_{loss}(0.7 eV)	E_{loss}(0.5 eV)		E_{loss}(0.7 eV)	E_{loss}(0.5 eV)
$FAPb_{0.5}Sn_{0.25}Ge_{0.25}I_3$	0.98	0.28	0.48	31.5	6.17	12
$FAPb_{0.5}Sn_{0.25}Ge_{0.25}Br_3$	1.22	0.52	0.72	29	12	17.5
$FAPb_{0.5}Sn_{0.25}Ge_{0.25}Cl_3$	1.7	1	1.2	18	15.8	19.3
$FAPbI_3$	1.5	0.8	1	20.3	14	17.8
$FAPbBr_3$	1.67	0.97	1.17	17.3	14.6	18
$FAPbCl_3$	2.14	1.44	1.64	9.6	12.5	14.3

V. Conclusion

In summary, we discussed in this chapter the theoretical investigation regarding the efficiency of new less toxic $FAPb_{0.5}Sn_{0.25}Ge_{0.25}X_3$ structures, where the Plomb was half doped with tin and germanium. Cation used in these structures was the Formamidinium (FA) and the halogen (X) was swapped for iodine, bromine, and chlorine. Interestingly, we found that these new hybrid perovskite materials show a significant stability improvement as well as a high conversion efficiency making of them, promising materials for photovoltaic application.

Third Section-Conclusion

In summary, throughout this section we focused on the reduction of the toxicity and the stability-enhancement of hybrid perovskite $MAPbI_3$. At first, we demonstrated that doping by bromine enhances the structure stability against oxygen as the oxygen-bromine bond was found to be unfavorable. The variation of bromine site doping was also studied in order to enhance the perovskite's optical properties. Another doping by both tin and germanium was shown to be efficient in mitigating the perovskite-water interaction for a stable hybrid perovskite. Moreover, this doping showed also a reduction in the formation of vacancy at the perovskite surface. Finally, we have investigated the efficiency of this same combination of Plomb doped with tin and germanium. For this purpose, we studied the properties of the new less toxic $FAPb_{0.5}Sn_{0.25}Ge_{0.25}X_3$ structures, where FA is the Formamidinium cation and the halogen X was swapped for iodine, bromine, and chlorine. These systems are shown to demonstrate relatively high power conversion efficiency, which suggests that these materials represent a promising interest for the photovoltaic application with less toxicity.

SUMMARY AND OUTLOOK

Solar installation has seen growth over the past few years in different countries where China represents the leader accounting the globally number of installations. Most of these photovoltaic systems are based on silicon, whose efficiency hasn't made much progress in the recent years. Impressive evolution in efficiency has been developed by the revolution of hybrid perovskite materials that have opened a new way for more performant and efficient solar panels. Nevertheless, these hybrid perovskites are triggered and limited by the instability, degradation, and toxicity that they represent. For this purpose, the aim of this thesis is to study and describe hybrid perovskite materials as well as to suggest some approaches to mitigate the hybrid perovskite degradation processes and also to reduce their toxicity. Currently, in order to enhance the stability and the performance of these materials, an in-depth access and understanding of their fundamental atomic-scale properties is essential. The investigation of these properties has been established by density functional theory. Firstly, we have been interested in understanding the mechanism and environmental conditions (light, temperature, moisture, and oxygen) that lead to the destruction of hybrid perovskite and then, based on some new approaches, we looked for new materials that enhances the performances of the perovskite.

In our first study and in order to mitigate the oxygen hybrid perovskite interaction we have been interested on studying bromine doped hybrid perovskite. In this study, we have investigated the hybrid perovskite degradation mechanism in the presence of an interstitial oxygen atom and we demonstrate how bromine limits material degradation. In fact, oxygen in the $CH_3NH_3PbI_3$ structure has shown to form a strong bond with iodine (I), causing the displacement of the elements. Despite that, through the effect of bromine doping, we have shown that $CH_3NH_3PbI_2Br$-O limits the element displacement since the O-Br bonding is found to be unfavourable leading to an enhancement of the material stability. However, $CH_3NH_3PbI_2Br$ demonstrated the same dynamic stability properties as $CH_3NH_3PbI_3$, revealing that this dynamical instability does not affect the degradation of this material. Furthermore, studies have shown that bromine doping reduces the hybrid perovskite efficiency. In order to enhance the $CH_3NH_3PbI_2Br$ optical absorption, we performed an investigation of the bromine (Br) doping effect on different sites. Results showed that reducing the distortion of the hybrid perovskite structures, improving their electrical conductivity, and gaining a better and high absorption coefficient that covers almost the entire

visible spectrum can be reached by varying the doping site in the hybrid perovskite framework. Thus, by this study, we provide an understanding of the mechanism enhancement of hybrid perovskite stability by bromine doping keeping their performance.

In order to mitigate the perovskite water interaction for a stable hybrid perovskite solar cells, we have been interested in the study of the new less toxic $MAPb_{0.5}Sn_{0.25}Ge_{0.25}I_3$ thin film. We have established a detailed investigation based on Density Functional Theory (DFT) on pure and doped $MAPbI_3$ ($MAPbSnGeI_3$) under various distortions, namely Iodine vacancies and water adsorption. In the first stage, we focused in the study of the iodine formation energy in hybrid perovskite as it has been shown to trigger the degradation of these compounds. Various sites for Iodine vacancy V_I formation have been tested, and the V_I site at the $MAPbSnGeI_3$ surface has been found to exhibit the highest formation energy due to the strong atomic bonding added with the presence of germanium atom (Ge) and lead (Pb), which indicates weaker iodine dissolution from the surface leading to the stabilization of the system. The vacancies effect on the electronic properties of these materials has been investigated and showed the manifestation of a new deep trap state in the band structure. Furthermore, to provide the mechanism of water interaction with the $MAPbI_3$ and $MAPb_{0.5}Sn_{0.25}Ge_{0.25}I_3$ structures, we have tested all possible water adsorption sites onto these compounds. The adsorption on all tested sites has been found to be exothermic, particularly, the adsorption on H_{NH3} (Hydrogen atom of NH_3) presented the highest adsorption energy with the shortest and strongest O-H_{NH3} interatomic bonding followed by the adsorption on Pb. Interestingly, we demonstrated that the mitigation of the interaction between water molecules and $MAPb_{0.5}Sn_{0.25}Ge_{0.25}I_3$'s surface upon the half doping of Pb atom by Ge and Sn atoms improves the stability of the hybrid perovskite system. The mechanism of the $MAPb_{0.5}Sn_{0.25}Ge_{0.25}I_3$–Water interaction limitation has been explained by the water-surfaces charge transfer analysis. Thus, our results shed light on a new approach for solar cell development based on a stable less toxic perovskite.

The manifestation of toxicity in hybrid perovskite appears as the second major problem that stuck the commercialization of these materials. Toward reducing toxicity in the hybrid lead halide perovskite, we were interested in the investigation of a new hybrid less lead perovskite $FAPb_{0.5}Sn_{0.25}Ge_{0.25}X_3$ ((X = I, Br, Cl). For this purpose, the structural, electronic and optical properties investigation of these compounds has been established using the density functional

theory and compared with those of $FAPbX_3$ (X = I, Br, Cl) compounds. The results show that the compounds represent a suitable bandgap for photovoltaic cells. Additionally, we carried out the photovoltaic parameters (J_{sc}, V_{oc}, FF, P_{in}) in order to evaluate their power conversion efficiency. We demonstrated that the half doping of lead by both Ge, and Sn improves the stability of the system and enhances its performance for photovoltaic application. The adsorption coefficient and short-circuit current density have been also improved significantly with the doping effect, where the Jsc shows a monotonically increase from the $FAPbCl_3$ to $FAPb_{0.5}Sn_{0.25}Ge_{0.25}I_3$. We notice that, although the $FAPb_{0.5}Sn_{0.25}Ge_{0.25}I_3$ exhibits the high absorption coefficient in the visible range and the highest short-circuit current density, it presents the lowest power conversion efficiency due to its low open circuit voltage. Interestingly, our results demonstrate that the $FAPb_{0.5}Sn_{0.25}Ge_{0.25}Cl_3$ structure has relatively the highest power conversion efficiency demonstrating that this compound represents a promising interest for the photovoltaic application with less toxicity. This study can be a good reference for the development of a new absorber material in photovoltaic cells with less toxicity and more efficiency.

Commercialization of large-scale solar cell based hybrid perovskite has not yet been established due to the shortcoming of these materials. A lot of work, including our studies, is made and published every year in order to overcome these drawbacks. In this context, a patent has been established by our team that proposes a new hybrid material, nontoxic, and efficient for photovoltaic application. The properties demonstrated by this material show better properties than the lead-based hybrid perovskite. This material solves both the problem of toxicity and the stability of solar cells based on lead hybrid perovskites which could demonstrate a revolution in the photovoltaic field and could also be used in many other technological domains. Studies and development on this material are still ongoing. Following the results found in this thesis and the patent realized, an important challenge remains: working on the experimental part and development of this new material will hopefully allow us to make future Moroccan production solar cells prepared based on this material.

Indexes and bibliography

LIST OF FIGURES

1st section literature review

2nd section research Design of resaerch

3rd section Outcomes of research

LIST OF FIGURES

LIST OF TABLES

1st section literature review

3rd section Outcomes of research

BIBLIOGRAPHY

(1) *World Population Clock: 7.98 Billion People (2022) - Worldometer*. https://www.worldometers.info/world-population/.

(2) *The United States became the world's largest LNG exporter in the first half of 2022*. https://www.eia.gov/todayinenergy/detail.php?id=53159.

(3) *More than 60% of energy used for electricity generation is lost in conversion*. https://www.eia.gov/todayinenergy/detail.php?id=44436.

(4) *What is energy*. Eniscuola. https://www.eniscuola.net/en/argomento/energy-knowledge/energy-sources/what-is-energy/.

(5) Hurley, S. Solar Energy. *Explaining Science*, 2019.

(6) *Shining brightly*. MIT News | Massachusetts Institute of Technology. https://news.mit.edu/2011/energy-scale-part3-1026.

(7) Crabtree, G. W.; Lewis, N. S. Solar Energy Conversion. *Phys. Today* **2007**, *60* (3), 37–42. https://doi.org/10.1063/1.2718755.

(8) Xu, J.; Wang, R. Z.; Li, Y. A Review of Available Technologies for Seasonal Thermal Energy Storage. *Sol. Energy* **2014**, *103*, 610–638. https://doi.org/10.1016/j.solener.2013.06.006.

(9) Ritchie, H.; Roser, M.; Rosado, P. Energy. *Our World Data* **2020**.

(10) Zafar |, S. Solar Energy Developments in Morocco | EcoMENA, 2020.

(11) Min, H.; Lee, D. Y.; Kim, J.; Kim, G.; Lee, K. S.; Kim, J.; Paik, M. J.; Kim, Y. K.; Kim, K. S.; Kim, M. G.; Shin, T. J.; Il Seok, S. Perovskite Solar Cells with Atomically Coherent Interlayers on SnO2 Electrodes. *Nature* **2021**, *598* (7881), 444–450. https://doi.org/10.1038/s41586-021-03964-8.

(12) Chawla, R.; Singhal, P.; Garg, A. K. Photovoltaic Review of All Generations: Environmental Impact and Its Market Potential. *Trans. Electr. Electron. Mater.* **2020**, *21* (5), 456–476. https://doi.org/10.1007/s42341-020-00217-9.

(13) Uddin, A.; Upama, M.; Yi, H.; Duan, L. Encapsulation of Organic and Perovskite Solar Cells: A Review. *Coatings* **2019**, *9* (2), 65. https://doi.org/10.3390/coatings9020065.

(14) Lu, H.; Krishna, A.; Zakeeruddin, S. M.; Grätzel, M.; Hagfeldt, A. Compositional and Interface Engineering of Organic-Inorganic Lead Halide Perovskite Solar Cells. *iScience* **2020**, *23* (8), 101359. https://doi.org/10.1016/j.isci.2020.101359.

(15) Ghosh, D.; Perez, C. M.; Prezhdo, O.; Nie, W.; Tretiak, S.; Neukirch, A. J. Impact of Composition Engineering on Charge Carrier Cooling in Hybrid Perovskites: Computational Insights. *J. Mater. Chem. C* **2022**, *10* (25), 9563–9572. https://doi.org/10.1039/D2TC01413K.

(16) Einstein, A. Über Einen Die Erzeugung Und Verwandlung Des Lichtes Betreffenden Heuristischen Gesichtspunkt. *Ann. Phys.* **1905**, *322* (6), 132–148. https://doi.org/10.1002/andp.19053220607.

(17) Ohl, R. S. Light-Sensitive Electric Device. US2402662A, June 25, 1946.

(18) Sherman, D.; Marquez, J.; Ramirez, Y.; Urbina, M.; Meza, A.; Hodges, D. Monocrystalline Silicon Solar Cell Simulation With Reduced Absorber Thickness and Efficiency Exceeding 25%. In *2021 IEEE 48th Photovoltaic Specialists Conference (PVSC)*; 2021; pp 2640–2642. https://doi.org/10.1109/PVSC43889.2021.9518818.

(19) *Best Research-Cell Efficiency Chart*. https://www.nrel.gov/pv/cell-efficiency.html.
(20) *Handbook of Nanomaterials for Industrial Applications - 1st Edition*. https://www.elsevier.com/books/handbook-of-nanomaterials-for-industrial-applications/mustansar-hussain/978-0-12-813351-4.
(21) Smith, C.; Abram, R. A.; Burt, M. G. Theory of Auger Recombination in a Quantum Well Heterostructure. *Superlattices Microstruct.* **1985**, *1* (2), 119–123. https://doi.org/10.1016/0749-6036(85)90105-3.
(22) Shockley, W.; Read, W. T. Statistics of the Recombinations of Holes and Electrons. *Phys. Rev.* **1952**, *87* (5), 835–842. https://doi.org/10.1103/PhysRev.87.835.
(23) Hall, R. N. Electron-Hole Recombination in Germanium. *Phys. Rev.* **1952**, *87* (2), 387–387. https://doi.org/10.1103/PhysRev.87.387.
(24) Kim, E.; Bhattacharya, I. Material Selection Method for a Perovskite Solar Cell Design Based on the Genetic Algorithm. In *2020 47th IEEE Photovoltaic Specialists Conference (PVSC)*; 2020; pp 2631–2634. https://doi.org/10.1109/PVSC45281.2020.9300498.
(25) Tao, Y.; Rohatgi, A. *High-Efficiency Front Junction N-Type Crystalline Silicon Solar Cells*; IntechOpen, 2017. https://doi.org/10.5772/65023.
(26) *Standard Solar Spectra | PVEducation*. https://www.pveducation.org/pvcdrom/appendices/standard-solar-spectra.
(27) Printz, A. D.; Lipomi, D. J. Competition between Deformability and Charge Transport in Semiconducting Polymers for Flexible and Stretchable Electronics. *Appl. Phys. Rev.* **2016**, *3* (2), 021302. https://doi.org/10.1063/1.4947428.
(28) Hacke, P.; Meier, D. L. Analysis of Fill Factor Losses Using Current-Voltage Curves Obtained under Dark and Illuminated Conditions. In *Conference Record of the Twenty-Ninth IEEE Photovoltaic Specialists Conference, 2002.*; 2002; pp 462–464. https://doi.org/10.1109/PVSC.2002.1190559.
(29) Dhass, A. D.; Natarajan, E.; Ponnusamy, L. Influence of Shunt Resistance on the Performance of Solar Photovoltaic Cell. In *2012 International Conference on Emerging Trends in Electrical Engineering and Energy Management (ICETEEEM)*; 2012; pp 382–386. https://doi.org/10.1109/ICETEEEM.2012.6494522.
(30) Singh, P.; Ravindra, N. M. Analysis of Series and Shunt Resistance in Silicon Solar Cells Using Single and Double Exponential Models. *Emerg. Mater. Res.* **2012**, *1* (1), 33–38. https://doi.org/10.1680/emr.11.00008.
(31) Nakane, A.; Tampo, H.; Tamakoshi, M.; Fujimoto, S.; Kim, K. M.; Kim, S.; Shibata, H.; Niki, S.; Fujiwara, H. Quantitative Determination of Optical and Recombination Losses in Thin-Film Photovoltaic Devices Based on External Quantum Efficiency Analysis. *J. Appl. Phys.* **2016**, *120* (6), 064505. https://doi.org/10.1063/1.4960698.
(32) Tonui, P.; Oseni, S. O.; Sharma, G.; Yan, Q.; Tessema Mola, G. Perovskites Photovoltaic Solar Cells: An Overview of Current Status. *Renew. Sustain. Energy Rev.* **2018**, *91*, 1025–1044. https://doi.org/10.1016/j.rser.2018.04.069.
(33) Swanson, R. M. Approaching the 29% Limit Efficiency of Silicon Solar Cells. In *Conference Record of the Thirty-first IEEE Photovoltaic Specialists Conference, 2005.*; 2005; pp 889–894. https://doi.org/10.1109/PVSC.2005.1488274.
(34) Sherman, D.; Marquez, J.; Ramirez, Y.; Urbina, M.; Meza, A.; Hodges, D. Monocrystalline Silicon Solar Cell Simulation With Reduced Absorber Thickness and Efficiency Exceeding 25%. In *2021 IEEE 48th Photovoltaic Specialists Conference (PVSC)*; 2021; pp 2640–2642. https://doi.org/10.1109/PVSC43889.2021.9518818.

(35) Narayanan, S. Fifty Years Of Crystalline Silicon Solar Cells. In *Electro International, 1991*; 1991; pp 678–683. https://doi.org/10.1109/ELECTR.1991.718297.
(36) Chawla, R.; Singhal, P.; Garg, A. K. Photovoltaic Review of All Generations: Environmental Impact and Its Market Potential. *Trans. Electr. Electron. Mater.* **2020**, *21* (5), 456–476. https://doi.org/10.1007/s42341-020-00217-9.
(37) Jean, J.; Brown, P. R.; Jaffe, R. L.; Buonassisi, T.; Bulović, V. Pathways for Solar Photovoltaics. *Energy Environ. Sci.* **2015**, *8* (4), 1200–1219. https://doi.org/10.1039/C4EE04073B.
(38) Kowsar, A.; Farhad, S. F. U.; Rahaman, M.; Islam, M. S.; Imam, A. Y.; Debnath, S. C.; Sultana, M.; Hoque, M. A.; Sharmin, A.; Mahmood, Z. H. Progress in Major Thin-Film Solar Cells: Growth Technologies, Layer Materials and Efficiencies. *Int. J. Renew. Energy Res. IJRER* **2019**, *9* (2), 579–597.
(39) Kim, H. C.; Fthenakis, V.; Choi, J.-K.; Turney, D. E. Life Cycle Greenhouse Gas Emissions of Thin-Film Photovoltaic Electricity Generation. *J. Ind. Ecol.* **2012**, *16* (s1), S110–S121. https://doi.org/10.1111/j.1530-9290.2011.00423.x.
(40) Yan, J.; Saunders, B. R. Third-Generation Solar Cells: A Review and Comparison of Polymer:Fullerene, Hybrid Polymer and Perovskite Solar Cells. *RSC Adv.* **2014**, *4* (82), 43286–43314. https://doi.org/10.1039/C4RA07064J.
(41) Riede, M.; Spoltore, D.; Leo, K. Organic Solar Cells—The Path to Commercial Success. *Adv. Energy Mater.* **2021**, *11* (1), 2002653. https://doi.org/10.1002/aenm.202002653.
(42) Tang, C. W. Two-layer Organic Photovoltaic Cell. *Appl. Phys. Lett.* **1986**, *48* (2), 183–185. https://doi.org/10.1063/1.96937.
(43) Li, H.; Zhang, W. Perovskite Tandem Solar Cells: From Fundamentals to Commercial Deployment. *Chem. Rev.* **2020**, *120* (18), 9835–9950. https://doi.org/10.1021/acs.chemrev.9b00780.
(44) Green, M. A.; Dunlop, E. D.; Levi, D. H.; Hohl-Ebinger, J.; Yoshita, M.; Ho-Baillie, A. W. Y. Solar Cell Efficiency Tables (Version 54). *Prog. Photovolt. Res. Appl.* **2019**, *27* (7), 565–575. https://doi.org/10.1002/pip.3171.
(45) O'Regan, B.; Grätzel, M. A Low-Cost, High-Efficiency Solar Cell Based on Dye-Sensitized Colloidal TiO2 Films. *Nature* **1991**, *353* (6346), 737–740. https://doi.org/10.1038/353737a0.
(46) Kojima, A.; Teshima, K.; Shirai, Y.; Miyasaka, T. Organometal Halide Perovskites as Visible-Light Sensitizers for Photovoltaic Cells. *J. Am. Chem. Soc.* **2009**, *131* (17), 6050–6051. https://doi.org/10.1021/ja809598r.
(47) Im, J.-H.; Lee, C.-R.; Lee, J.-W.; Park, S.-W.; Park, N.-G. 6.5% Efficient Perovskite Quantum-Dot-Sensitized Solar Cell. *Nanoscale* **2011**, *3* (10), 4088–4093. https://doi.org/10.1039/C1NR10867K.
(48) Kim, H.-S.; Lee, C.-R.; Im, J.-H.; Lee, K.-B.; Moehl, T.; Marchioro, A.; Moon, S.-J.; Humphry-Baker, R.; Yum, J.-H.; Moser, J. E.; Grätzel, M.; Park, N.-G. Lead Iodide Perovskite Sensitized All-Solid-State Submicron Thin Film Mesoscopic Solar Cell with Efficiency Exceeding 9%. *Sci. Rep.* **2012**, *2* (1), 591. https://doi.org/10.1038/srep00591.
(49) Chawla, R.; Singal, P.; Garg, A. K. A Mamdani Fuzzy Logic System to Enhance Solar Cell Micro-Cracks Image Processing. *3D Res.* **2018**, *9* (3), 34. https://doi.org/10.1007/s13319-018-0186-7.

(50) *Photovoltaic Energy Factsheet | Center for Sustainable Systems*. Center for Sustainable Systems, University of Michigan. 2021. "Photovoltaic Energy Factsheet." Pub. No. CSS07-08.

(51) Serea, E. S. A.; Mohamed, S. A.; Shalan, A. E.; Rashad, M. M. 14 - Hybrid Perovskite Photovoltaic Devices: Architecture and Fabrication Methods Based on Solution-Processed Metal Oxide Transport Layers. In *Hybrid Perovskite Composite Materials*; Khan, I., Khan, A., Khan, M. M. A., Khan, S., Verpoort, F., Umar, A., Eds.; Woodhead Publishing Series in Composites Science and Engineering; Woodhead Publishing, 2021; pp 291–313. https://doi.org/10.1016/B978-0-12-819977-0.00014-7.

(52) Etgar, L.; Gao, P.; Xue, Z.; Peng, Q.; Chandiran, A. K.; Liu, B.; Nazeeruddin, Md. K.; Grätzel, M. Mesoscopic CH3NH3PbI3/TiO2 Heterojunction Solar Cells. *J. Am. Chem. Soc.* **2012**, *134* (42), 17396–17399. https://doi.org/10.1021/ja307789s.

(53) Lee, M. M.; Teuscher, J.; Miyasaka, T.; Murakami, T. N.; Snaith, H. J. Efficient Hybrid Solar Cells Based on Meso-Superstructured Organometal Halide Perovskites. *Science* **2012**, *338* (6107), 643–647. https://doi.org/10.1126/science.1228604.

(54) Motta, C.; El-Mellouhi, F.; Sanvito, S. Charge Carrier Mobility in Hybrid Halide Perovskites. *Sci. Rep.* **2015**, *5* (1), 12746. https://doi.org/10.1038/srep12746.

(55) Osman, B. A.; Abdolkader, T. M.; Ahmed, I. S. A Review of Perovskite Solar Cells. *Int. J. Mater. Technol. Innov.* **2021**, *1* (2), 48–66. https://doi.org/10.21608/ijmti.2021.78369.1032.

(56) Cheif, I. editor in. IJCRT2002249 International Journal of Creative Research Thoughts (IJCRT) Www.Ijcrt.Org. *IJCRT - Int. J. Creat. Res. Thoughts IJCRT*.

(57) Tress, W.; Marinova, N.; Moehl, T.; Zakeeruddin, S. M.; Nazeeruddin, M. K.; Grätzel, M. Understanding the Rate-Dependent J–V Hysteresis, Slow Time Component, and Aging in CH3NH3PbI3 Perovskite Solar Cells: The Role of a Compensated Electric Field. *Energy Environ. Sci.* **2015**, *8* (3), 995–1004. https://doi.org/10.1039/C4EE03664F.

(58) Heo, J. H.; Han, H. J.; Kim, D.; Ahn, T. K.; Im, S. H. Hysteresis-Less Inverted CH3NH3PbI3 Planar Perovskite Hybrid Solar Cells with 18.1% Power Conversion Efficiency. *Energy Environ. Sci.* **2015**, *8* (5), 1602–1608. https://doi.org/10.1039/C5EE00120J.

(59) Front Matter. In *Hybrid Perovskite Solar Cells*; John Wiley & Sons, Ltd, 2021; pp i–xix. https://doi.org/10.1002/9783527825851.fmatter.

(60) Danladi, E.; Dogo, D. S.; Michael, S. U.; Uloko, F. O.; Salawu, A. O. Recent Advances in Modeling of Perovskite Solar Cells Using SCAPS-1D: Effect of Absorber and ETM Thickness. *East Eur. J. Phys.* **2021**, No. 4, 5–17. https://doi.org/10.26565/2312-4334-2021-4-01.

(61) Hossain, A.; Bandyopadhyay, P.; Karmakar, A.; Ullah, A. K. M. A.; Manavalan, R. K.; Sakthipandi, K.; Alhokbany, N.; Alshehri, S. M.; Ahmed, J. The Hybrid Halide Perovskite: Synthesis Strategies, Fabrications, and Modern Applications. *Ceram. Int.* **2022**, *48* (6), 7325–7343. https://doi.org/10.1016/j.ceramint.2021.11.313.

(62) Im, J.-H.; Kim, H.-S.; Park, N.-G. Morphology-Photovoltaic Property Correlation in Perovskite Solar Cells: One-Step versus Two-Step Deposition of CH3NH3PbI3. *APL Mater.* **2014**, *2* (8), 081510. https://doi.org/10.1063/1.4891275.

(63) Saidaminov, M. I.; Abdelhady, A. L.; Murali, B.; Alarousu, E.; Burlakov, V. M.; Peng, W.; Dursun, I.; Wang, L.; He, Y.; Maculan, G.; Goriely, A.; Wu, T.; Mohammed, O. F.; Bakr, O. M. High-Quality Bulk Hybrid Perovskite Single Crystals within Minutes by Inverse

Temperature Crystallization. *Nat. Commun.* **2015**, *6* (1), 7586. https://doi.org/10.1038/ncomms8586.

(64) Chiang, C.-H.; Tseng, Z.-L.; Wu, C.-G. Planar Heterojunction Perovskite/PC71BM Solar Cells with Enhanced Open-Circuit Voltage via a (2/1)-Step Spin-Coating Process. *J. Mater. Chem. A* **2014**, *2* (38), 15897–15903. https://doi.org/10.1039/C4TA03674C.

(65) Raga, S. R.; Jiang, Y.; Ono, L. K.; Qi, Y. Application of Methylamine Gas in Fabricating Organic–Inorganic Hybrid Perovskite Solar Cells. *Energy Technol.* **2017**, *5* (10), 1750–1761. https://doi.org/10.1002/ente.201700423.

(66) Zhou, Z.; Wang, Z.; Zhou, Y.; Pang, S.; Wang, D.; Xu, H.; Liu, Z.; Padture, N. P.; Cui, G. Methylamine-Gas-Induced Defect-Healing Behavior of CH3NH3PbI3 Thin Films for Perovskite Solar Cells. *Angew. Chem. Int. Ed.* **2015**, *54* (33), 9705–9709. https://doi.org/10.1002/anie.201504379.

(67) Zhang, T.; Yang, M.; Benson, E. E.; Li, Z.; Lagemaat, J. van de; Luther, J. M.; Yan, Y.; Zhu, K.; Zhao, Y. A Facile Solvothermal Growth of Single Crystal Mixed Halide Perovskite CH3NH3Pb(Br1−xClx)3. *Chem. Commun.* **2015**, *51* (37), 7820–7823. https://doi.org/10.1039/C5CC01835H.

(68) Cao, X.; Hao, L.; Liu, Z.; Su, G.; He, X.; Zeng, Q.; Wei, J. All Green Solvent Engineering of Organic–Inorganic Hybrid Perovskite Layer for High-Performance Solar Cells. *Chem. Eng. J.* **2022**, *437*, 135458. https://doi.org/10.1016/j.cej.2022.135458.

(69) Zhou, H.; Chen, Q.; Yang, Y. Vapor-Assisted Solution Process for Perovskite Materials and Solar Cells. *MRS Bull.* **2015**, *40* (8), 667–673. https://doi.org/10.1557/mrs.2015.171.

(70) Li, M.-H.; Yeh, H.-H.; Chiang, Y.-H.; Jeng, U.-S.; Su, C.-J.; Shiu, H.-W.; Hsu, Y.-J.; Kosugi, N.; Ohigashi, T.; Chen, Y.-A.; Shen, P.-S.; Chen, P.; Guo, T.-F. Highly Efficient 2D/3D Hybrid Perovskite Solar Cells via Low-Pressure Vapor-Assisted Solution Process. *Adv. Mater.* **2018**, *30* (30), 1801401. https://doi.org/10.1002/adma.201801401.

(71) Snaith, H. J. Present Status and Future Prospects of Perovskite Photovoltaics. *Nat. Mater.* **2018**, *17* (5), 372–376. https://doi.org/10.1038/s41563-018-0071-z.

(72) Millán-Franco, M. A.; Pascoe-Sussoni, J. E.; Delesma, C.; Celaya, C. A.; Jaramillo-Quintero, O. A.; Muñiz, J.; Hu, H. Unveiling the Electronic Structure Nature of Twisted Hybrid Perovskites for Solar Cell Applications: A Combined Experimental and Theoretical Study. *Sol. Energy* **2021**, *227*, 151–161. https://doi.org/10.1016/j.solener.2021.08.072.

(73) Yin, Y.; Tian, W.; Luo, H.; Gao, Y.; Zhao, T.; Zhao, C.; Leng, J.; Sun, Q.; Tang, J.; Wang, P.; Li, Q.; Lü, X.; Bian, J.; Jin, S. Excellent Carrier Transport Property of Hybrid Perovskites Sustained under High Pressures. *ACS Energy Lett.* **2022**, *7* (1), 154–161. https://doi.org/10.1021/acsenergylett.1c02359.

(74) Mujahid, M.; Chen, C.; Hu, W.; Wang, Z.-K.; Duan, Y. Progress of High-Throughput and Low-Cost Flexible Perovskite Solar Cells. *Sol. RRL* **2020**, *4* (8), 1900556. https://doi.org/10.1002/solr.201900556.

(75) Roy, P.; Sinha, N. K.; Khare, A. 11 - Progress in Efficiency and Stability of Hybrid Perovskite Photovoltaic Devices in High Reactive Environments. In *Hybrid Perovskite Composite Materials*; Khan, I., Khan, A., Khan, M. M. A., Khan, S., Verpoort, F., Umar, A., Eds.; Woodhead Publishing Series in Composites Science and Engineering; Woodhead Publishing, 2021; pp 239–257. https://doi.org/10.1016/B978-0-12-819977-0.00011-1.

(76) Li, X.; Kepenekian, M.; Li, L.; Dong, H.; Stoumpos, C. C.; Seshadri, R.; Katan, C.; Guo, P.; Even, J.; Kanatzidis, M. G. Tolerance Factor for Stabilizing 3D Hybrid Halide

Perovskitoids Using Linear Diammonium Cations. *J. Am. Chem. Soc.* **2022**, *144* (9), 3902–3912. https://doi.org/10.1021/jacs.1c11803.

(77) Onoda-Yamamuro, N.; Matsuo, T.; Suga, H. Calorimetric and IR Spectroscopic Studies of Phase Transitions in Methylammonium Trihalogenoplumbates (II)†. *J. Phys. Chem. Solids* **1990**, *51* (12), 1383–1395. https://doi.org/10.1016/0022-3697(90)90021-7.

(78) Koh, T. M.; Wang, H.; Ng, Y. F.; Bruno, A.; Mhaisalkar, S.; Mathews, N. Halide Perovskite Solar Cells for Building Integrated Photovoltaics: Transforming Building Façades into Power Generators. *Adv. Mater. n/a* (n/a), 2104661. https://doi.org/10.1002/adma.202104661.

(79) Roy, A.; Ghosh, A.; Bhandari, S.; Sundaram, S.; Mallick, T. K. Perovskite Solar Cells for BIPV Application: A Review. *Buildings* **2020**, *10* (7), 129. https://doi.org/10.3390/buildings10070129.

(80) Yao, J.; Pan, Q.; Feng, Z.-J.; Xiong, Y.-A.; Sha, T.-T.; Ji, H.-R.; Gu, Z.-X.; You, Y.-M. Hybrid Organic–Inorganic Perovskite Ferroelectrics Bring Light to Semiconducting Applications: Bandgap Engineering as a Starting Point. *APL Mater.* **2021**, *9* (4), 040901. https://doi.org/10.1063/5.0039082.

(81) Yuan, L.; Wang, Z.; Duan, R.; Huang, P.; Zhang, K.; Chen, Q.; Allam, N. K.; Zhou, Y.; Song, B.; Li, Y. Semi-Transparent Perovskite Solar Cells: Unveiling the Trade-off between Transparency and Efficiency. *J. Mater. Chem. A* **2018**, *6* (40), 19696–19702. https://doi.org/10.1039/C8TA07318J.

(82) Thind, A. S.; Huang, X.; Sun, J.; Mishra, R. First-Principles Prediction of a Stable Hexagonal Phase of CH3NH3PbI3. *Chem. Mater.* **2017**, *29* (14), 6003–6011. https://doi.org/10.1021/acs.chemmater.7b01781.

(83) Li, H.-H.; Chen, Z.-R.; Cheng, L.-C.; Wang, Y.-J.; Feng, M.; Wang, M. Hybrid Polymeric Iodoplumbates Constructed from Morpholine and Its Derivatives: Structures and Properties. *Dalton Trans.* **2010**, *39* (45), 11000–11007. https://doi.org/10.1039/C0DT00622J.

(84) Lode, C.; Krautscheid, H. Iodostannate(II) mit kettenförmigen [SnI3]–-Anionen – der Übergang von fünffach zu sechsfach koordinierten SnII-Zentralatomen. *Z. Für Anorg. Allg. Chem.* **2001**, *627* (5), 841–846. https://doi.org/10.1002/1521-3749(200105)627:5<841::AID-ZAAC841>3.0.CO;2-Z.

(85) Stoumpos, C. C.; Malliakas, C. D.; Kanatzidis, M. G. Semiconducting Tin and Lead Iodide Perovskites with Organic Cations: Phase Transitions, High Mobilities, and Near-Infrared Photoluminescent Properties. *Inorg. Chem.* **2013**, *52* (15), 9019–9038. https://doi.org/10.1021/ic401215x.

(86) Francisco-López, A.; Charles, B.; Alonso, M. I.; Garriga, M.; Campoy-Quiles, M.; Weller, M. T.; Goñi, A. R. Phase Diagram of Methylammonium/Formamidinium Lead Iodide Perovskite Solid Solutions from Temperature-Dependent Photoluminescence and Raman Spectroscopies. *J. Phys. Chem. C* **2020**, *124* (6), 3448–3458. https://doi.org/10.1021/acs.jpcc.9b10185.

(87) Glazer, A. M. The Classification of Tilted Octahedra in Perovskites. *Acta Crystallogr. Sect. B* **1972**, *28* (11), 3384–3392. https://doi.org/10.1107/S0567740872007976.

(88) Lee, J.-H.; Bristowe, N. C.; Lee, J. H.; Lee, S.-H.; Bristowe, P. D.; Cheetham, A. K.; Jang, H. M. Resolving the Physical Origin of Octahedral Tilting in Halide Perovskites. *Chem. Mater.* **2016**, *28* (12), 4259–4266. https://doi.org/10.1021/acs.chemmater.6b00968.

(89) Klarbring, J. Low-Energy Paths for Octahedral Tilting in Inorganic Halide Perovskites. *Phys. Rev. B* **2019**, *99* (10), 104105. https://doi.org/10.1103/PhysRevB.99.104105.
(90) Targhi, F. F.; Jalili, Y. S.; Kanjouri, F. MAPbI3 and FAPbI3 Perovskites as Solar Cells: Case Study on Structural, Electrical and Optical Properties. *Results Phys.* **2018**, *10*, 616–627. https://doi.org/10.1016/j.rinp.2018.07.007.
(91) Weller, M. T.; Weber, O. J.; Frost, J. M.; Walsh, A. Cubic Perovskite Structure of Black Formamidinium Lead Iodide, α-[HC(NH2)2]PbI3, at 298 K. *J. Phys. Chem. Lett.* **2015**, *6* (16), 3209–3212. https://doi.org/10.1021/acs.jpclett.5b01432.
(92) Fabini, D. H.; Stoumpos, C. C.; Laurita, G.; Kaltzoglou, A.; Kontos, A. G.; Falaras, P.; Kanatzidis, M. G.; Seshadri, R. Reentrant Structural and Optical Properties and Large Positive Thermal Expansion in Perovskite Formamidinium Lead Iodide. *Angew. Chem. Int. Ed.* **2016**, *55* (49), 15392–15396. https://doi.org/10.1002/anie.201609538.
(93) Chen, T.; Chen, W.-L.; Foley, B. J.; Lee, J.; Ruff, J. P. C.; Ko, J. Y. P.; Brown, C. M.; Harriger, L. W.; Zhang, D.; Park, C.; Yoon, M.; Chang, Y.-M.; Choi, J. J.; Lee, S.-H. Origin of Long Lifetime of Band-Edge Charge Carriers in Organic-Inorganic Lead Iodide Perovskites. *Proc. Natl. Acad. Sci. U. S. A.* **2017**, *114* (29), 7519–7524. https://doi.org/10.1073/pnas.1704421114.
(94) Chen, T.; Foley, B. J.; Park, C.; Brown, C. M.; Harriger, L. W.; Lee, J.; Ruff, J.; Yoon, M.; Choi, J. J.; Lee, S.-H. Entropy-Driven Structural Transition and Kinetic Trapping in Formamidinium Lead Iodide Perovskite. *Sci. Adv.* *2* (10), e1601650. https://doi.org/10.1126/sciadv.1601650.
(95) Prathapani, S.; Choudhary, D.; Mallick, S.; Bhargava, P.; Yella, A. Experimental Evaluation of Room Temperature Crystallization and Phase Evolution of Hybrid Perovskite Materials. *CrystEngComm* **2017**, *19* (27), 3834–3843. https://doi.org/10.1039/C7CE00402H.
(96) Kong, W.; Ye, Z.; Qi, Z.; Zhang, B.; Wang, M.; Rahimi-Iman, A.; Wu, H. Characterization of an Abnormal Photoluminescence Behavior upon Crystal-Phase Transition of Perovskite CH3NH3PbI3. *Phys. Chem. Chem. Phys.* **2015**, *17* (25), 16405–16411. https://doi.org/10.1039/C5CP02605A.
(97) Bertoluzzi, L.; Sanchez, R. S.; Liu, L.; Lee, J.-W.; Mas-Marza, E.; Han, H.; Park, N.-G.; Mora-Sero, I.; Bisquert, J. Cooperative Kinetics of Depolarization in CH3NH3PbI3 Perovskite Solar Cells. *Energy Environ. Sci.* **2015**, *8* (3), 910–915. https://doi.org/10.1039/C4EE03171G.
(98) Sherkar, T. S.; Koster, L. J. A. Can Ferroelectric Polarization Explain the High Performance of Hybrid Halide Perovskite Solar Cells? *Phys. Chem. Chem. Phys.* **2015**, *18* (1), 331–338. https://doi.org/10.1039/C5CP07117H.
(99) Li, J.; Rinke, P. Atomic Structure of Metal-Halide Perovskites from First Principles: The Chicken-and-Egg Paradox of the Organic-Inorganic Interaction. *Phys. Rev. B* **2016**, *94* (4), 045201. https://doi.org/10.1103/PhysRevB.94.045201.
(100) Cordero, F.; Trequattrini, F.; Craciun, F.; Paoletti, A. M.; Pennesi, G.; Zanotti, G. Cation Reorientation and Octahedral Tilting in the Metal-Organic Perovskites MAPI and FAPI. *J. Alloys Compd.* **2021**, *867*, 158210. https://doi.org/10.1016/j.jallcom.2020.158210.
(101) Holekevi Chandrappa, M. L.; Zhu, Z.; Fenning, D. P.; Ong, S. P. Correlated Octahedral Rotation and Organic Cation Reorientation Assist Halide Ion Migration in Lead Halide Perovskites. *Chem. Mater.* **2021**, *33* (12), 4672–4678. https://doi.org/10.1021/acs.chemmater.1c01175.

(102) Maheshwari, S.; Fridriksson, M. B.; Seal, S.; Meyer, J.; Grozema, F. C. The Relation between Rotational Dynamics of the Organic Cation and Phase Transitions in Hybrid Halide Perovskites. *J. Phys. Chem. C* **2019**, *123* (23), 14652–14661. https://doi.org/10.1021/acs.jpcc.9b02736.
(103) Frost, J. M.; Butler, K. T.; Brivio, F.; Hendon, C. H.; van Schilfgaarde, M.; Walsh, A. Atomistic Origins of High-Performance in Hybrid Halide Perovskite Solar Cells. *Nano Lett.* **2014**, *14* (5), 2584–2590. https://doi.org/10.1021/nl500390f.
(104) Li, J.; Bouchard, M.; Reiss, P.; Aldakov, D.; Pouget, S.; Demadrille, R.; Aumaitre, C.; Frick, B.; Djurado, D.; Rossi, M.; Rinke, P. Activation Energy of Organic Cation Rotation in CH3NH3PbI3 and CD3NH3PbI3: Quasi-Elastic Neutron Scattering Measurements and First-Principles Analysis Including Nuclear Quantum Effects. *J. Phys. Chem. Lett.* **2018**, *9* (14), 3969–3977. https://doi.org/10.1021/acs.jpclett.8b01321.
(105) Carignano, M. A.; Saeed, Y.; Aravindh, S. A.; Roqan, I. S.; Even, J.; Katan, C. A Close Examination of the Structure and Dynamics of HC(NH2)2PbI3 by MD Simulations and Group Theory. *Phys. Chem. Chem. Phys.* **2016**, *18* (39), 27109–27118. https://doi.org/10.1039/C6CP02917E.
(106) Kanno, S.; Imamura, Y.; Hada, M. Theoretical Study on Rotational Controllability of Organic Cations in Organic–Inorganic Hybrid Perovskites: Hydrogen Bonds and Halogen Substitution. *J. Phys. Chem. C* **2017**, *121* (47), 26188–26195. https://doi.org/10.1021/acs.jpcc.7b07721.
(107) Karthick, S.; Ríos-Ramírez, J. J.; Velumani, S. 12 Possible Orientations of Organic Formamidinium Cation and Its Structural Analysis by First Principles Calculations Using Van Der Waals-Density Functional Theory. In *2018 15th International Conference on Electrical Engineering, Computing Science and Automatic Control (CCE)*; 2018; pp 1–5. https://doi.org/10.1109/ICEEE.2018.8533994.
(108) Kanno, S.; Imamura, Y.; Saeki, A.; Hada, M. Rotational Energy Barriers and Relaxation Times of the Organic Cation in Cubic Methylammonium Lead/Tin Halide Perovskites from First Principles. *J. Phys. Chem. C* **2017**, *121* (26), 14051–14059. https://doi.org/10.1021/acs.jpcc.7b04589.
(109) Deretzis, I.; Alberti, A.; Pellegrino, G.; Smecca, E.; Giannazzo, F.; Sakai, N.; Miyasaka, T.; La Magna, A. Atomistic Origins of CH3NH3PbI3 Degradation to PbI2 in Vacuum. *Appl. Phys. Lett.* **2015**, *106* (13), 131904. https://doi.org/10.1063/1.4916821.
(110) Mazumdar, S.; Zhao, Y.; Zhang, X. Stability of Perovskite Solar Cells: Degradation Mechanisms and Remedies. *Front. Electron.* **2021**, *2*.
(111) Lu, Y.-B.; Cong, W.-Y.; Guan, C.; Sun, H.; Xin, Y.; Wang, K.; Song, S. Light Enhanced Moisture Degradation of Perovskite Solar Cell Material CH3NH3PbI3. *J. Mater. Chem. A* **2019**, *7* (48), 27469–27474. https://doi.org/10.1039/C9TA10443G.
(112) Leguy, A. M. A.; Hu, Y.; Campoy-Quiles, M.; Alonso, M. I.; Weber, O. J.; Azarhoosh, P.; van Schilfgaarde, M.; Weller, M. T.; Bein, T.; Nelson, J.; Docampo, P.; Barnes, P. R. F. Reversible Hydration of CH3NH3PbI3 in Films, Single Crystals, and Solar Cells. *Chem. Mater.* **2015**, *27* (9), 3397–3407. https://doi.org/10.1021/acs.chemmater.5b00660.
(113) Zhu, Z.; Hadjiev, V. G.; Rong, Y.; Guo, R.; Cao, B.; Tang, Z.; Qin, F.; Li, Y.; Wang, Y.; Hao, F.; Venkatesan, S.; Li, W.; Baldelli, S.; Guloy, A. M.; Fang, H.; Hu, Y.; Yao, Y.; Wang, Z.; Bao, J. Interaction of Organic Cation with Water Molecule in Perovskite MAPbI3: From Dynamic Orientational Disorder to Hydrogen Bonding. *Chem. Mater.* **2016**, *28* (20), 7385–7393. https://doi.org/10.1021/acs.chemmater.6b02883.

(114) Wang, R. T.; Xu, A. F.; Chen, J. Y.; Yang, L. W.; Xu, G.; Jarvis, V.; Britten, J. F. Reversing Organic–Inorganic Hybrid Perovskite Degradation in Water via PH and Hydrogen Bonds. *J. Phys. Chem. Lett.* **2019**, *10* (22), 7245–7250. https://doi.org/10.1021/acs.jpclett.9b02972.
(115) Zheng, C.; Rubel, O. Unraveling the Water Degradation Mechanism of CH3NH3PbI3. *J. Phys. Chem. C* **2019**, *123* (32), 19385–19394. https://doi.org/10.1021/acs.jpcc.9b05516.
(116) Ahn, N.; Kwak, K.; Jang, M. S.; Yoon, H.; Lee, B. Y.; Lee, J.-K.; Pikhitsa, P. V.; Byun, J.; Choi, M. Trapped Charge-Driven Degradation of Perovskite Solar Cells. *Nat. Commun.* **2016**, *7* (1), 13422. https://doi.org/10.1038/ncomms13422.
(117) Llacer, J.; Moerman, D.; Douhéret, O.; Noirfalise, X.; Quarti, C.; Lazzaroni, R.; Théron, D.; Leclère, P. Nanoscale Studies at the Early Stage of Water-Induced Degradation of CH3NH3PbI3 Perovskite Films Used for Photovoltaic Applications. *ACS Appl. Nano Mater.* **2020**, *3* (8), 8268–8277. https://doi.org/10.1021/acsanm.0c01687.
(118) Chen, B.; Wang, S.; Song, Y.; Li, C.; Hao, F. A Critical Review on the Moisture Stability of Halide Perovskite Films and Solar Cells. *Chem. Eng. J.* **2022**, *430*, 132701. https://doi.org/10.1016/j.cej.2021.132701.
(119) Kwak, K.; Lim, E.; Ahn, N.; Heo, J.; Bang, K.; Kim, S. K.; Choi, M. An Atomistic Mechanism for the Degradation of Perovskite Solar Cells by Trapped Charge. *Nanoscale* **2019**, *11* (23), 11369–11378. https://doi.org/10.1039/C9NR02193K.
(120) Zhidkov, I. S.; Akbulatov, A. F.; Inasaridze, L. N.; Kukharenko, A. I.; Frolova, L. A.; Cholakh, S. O.; Chueh, C.-C.; Troshin, P. A.; Kurmaev, E. Z. Influence of Oxygen Ion Migration from Substrates on Photochemical Degradation of CH3NH3PbI3 Hybrid Perovskite. *Energies* **2021**, *14* (16), 5062. https://doi.org/10.3390/en14165062.
(121) Aristidou, N.; Eames, C.; Sanchez-Molina, I.; Bu, X.; Kosco, J.; Islam, M. S.; Haque, S. A. Fast Oxygen Diffusion and Iodide Defects Mediate Oxygen-Induced Degradation of Perovskite Solar Cells. *Nat. Commun.* **2017**, *8* (1), 15218. https://doi.org/10.1038/ncomms15218.
(122) Senocrate, A.; Acartürk, T.; Kim, G. Y.; Merkle, R.; Starke, U.; Grätzel, M.; Maier, J. Interaction of Oxygen with Halide Perovskites. *J. Mater. Chem. A* **2018**, *6* (23), 10847–10855. https://doi.org/10.1039/C8TA04537B.
(123) Aristidou, N.; Sanchez-Molina, I.; Chotchuangchutchaval, T.; Brown, M.; Martinez, L.; Rath, T.; Haque, S. A. The Role of Oxygen in the Degradation of Methylammonium Lead Trihalide Perovskite Photoactive Layers. *Angew. Chem. Int. Ed Engl.* **2015**, *54* (28), 8208–8212. https://doi.org/10.1002/anie.201503153.
(124) Ouyang, Y.; Shi, L.; Li, Q.; Wang, J. Role of Water and Defects in Photo-Oxidative Degradation of Methylammonium Lead Iodide Perovskite. *Small Methods* **2019**, *3* (7), 1900154. https://doi.org/10.1002/smtd.201900154.
(125) Wang, S.; Jiang, Y.; Juarez-Perez, E. J.; Ono, L. K.; Qi, Y. Accelerated Degradation of Methylammonium Lead Iodide Perovskites Induced by Exposure to Iodine Vapour. *Nat. Energy* **2016**, *2* (1), 1–8. https://doi.org/10.1038/nenergy.2016.195.
(126) Zhang, L.; Sit, P. H.-L. Ab Initio Study of the Role of Oxygen and Excess Electrons in the Degradation of CH3NH3PbI3. *J. Mater. Chem. A* **2017**, *5* (19), 9042–9049. https://doi.org/10.1039/C7TA01091E.
(127) Ouyang, Y.; Li, Y.; Zhu, P.; Li, Q.; Gao, Y.; Tong, J.; Shi, L.; Zhou, Q.; Ling, C.; Chen, Q.; Deng, Z.; Tan, H.; Deng, W.; Wang, J. Photo-Oxidative Degradation of

Methylammonium Lead Iodide Perovskite: Mechanism and Protection. *J. Mater. Chem. A* **2019**, *7* (5), 2275–2282. https://doi.org/10.1039/C8TA12193A.

(128) Zhidkov, I. S.; Poteryaev, A. I.; Kukharenko, A. I.; Finkelstein, L. D.; Cholakh, S. O.; Akbulatov, A. F.; Troshin, P. A.; Chueh, C.-C.; Kurmaev, E. Z. XPS Evidence of Degradation Mechanism in CH3NH3PbI3 Hybrid Perovskite. *J. Phys. Condens. Matter* **2019**, *32* (9), 095501. https://doi.org/10.1088/1361-648X/ab576f.

(129) Juarez-Perez, E. J.; Hawash, Z.; Raga, S. R.; Ono, L. K.; Qi, Y. Thermal Degradation of CH3NH3PbI3 Perovskite into NH3 and CH3I Gases Observed by Coupled Thermogravimetry–Mass Spectrometry Analysis. *Energy Environ. Sci.* **2016**, *9* (11), 3406–3410. https://doi.org/10.1039/C6EE02016J.

(130) Brunetti, B.; Cavallo, C.; Ciccioli, A.; Gigli, G.; Latini, A. On the Thermal and Thermodynamic (In)Stability of Methylammonium Lead Halide Perovskites. *Sci. Rep.* **2016**, *6* (1), 31896. https://doi.org/10.1038/srep31896.

(131) Latini, A.; Gigli, G.; Ciccioli, A. A Study on the Nature of the Thermal Decomposition of Methylammonium Lead Iodide Perovskite, CH3NH3PbI3: An Attempt to Rationalise Contradictory Experimental Results. *Sustain. Energy Fuels* **2017**, *1* (6), 1351–1357. https://doi.org/10.1039/C7SE00114B.

(132) Liu, F.; Dong, Q.; Wong, M. K.; Djurišić, A. B.; Ng, A.; Ren, Z.; Shen, Q.; Surya, C.; Chan, W. K.; Wang, J.; Ng, A. M. C.; Liao, C.; Li, H.; Shih, K.; Wei, C.; Su, H.; Dai, J. Is Excess PbI2 Beneficial for Perovskite Solar Cell Performance? *Adv. Energy Mater.* **2016**, *6* (7), 1502206. https://doi.org/10.1002/aenm.201502206.

(133) Dawood, R. I.; Forty, A. J.; Tubbs, M. R.; Frank, F. C. The Photodecomposition of Lead Iodide. *Proc. R. Soc. Lond. Ser. Math. Phys. Sci.* **1965**, *284* (1397), 272–288. https://doi.org/10.1098/rspa.1965.0063.

(134) J. Juarez-Perez, E.; K. Ono, L.; Maeda, M.; Jiang, Y.; Hawash, Z.; Qi, Y. Photodecomposition and Thermal Decomposition in Methylammonium Halide Lead Perovskites and Inferred Design Principles to Increase Photovoltaic Device Stability. *J. Mater. Chem. A* **2018**, *6* (20), 9604–9612. https://doi.org/10.1039/C8TA03501F.

(135) Christians, J. A.; Miranda Herrera, P. A.; Kamat, P. V. Transformation of the Excited State and Photovoltaic Efficiency of CH3NH3PbI3 Perovskite upon Controlled Exposure to Humidified Air. *J. Am. Chem. Soc.* **2015**, *137* (4), 1530–1538. https://doi.org/10.1021/ja511132a.

(136) Schwenzer, J. A.; Hellmann, T.; Nejand, B. A.; Hu, H.; Abzieher, T.; Schackmar, F.; Hossain, I. M.; Fassl, P.; Mayer, T.; Jaegermann, W.; Lemmer, U.; Paetzold, U. W. Thermal Stability and Cation Composition of Hybrid Organic–Inorganic Perovskites. *ACS Appl. Mater. Interfaces* **2021**, *13* (13), 15292–15304. https://doi.org/10.1021/acsami.1c01547.

(137) Quitsch, W.-A.; deQuilettes, D. W.; Pfingsten, O.; Schmitz, A.; Ognjanovic, S.; Jariwala, S.; Koch, S.; Winterer, M.; Ginger, D. S.; Bacher, G. The Role of Excitation Energy in Photobrightening and Photodegradation of Halide Perovskite Thin Films. *J. Phys. Chem. Lett.* **2018**, *9* (8), 2062–2069. https://doi.org/10.1021/acs.jpclett.8b00212.

(138) Boldyreva, A. G.; Akbulatov, A. F.; Elnaggar, M.; Luchkin, S. Y.; Danilov, A. V.; Zhidkov, I. S.; Yamilova, O. R.; Fedotov, Y. S.; Bredikhin, S. I.; Kurmaev, E. Z.; Stevenson, K. J.; Troshin, P. A. Impact of Charge Transport Layers on the Photochemical Stability of MAPbI3 in Thin Films and Perovskite Solar Cells. *Sustain. Energy Fuels* **2019**, *3* (10), 2705–2716. https://doi.org/10.1039/C9SE00493A.

(139) Yang, Y.; Zhang, Y.; Bai, L.; Malouangou, D. M.; Matondo, J. T.; Pan, J.; Dai, S.; Cai, M.; Liu, X.; Guli, M. Research Progress of Atomic Layer Deposition Technology to Improve the Long-Term Stability of Perovskite Solar Cells. *J. Mater. Chem. C* **2022**, *10* (3), 819–839. https://doi.org/10.1039/D1TC05035D.
(140) Gabriel Tomulescu, A.; Nicoleta Leonat, L.; Neațu, F.; Stancu, V.; Toma, V.; Derbali, S.; Neațu, Ștefan; Mihai Rostas, A.; Beșleagă, C.; Pătru, R.; Pintilie, I.; Florea, M. Enhancing Stability of Hybrid Perovskite Solar Cells by Imidazolium Incorporation. *Sol. Energy Mater. Sol. Cells* **2021**, *227*, 111096. https://doi.org/10.1016/j.solmat.2021.111096.
(141) Jiang, Q.; Rebollar, D.; Gong, J.; Piacentino, E. L.; Zheng, C.; Xu, T. Pseudohalide-Induced Moisture Tolerance in Perovskite CH3 NH3 Pb(SCN)2 I Thin Films. *Angew. Chem. Int. Ed Engl.* **2015**, *54* (26), 7617–7620. https://doi.org/10.1002/anie.201503038.
(142) Cai, Y.; Cui, J.; Chen, M.; Zhang, M.; Han, Y.; Qian, F.; Zhao, H.; Yang, S.; Yang, Z.; Bian, H.; Wang, T.; Guo, K.; Cai, M.; Dai, S.; Liu, Z.; Liu, S. (Frank). Multifunctional Enhancement for Highly Stable and Efficient Perovskite Solar Cells. *Adv. Funct. Mater.* **2021**, *31* (7), 2005776. https://doi.org/10.1002/adfm.202005776.
(143) Fan, Y.; Wang, X.; Miao, Y.; Zhao, Y. The Chemical Design in High-Performance Lead Halide Perovskite: Additive vs Dopant? *J. Phys. Chem. Lett.* **2021**, *12* (48), 11636–11644. https://doi.org/10.1021/acs.jpclett.1c03399.
(144) Aranda, C. A.; Caliò, L.; Salado, M. Toward Commercialization of Stable Devices: An Overview on Encapsulation of Hybrid Organic-Inorganic Perovskite Solar Cells. *Crystals* **2021**, *11* (5), 519. https://doi.org/10.3390/cryst11050519.
(145) Hosseinian Ahangharnejhad, R.; Song, Z.; Mariam, T.; Gardner, J. J.; Liyanage, G. K.; Almutawah, Z. S.; Anwar, B. M. M.; Junda, M.; Podraza, N. J.; Phillips, A. B.; Yan, Y.; Heben, M. J. Protecting Perovskite Solar Cells against Moisture-Induced Degradation with Sputtered Inorganic Barrier Layers. *ACS Appl. Energy Mater.* **2021**, *4* (8), 7571–7578. https://doi.org/10.1021/acsaem.1c00816.
(146) Boyd, C. C.; Cheacharoen, R.; Bush, K. A.; Prasanna, R.; Leijtens, T.; McGehee, M. D. Barrier Design to Prevent Metal-Induced Degradation and Improve Thermal Stability in Perovskite Solar Cells. *ACS Energy Lett.* **2018**, *3* (7), 1772–1778. https://doi.org/10.1021/acsenergylett.8b00926.
(147) *Reviews of Environmental Contamination and Toxicology Volume 233*.
(148) Hutter, E. M.; Sangster, R.; Testerink, C.; Ehrler, B.; Gommers, C. M. M. Metal Halide Perovskite Toxicity Effects on Arabidopsis Thaliana Plants Are Caused by Iodide Ions. *iScience* **2022**, *25* (1). https://doi.org/10.1016/j.isci.2021.103583.
(149) Horváth, E.; Kollár, M.; Andričević, P.; Rossi, L.; Mettan, X.; Forró, L. Fighting Health Hazards in Lead Halide Perovskite Optoelectronic Devices with Transparent Phosphate Salts. *ACS Appl. Mater. Interfaces* **2021**, *13* (29), 33995–34002. https://doi.org/10.1021/acsami.0c21137.
(150) Ke, W.; Kanatzidis, M. G. Prospects for Low-Toxicity Lead-Free Perovskite Solar Cells. *Nat. Commun.* **2019**, *10* (1), 965. https://doi.org/10.1038/s41467-019-08918-3.
(151) Shalan, A. E.; Kazim, S.; Ahmad, S. Lead-Free Perovskites: Metals Substitution towards Environmentally Benign Solar Cell Fabrication. *ChemSusChem* **2019**, *12* (18), 4116–4139. https://doi.org/10.1002/cssc.201901296.
(152) Li, M.; Zuo, W.-W.; Yang, Y.-G.; Aldamasy, M. H.; Wang, Q.; Cruz, S. H. T.; Feng, S.-L.; Saliba, M.; Wang, Z.-K.; Abate, A. Tin Halide Perovskite Films Made of Highly

Oriented 2D Crystals Enable More Efficient and Stable Lead-Free Perovskite Solar Cells. *ACS Energy Lett.* **2020**, *5* (6), 1923–1929. https://doi.org/10.1021/acsenergylett.0c00782.
(153) Wang, R.; Wang, J.; Tan, S.; Duan, Y.; Wang, Z.-K.; Yang, Y. Opportunities and Challenges of Lead-Free Perovskite Optoelectronic Devices. *Trends Chem.* **2019**, *1* (4), 368–379. https://doi.org/10.1016/j.trechm.2019.04.004.
(154) Löwdin, P.-O. Mathematics in Chemistry and in Mathematical Chemistry. *J. Math. Chem.* **1990**, *4* (1), 3–14. https://doi.org/10.1007/BF01170000.
(155) Löwdin, P.-O. Connection between semi-empirical and ab initio methods in the quantum theory of molecular electronic spectra. *Int. J. Quantum Chem.* **1999**, *72* (4), 379–391. https://doi.org/10.1002/(SICI)1097-461X(1999)72:4<379::AID-QUA22>3.0.CO;2-U.
(156) Kurth, S.; Marques, M. A. L.; Gross, E. K. U. Density-Functional Theory. In *Encyclopedia of Condensed Matter Physics*; Bassani, F., Liedl, G. L., Wyder, P., Eds.; Elsevier: Oxford, 2005; pp 395–402. https://doi.org/10.1016/B0-12-369401-9/00445-9.
(157) Head-Gordon, M.; Artacho, E. Chemistry on the Computer. *Phys. Today* **2008**, *61* (4), 58–63. https://doi.org/10.1063/1.2911179.
(158) Shirley, J. H. Solution of the Schr\"odinger Equation with a Hamiltonian Periodic in Time. *Phys. Rev.* **1965**, *138* (4B), B979–B987. https://doi.org/10.1103/PhysRev.138.B979.
(159) Born, M.; Oppenheimer, R. Zur Quantentheorie Der Molekeln. *Ann. Phys.* **1927**, *389* (20), 457–484. https://doi.org/10.1002/andp.19273892002.
(160) Hohenberg, P.; Kohn, W. Inhomogeneous Electron Gas. *Phys. Rev.* **1964**, *136* (3B), B864–B871. https://doi.org/10.1103/PhysRev.136.B864.
(161) Kohn, W.; Sham, L. J. Self-Consistent Equations Including Exchange and Correlation Effects. *Phys. Rev.* **1965**, *140* (4A), A1133–A1138. https://doi.org/10.1103/PhysRev.140.A1133.
(162) Parr, R. G.; Weitao, Y. *Density-Functional Theory of Atoms and Molecules*; International Series of Monographs on Chemistry; Oxford University Press: New York, 1995. https://doi.org/10.1093/oso/9780195092769.001.0001.
(163) Ceperley, D. M.; Alder, B. J. Ground State of the Electron Gas by a Stochastic Method. *Phys. Rev. Lett.* **1980**, *45* (7), 566–569. https://doi.org/10.1103/PhysRevLett.45.566.
(164) Perdew, null; Chevary, null; Vosko, null; Jackson, null; Pederson, null; Singh, null; Fiolhais, null. Atoms, Molecules, Solids, and Surfaces: Applications of the Generalized Gradient Approximation for Exchange and Correlation. *Phys. Rev. B Condens. Matter* **1992**, *46* (11), 6671–6687. https://doi.org/10.1103/physrevb.46.6671.
(165) Perdew, J. P.; Burke, K.; Ernzerhof, M. Generalized Gradient Approximation Made Simple. *Phys. Rev. Lett.* **1996**, *77* (18), 3865–3868. https://doi.org/10.1103/PhysRevLett.77.3865.
(166) Perdew, J. P.; Ruzsinszky, A.; Csonka, G. I.; Vydrov, O. A.; Scuseria, G. E.; Constantin, L. A.; Zhou, X.; Burke, K. Restoring the Density-Gradient Expansion for Exchange in Solids and Surfaces. *Phys. Rev. Lett.* **2008**, *100* (13), 136406. https://doi.org/10.1103/PhysRevLett.100.136406.
(167) Park, J.; Yu, B. D.; Hong, S. Van Der Waals Density Functional Theory Study for Bulk Solids with BCC, FCC, and Diamond Structures. *Curr. Appl. Phys.* **2015**, *15* (8), 885–891. https://doi.org/10.1016/j.cap.2015.03.028.
(168) Dion, M.; Rydberg, H.; Schröder, E.; Langreth, D. C.; Lundqvist, B. I. Van Der Waals Density Functional for General Geometries. *Phys. Rev. Lett.* **2004**, *92* (24), 246401. https://doi.org/10.1103/PhysRevLett.92.246401.

(169) Görling, A. Kohn-Sham Potentials and Wave Functions from Electron Densities. *Phys. Rev. A* **1992**, *46* (7), 3753–3757. https://doi.org/10.1103/PhysRevA.46.3753.
(170) Wannier, G. H. Wave Functions and Effective Hamiltonian for Bloch Electrons in an Electric Field. *Phys. Rev.* **1960**, *117* (2), 432–439. https://doi.org/10.1103/PhysRev.117.432.
(171) Kittel, C.; McEuen, P. *Introduction to Solid State Physics*; 2018.
(172) Ashcroft, N. W.; Mermin, N. D. *Solid State Physics*; Holt, Rinehart and Winston: New York, 1976.
(173) Lin, J. S.; Qteish, A.; Payne, M. C.; Heine, V. Optimized and Transferable Nonlocal Separable Ab Initio Pseudopotentials. *Phys. Rev. B* **1993**, *47* (8), 4174–4180. https://doi.org/10.1103/PhysRevB.47.4174.
(174) Giannozzi, P.; Baroni, S.; Bonini, N.; Calandra, M.; Car, R.; Cavazzoni, C.; Ceresoli, D.; Chiarotti, G. L.; Cococcioni, M.; Dabo, I.; Corso, A. D.; Gironcoli, S. de; Fabris, S.; Fratesi, G.; Gebauer, R.; Gerstmann, U.; Gougoussis, C.; Kokalj, A.; Lazzeri, M.; Martin-Samos, L.; Marzari, N.; Mauri, F.; Mazzarello, R.; Paolini, S.; Pasquarello, A.; Paulatto, L.; Sbraccia, C.; Scandolo, S.; Sclauzero, G.; Seitsonen, A. P.; Smogunov, A.; Umari, P.; Wentzcovitch, R. M. QUANTUM ESPRESSO: A Modular and Open-Source Software Project for Quantum Simulations of Materials. *J. Phys. Condens. Matter* **2009**, *21* (39), 395502. https://doi.org/10.1088/0953-8984/21/39/395502.
(175) Tao, S. SOLID STATE PHYSICS PART I Transport Properties of Solids.
(176) Sachs, M. *Solid State Theory*, 1st Edition.; McGraw-Hill, 1963.
(177) van Setten, M. J.; Er, S.; Brocks, G.; de Groot, R. A.; de Wijs, G. A. First-Principles Study of the Optical Properties of MgxTi1−xH2. *Phys. Rev. B* **2009**, *79* (12), 125117. https://doi.org/10.1103/PhysRevB.79.125117.
(178) Marini, A.; Hogan, C.; Grüning, M.; Varsano, D. Yambo: An Ab Initio Tool for Excited State Calculations. *Comput. Phys. Commun.* **2009**, *180* (8), 1392–1403. https://doi.org/10.1016/j.cpc.2009.02.003.
(179) Gajdoš, M.; Hummer, K.; Kresse, G.; Furthmüller, J.; Bechstedt, F. Linear Optical Properties in the Projector-Augmented Wave Methodology. *Phys. Rev. B* **2006**, *73* (4), 045112. https://doi.org/10.1103/PhysRevB.73.045112.
(180) Togo, A.; Tanaka, I. First Principles Phonon Calculations in Materials Science. *Scr. Mater.* **2015**, *108*, 1–5. https://doi.org/10.1016/j.scriptamat.2015.07.021.
(181) Jena, A. K.; Kulkarni, A.; Miyasaka, T. Halide Perovskite Photovoltaics: Background, Status, and Future Prospects. *Chem. Rev.* **2019**, *119* (5), 3036–3103. https://doi.org/10.1021/acs.chemrev.8b00539.
(182) Stranks, S. D.; Eperon, G. E.; Grancini, G.; Menelaou, C.; Alcocer, M. J. P.; Leijtens, T.; Herz, L. M.; Petrozza, A.; Snaith, H. J. Electron-Hole Diffusion Lengths Exceeding 1 Micrometer in an Organometal Trihalide Perovskite Absorber. *Science* **2013**, *342* (6156), 341–344. https://doi.org/10.1126/science.1243982.
(183) De Wolf, S.; Holovsky, J.; Moon, S.-J.; Löper, P.; Niesen, B.; Ledinsky, M.; Haug, F.-J.; Yum, J.-H.; Ballif, C. Organometallic Halide Perovskites: Sharp Optical Absorption Edge and Its Relation to Photovoltaic Performance. *J. Phys. Chem. Lett.* **2014**, *5* (6), 1035–1039. https://doi.org/10.1021/jz500279b.
(184) Eperon, G. E.; Stranks, S. D.; Menelaou, C.; Johnston, M. B.; Herz, L. M.; Snaith, H. J. Formamidinium Lead Trihalide: A Broadly Tunable Perovskite for Efficient Planar

Heterojunction Solar Cells. *Energy Environ. Sci.* **2014**, *7* (3), 982–988. https://doi.org/10.1039/C3EE43822H.

(185) Kumavat, S. R.; Sonvane, Y.; Singh, D.; Gupta, S. K. Two-Dimensional CH3NH3PbI3 with High Efficiency and Superior Carrier Mobility: A Theoretical Study. *J. Phys. Chem. C* **2019**, *123* (9), 5231–5239. https://doi.org/10.1021/acs.jpcc.8b11427.

(186) Gu, Y.-F.; Du, H.-J.; Li, N.-N.; Yang, L.; Zhou, C.-Y. Effect of Carrier Mobility on Performance of Perovskite Solar Cells. *Chin. Phys. B* **2019**, *28* (4), 048802. https://doi.org/10.1088/1674-1056/28/4/048802.

(187) Phillips, L. J.; Rashed, A. M.; Treharne, R. E.; Kay, J.; Yates, P.; Mitrovic, I. Z.; Weerakkody, A.; Hall, S.; Durose, K. Maximizing the Optical Performance of Planar CH3NH3PbI3 Hybrid Perovskite Heterojunction Stacks. *Sol. Energy Mater. Sol. Cells* **2016**, *147*, 327–333. https://doi.org/10.1016/j.solmat.2015.10.007.

(188) Etienne, T.; Mosconi, E.; De Angelis, F. Dynamical Origin of the Rashba Effect in Organohalide Lead Perovskites: A Key to Suppressed Carrier Recombination in Perovskite Solar Cells? *J. Phys. Chem. Lett.* **2016**, *7* (9), 1638–1645. https://doi.org/10.1021/acs.jpclett.6b00564.

(189) Jeong, J.; Kim, M.; Seo, J.; Lu, H.; Ahlawat, P.; Mishra, A.; Yang, Y.; Hope, M. A.; Eickemeyer, F. T.; Kim, M.; Yoon, Y. J.; Choi, I. W.; Darwich, B. P.; Choi, S. J.; Jo, Y.; Lee, J. H.; Walker, B.; Zakeeruddin, S. M.; Emsley, L.; Rothlisberger, U.; Hagfeldt, A.; Kim, D. S.; Grätzel, M.; Kim, J. Y. Pseudo-Halide Anion Engineering for α-FAPbI 3 Perovskite Solar Cells. *Nature* **2021**, *592* (7854), 381–385. https://doi.org/10.1038/s41586-021-03406-5.

(190) Niu, G.; Guo, X.; Wang, L. Review of Recent Progress in Chemical Stability of Perovskite Solar Cells. *J. Mater. Chem. A* **2015**, *3* (17), 8970–8980. https://doi.org/10.1039/C4TA04994B.

(191) Fakharuddin, A.; De Rossi, F.; Watson, T. M.; Schmidt-Mende, L.; Jose, R. Research Update: Behind the High Efficiency of Hybrid Perovskite Solar Cells. *APL Mater.* **2016**, *4* (9), 091505. https://doi.org/10.1063/1.4962143.

(192) Berhe, T. A.; Su, W.-N.; Chen, C.-H.; Pan, C.-J.; Cheng, J.-H.; Chen, H.-M.; Tsai, M.-C.; Chen, L.-Y.; Dubale, A. A.; Hwang, B.-J. Organometal Halide Perovskite Solar Cells: Degradation and Stability. *Energy Environ. Sci.* **2016**, *9* (2), 323–356. https://doi.org/10.1039/C5EE02733K.

(193) Zhu, T.-Y.; Shu, D.-J. Polarization-Controlled Surface Defect Formation in a Hybrid Perovskite. *J. Phys. Chem. Lett.* **2021**, *12* (16), 3898–3906. https://doi.org/10.1021/acs.jpclett.1c00702.

(194) Huang, J.; Tan, S.; Lund, P. D.; Zhou, H. Impact of H2O on Organic–Inorganic Hybrid Perovskite Solar Cells. *Energy Environ. Sci.* **2017**, *10* (11), 2284–2311. https://doi.org/10.1039/C7EE01674C.

(195) Melvin, A. A.; Stoichkov, V. D.; Kettle, J.; Mogilyansky, D.; Katz, E. A.; Visoly-Fisher, I. Lead Iodide as a Buffer Layer in UV-Induced Degradation of CH3NH3PbI3 Films. *Sol. Energy* **2018**, *159*, 794–799. https://doi.org/10.1016/j.solener.2017.11.054.

(196) Aristidou, N.; Eames, C.; Sanchez-Molina, I.; Bu, X.; Kosco, J.; Islam, M. S.; Haque, S. A. Fast Oxygen Diffusion and Iodide Defects Mediate Oxygen-Induced Degradation of Perovskite Solar Cells. *Nat. Commun.* **2017**, *8* (1), 15218. https://doi.org/10.1038/ncomms15218.

(197) Juarez-Perez, E. J.; Ono, L. K.; Uriarte, I.; Cocinero, E. J.; Qi, Y. Degradation Mechanism and Relative Stability of Methylammonium Halide Based Perovskites Analyzed on the Basis of Acid–Base Theory. *ACS Appl. Mater. Interfaces* **2019**, *11* (13), 12586–12593. https://doi.org/10.1021/acsami.9b02374.
(198) Ahn, N.; Kwak, K.; Jang, M. S.; Yoon, H.; Lee, B. Y.; Lee, J.-K.; Pikhitsa, P. V.; Byun, J.; Choi, M. Trapped Charge-Driven Degradation of Perovskite Solar Cells. *Nat. Commun.* **2016**, *7* (1), 13422. https://doi.org/10.1038/ncomms13422.
(199) Bryant, D.; Aristidou, N.; Pont, S.; Sanchez-Molina, I.; Chotchunangatchaval, T.; Wheeler, S.; Durrant, J. R.; Haque, S. A. Light and Oxygen Induced Degradation Limits the Operational Stability of Methylammonium Lead Triiodide Perovskite Solar Cells. *Energy Environ. Sci.* **2016**, *9* (5), 1655–1660. https://doi.org/10.1039/C6EE00409A.
(200) Abdelmageed, G.; Jewell, L.; Hellier, K.; Seymour, L.; Luo, B.; Bridges, F.; Zhang, J. Z.; Carter, S. Mechanisms for Light Induced Degradation in MAPbI3 Perovskite Thin Films and Solar Cells. *Appl. Phys. Lett.* **2016**, *109* (23), 233905. https://doi.org/10.1063/1.4967840.
(201) Ouyang, Y.; Li, Y.; Zhu, P.; Li, Q.; Gao, Y.; Tong, J.; Shi, L.; Zhou, Q.; Ling, C.; Chen, Q.; Deng, Z.; Tan, H.; Deng, W.; Wang, J. Photo-Oxidative Degradation of Methylammonium Lead Iodide Perovskite: Mechanism and Protection. *J. Mater. Chem. A* **2019**, *7* (5), 2275–2282. https://doi.org/10.1039/C8TA12193A.
(202) Aharon, S.; Cohen, B. E.; Etgar, L. Hybrid Lead Halide Iodide and Lead Halide Bromide in Efficient Hole Conductor Free Perovskite Solar Cell. *J. Phys. Chem. C* **2014**, *118* (30), 17160–17165. https://doi.org/10.1021/jp5023407.
(203) Ouafi, M.; Jaber, B.; Atourki, L.; Bekkari, R.; Laânab, L. Improving UV Stability of MAPbI3 Perovskite Thin Films by Bromide Incorporation. *J. Alloys Compd.* **2018**, *746*, 391–398. https://doi.org/10.1016/j.jallcom.2018.02.240.
(204) Ni, Z.; Jiao, H.; Fei, C.; Gu, H.; Xu, S.; Yu, Z.; Yang, G.; Deng, Y.; Jiang, Q.; Liu, Y.; Yan, Y.; Huang, J. Evolution of Defects during the Degradation of Metal Halide Perovskite Solar Cells under Reverse Bias and Illumination. *Nat. Energy* **2022**, *7* (1), 65–73. https://doi.org/10.1038/s41560-021-00949-9.
(205) Duan, L.; Uddin, A. Defects and Stability of Perovskite Solar Cells: A Critical Analysis. *Mater. Chem. Front.* **2022**, *6* (4), 400–417. https://doi.org/10.1039/D1QM01250A.
(206) Musiienko, A.; Ceratti, D. R.; Pipek, J.; Brynza, M.; Elhadidy, H.; Belas, E.; Betušiak, M.; Delport, G.; Praus, P. Defects in Hybrid Perovskites: The Secret of Efficient Charge Transport. *Adv. Funct. Mater.* **2021**, *31* (48), 2104467. https://doi.org/10.1002/adfm.202104467.
(207) De Marco, N.; Zhou, H.; Chen, Q.; Sun, P.; Liu, Z.; Meng, L.; Yao, E.-P.; Liu, Y.; Schiffer, A.; Yang, Y. Guanidinium: A Route to Enhanced Carrier Lifetime and Open-Circuit Voltage in Hybrid Perovskite Solar Cells. *Nano Lett.* **2016**, *16* (2), 1009–1016. https://doi.org/10.1021/acs.nanolett.5b04060.
(208) Zhang, L.; Sit, P. H.-L. Ab Initio Study of the Dynamics of Electron Trapping and Detrapping Processes in the CH3NH3PbI3 Perovskite. *J. Mater. Chem. A* **2019**, *7* (5), 2135–2147. https://doi.org/10.1039/C8TA09512D.
(209) Zhang, X.; Turiansky, M. E.; Shen, J.-X.; Van de Walle, C. G. Iodine Interstitials as a Cause of Nonradiative Recombination in Hybrid Perovskites. *Phys. Rev. B* **2020**, *101* (14), 140101. https://doi.org/10.1103/PhysRevB.101.140101.

(210) Brenes, R.; Eames, C.; Bulović, V.; Islam, M. S.; Stranks, S. D. The Impact of Atmosphere on the Local Luminescence Properties of Metal Halide Perovskite Grains. *Adv. Mater.* **2018**, *30* (15), 1706208. https://doi.org/10.1002/adma.201706208.
(211) Christians, J. A.; Miranda Herrera, P. A.; Kamat, P. V. Transformation of the Excited State and Photovoltaic Efficiency of CH3NH3PbI3 Perovskite upon Controlled Exposure to Humidified Air. *J. Am. Chem. Soc.* **2015**, *137* (4), 1530–1538. https://doi.org/10.1021/ja511132a.
(212) Leijtens, T.; Eperon, G. E.; Noel, N. K.; Habisreutinger, S. N.; Petrozza, A.; Snaith, H. J. Stability of Metal Halide Perovskite Solar Cells. *Adv. Energy Mater.* **2015**, *5* (20), 1500963. https://doi.org/10.1002/aenm.201500963.
(213) Yang, J.; Siempelkamp, B. D.; Liu, D.; Kelly, T. L. Investigation of CH3NH3PbI3 Degradation Rates and Mechanisms in Controlled Humidity Environments Using in Situ Techniques. *ACS Nano* **2015**, *9* (2), 1955–1963. https://doi.org/10.1021/nn506864k.
(214) Lu, Y.-B.; Cong, W.-Y.; Guan, C.; Sun, H.; Xin, Y.; Wang, K.; Song, S. Light Enhanced Moisture Degradation of Perovskite Solar Cell Material CH3NH3PbI3. *J. Mater. Chem. A* **2019**, *7* (48), 27469–27474. https://doi.org/10.1039/C9TA10443G.
(215) Ogunniran, K. O.; Martins, N. T. Humidity and Moisture Degradation of Perovskite Material in Solar Cells: Effects on Efficiency. *IOP Conf. Ser. Earth Environ. Sci.* **2021**, *655* (1), 012049. https://doi.org/10.1088/1755-1315/655/1/012049.
(216) Kundu, S.; Kelly, T. L. In Situ Studies of the Degradation Mechanisms of Perovskite Solar Cells. *EcoMat* **2020**, *2* (2), e12025. https://doi.org/10.1002/eom2.12025.
(217) Zheng, C.; Rubel, O. Unraveling the Water Degradation Mechanism of CH3NH3PbI3. *J. Phys. Chem. C* **2019**, *123* (32), 19385–19394. https://doi.org/10.1021/acs.jpcc.9b05516.
(218) Kwak, K.; Lim, E.; Ahn, N.; Heo, J.; Bang, K.; Kim, S. K.; Choi, M. An Atomistic Mechanism for the Degradation of Perovskite Solar Cells by Trapped Charge. *Nanoscale* **2019**, *11* (23), 11369–11378. https://doi.org/10.1039/C9NR02193K.
(219) Zhu, Z.; Hadjiev, V. G.; Rong, Y.; Guo, R.; Cao, B.; Tang, Z.; Qin, F.; Li, Y.; Wang, Y.; Hao, F.; Venkatesan, S.; Li, W.; Baldelli, S.; Guloy, A. M.; Fang, H.; Hu, Y.; Yao, Y.; Wang, Z.; Bao, J. Interaction of Organic Cation with Water Molecule in Perovskite MAPbI3: From Dynamic Orientational Disorder to Hydrogen Bonding. *Chem. Mater.* **2016**, *28* (20), 7385–7393. https://doi.org/10.1021/acs.chemmater.6b02883.
(220) Cui, Y.; Chen, C.; Li, C.; Chen, L.; Bista, S. S.; Liu, X.; Li, Y.; Awni, R. A.; Song, Z.; Yan, Y. Correlating Hysteresis and Stability with Organic Cation Composition in the Two-Step Solution-Processed Perovskite Solar Cells. *ACS Appl. Mater. Interfaces* **2020**, *12* (9), 10588–10596. https://doi.org/10.1021/acsami.9b23374.
(221) Oranskaia, A.; Yin, J.; Bakr, O. M.; Brédas, J.-L.; Mohammed, O. F. Halogen Migration in Hybrid Perovskites: The Organic Cation Matters. *J. Phys. Chem. Lett.* **2018**, *9* (18), 5474–5480. https://doi.org/10.1021/acs.jpclett.8b02522.
(222) Zhang, X.; Shen, J.-X.; Turiansky, M. E.; Van de Walle, C. G. Minimizing Hydrogen Vacancies to Enable Highly Efficient Hybrid Perovskites. *Nat. Mater.* **2021**, *20* (7), 971–976. https://doi.org/10.1038/s41563-021-00986-5.
(223) Lyu, M.; Yun, J.-H.; Chen, P.; Hao, M.; Wang, L. Addressing Toxicity of Lead: Progress and Applications of Low-Toxic Metal Halide Perovskites and Their Derivatives. *Adv. Energy Mater.* **2017**, *7* (15), 1602512. https://doi.org/10.1002/aenm.201602512.
(224) Prakash, J.; Singh, A.; Sathiyan, G.; Ranjan, R.; Singh, A.; Garg, A.; Gupta, R. K. Progress in Tailoring Perovskite Based Solar Cells through Compositional Engineering: Materials

Properties, Photovoltaic Performance and Critical Issues. *Mater. Today Energy* **2018**, *9*, 440–486. https://doi.org/10.1016/j.mtener.2018.07.003.

(225) Peng, L.; Xie, W. Theoretical and Experimental Investigations on the Bulk Photovoltaic Effect in Lead-Free Perovskites MASnI3 and FASnI3. *RSC Adv.* **2020**, *10* (25), 14679–14688. https://doi.org/10.1039/D0RA02584D.

(226) Krishnamoorthy, T.; Ding, H.; Yan, C.; Leong, W. L.; Baikie, T.; Zhang, Z.; Sherburne, M.; Li, S.; Asta, M.; Mathews, N.; Mhaisalkar, S. G. Lead-Free Germanium Iodide Perovskite Materials for Photovoltaic Applications. *J. Mater. Chem. A* **2015**, *3* (47), 23829–23832. https://doi.org/10.1039/C5TA05741H.

(227) Zhao, Y.; Nardes, A. M.; Zhu, K. Mesoporous Perovskite Solar Cells: Material Composition, Charge-Carrier Dynamics, and Device Characteristics. *Faraday Discuss.* **2015**, *176* (0), 301–312. https://doi.org/10.1039/C4FD00128A.

(228) Busipalli, D. L.; Nachimuthu, S.; Jiang, J. Theoretical Study on Halide and Mixed Halide Perovskite Solar Cells: Effects of Halide Atoms on the Stability and Electronic Properties. *J. Chin. Chem. Soc.* **2019**, *66* (6), 575–582. https://doi.org/10.1002/jccs.201800443.

(229) López, C. A.; Alvarez-Galván, M. C.; Martínez-Huerta, M. V.; Fauth, F.; Alonso, J. A. Crystal Structure Features of CH3NH3PbI3−xBrx Hybrid Perovskites Prepared by Ball Milling: A Route to More Stable Materials. *CrystEngComm* **2020**, *22* (4), 767–775. https://doi.org/10.1039/C9CE01461F.

(230) Luan, M.; Song, J.; Wei, X.; Chen, F.; Liu, J. Controllable Growth of Bulk Cubic-Phase CH3NH3PbI3 Single Crystal with Exciting Room-Temperature Stability. *CrystEngComm* **2016**, *18* (28), 5257–5261. https://doi.org/10.1039/C6CE00375C.

(231) Suzuki, A.; Okada, H.; Oku, T. Role of Bromine Doping on the Photovoltaic Properties and Microstructures of CH3NH3PbI3 Perovskite Solar Cells. *AIP Conf. Proc.* **2016**, *1709* (1), 020022. https://doi.org/10.1063/1.4941221.

(232) Qian, J.; Xu, B.; Tian, W. A Comprehensive Theoretical Study of Halide Perovskites ABX3. *Org. Electron.* **2016**, *37*, 61–73. https://doi.org/10.1016/j.orgel.2016.05.046.

(233) Otero, R.; Vázquez de Parga, A. L.; Gallego, J. M. Electronic, Structural and Chemical Effects of Charge-Transfer at Organic/Inorganic Interfaces. *Surf. Sci. Rep.* **2017**, *72* (3), 105–145. https://doi.org/10.1016/j.surfrep.2017.03.001.

(234) Al-Shami, A.; Lakhal, M.; Hamedoun, M.; El Kenz, A.; Benyoussef, A.; Loulidi, M.; Ennaoui, A.; Mounkachi, O. Tuning the Optical and Electrical Properties of Orthorhombic Hybrid Perovskite CH3NH3PbI3 by First-Principles Simulations: Strain-Engineering. *Sol. Energy Mater. Sol. Cells* **2018**, *180*, 266–270. https://doi.org/10.1016/j.solmat.2017.06.047.

(235) Yang, J.-P.; Meissner, M.; Yamaguchi, T.; Zhang, X.-Y.; Ueba, T.; Cheng, L.-W.; Ideta, S.; Tanaka, K.; Zeng, X.-H.; Ueno, N.; Kera, S. Band Dispersion and Hole Effective Mass of Methylammonium Lead Iodide Perovskite. *Sol. RRL* **2018**, *2* (10), 1800132. https://doi.org/10.1002/solr.201800132.

(236) Walsh, A.; Payne, D. J.; Egdell, R. G.; Watson, G. W. Stereochemistry of Post-Transition Metal Oxides: Revision of the Classical Lone Pair Model. *Chem. Soc. Rev.* **2011**, *40* (9), 4455–4463. https://doi.org/10.1039/c1cs15098g.

(237) Momblona, C.; Gil-Escrig, L.; Bandiello, E.; Hutter, E. M.; Sessolo, M.; Lederer, K.; Blochwitz-Nimoth, J.; Bolink, H. J. Efficient Vacuum Deposited P-i-n and n-i-p Perovskite Solar Cells Employing Doped Charge Transport Layers. *Energy Environ. Sci.* **2016**, *9* (11), 3456–3463. https://doi.org/10.1039/C6EE02100J.

(238) Kim, J.; Lee, S.-C.; Lee, S.-H.; Hong, K.-H. Importance of Orbital Interactions in Determining Electronic Band Structures of Organo-Lead Iodide. *J. Phys. Chem. C* **2015**, *119* (9), 4627–4634. https://doi.org/10.1021/jp5126365.
(239) Buin, A.; Comin, R.; Xu, J.; Ip, A. H.; Sargent, E. H. Halide-Dependent Electronic Structure of Organolead Perovskite Materials. *Chem. Mater.* **2015**, *27* (12), 4405–4412. https://doi.org/10.1021/acs.chemmater.5b01909.
(240) Lee, J.-H.; Bristowe, N. C.; Lee, J. H.; Lee, S.-H.; Bristowe, P. D.; Cheetham, A. K.; Jang, H. M. Resolving the Physical Origin of Octahedral Tilting in Halide Perovskites. *Chem. Mater.* **2016**, *28* (12), 4259–4266. https://doi.org/10.1021/acs.chemmater.6b00968.
(241) Madsen, G. K. H.; Singh, D. J. BoltzTraP. A Code for Calculating Band-Structure Dependent Quantities. *Comput. Phys. Commun.* **2006**, *175* (1), 67–71. https://doi.org/10.1016/j.cpc.2006.03.007.
(242) Singh, R.; Kottokkaran, R.; Dalal, V. L.; Balasubramanian, G. Engineering Band Gap and Electronic Transport in Organic–Inorganic Halide Perovskites by Superlattices. *Nanoscale* **2017**, *9* (25), 8600–8607. https://doi.org/10.1039/C7NR00459A.
(243) Yamada, K.; Kawaguchi, H.; Matsui, T.; Okuda, T.; Ichiba, S. Structural Phase Transition and Electrical Conductivity of the Perovskite CH3NH3Sn1-XPbxBr3 and CsSnBr3. *Bull. Chem. Soc. Jpn.* **1990**, *63* (9), 2521–2525. https://doi.org/10.1246/bcsj.63.2521.
(244) Durmus, H.; Safak, H.; Akbas, H. Z.; Ahmetli, G. Optical Properties of Modified Epoxy Resin with Various Oxime Derivatives in the UV-VIS Spectral Region. *J. Appl. Polym. Sci.* **2011**, *120* (3), 1490–1495. https://doi.org/10.1002/app.33287.
(245) Barugkin, C.; Cong, J.; Duong, T.; Rahman, S.; Nguyen, H. T.; Macdonald, D.; White, T. P.; Catchpole, K. R. Ultralow Absorption Coefficient and Temperature Dependence of Radiative Recombination of CH3NH3PbI3 Perovskite from Photoluminescence. *J. Phys. Chem. Lett.* **2015**, *6* (5), 767–772. https://doi.org/10.1021/acs.jpclett.5b00044.
(246) Kanemitsu, Y. Luminescence Spectroscopy of Lead-Halide Perovskites: Materials Properties and Application as Photovoltaic Devices. *J. Mater. Chem. C* **2017**, *5* (14), 3427–3437. https://doi.org/10.1039/C7TC00669A.
(247) Xu, Q.; Yang, D.; Lv, J.; Sun, Y.-Y.; Zhang, L. Perovskite Solar Absorbers: Materials by Design. *Small Methods* **2018**, *2* (5), 1700316. https://doi.org/10.1002/smtd.201700316.
(248) Atourki, L.; Vega, E.; Marí, B.; Mollar, M.; Ait Ahsaine, H.; Bouabid, K.; Ihlal, A. Role of the Chemical Substitution on the Structural and Luminescence Properties of the Mixed Halide Perovskite Thin MAPbI3−xBrx (0≤x≤1) Films. *Appl. Surf. Sci.* **2016**, *371*, 112–117. https://doi.org/10.1016/j.apsusc.2016.02.207.
(249) Jong, U.-G.; Yu, C.-J.; Ri, J.-S.; Kim, N.-H.; Ri, G.-C. Influence of Halide Composition on the Structural, Electronic, and Optical Properties of Mixed ${\mathrm{CH}}_{3}{\mathrm{NH}}_{3}\mathrm{Pb}({\mathrm{I}}_{1\ensuremath{-}x}{\mathrm{Br}}_{x})}_{3}$ Perovskites Calculated Using the Virtual Crystal Approximation Method. *Phys. Rev. B* **2016**, *94* (12), 125139. https://doi.org/10.1103/PhysRevB.94.125139.
(250) Liu, M.; Johnston, M. B.; Snaith, H. J. Efficient Planar Heterojunction Perovskite Solar Cells by Vapour Deposition. *Nature* **2013**, *501* (7467), 395–398. https://doi.org/10.1038/nature12509.
(251) Togo, A.; Tanaka, I. First Principles Phonon Calculations in Materials Science. *Scr. Mater.* **2015**, *108*, 1–5. https://doi.org/10.1016/j.scriptamat.2015.07.021.

(252) Senocrate, A.; Acartürk, T.; Kim, G. Y.; Merkle, R.; Starke, U.; Grätzel, M.; Maier, J. Interaction of Oxygen with Halide Perovskites. *J. Mater. Chem. A* **2018**, *6* (23), 10847–10855. https://doi.org/10.1039/C8TA04537B.
(253) Deretzis, I.; Alberti, A.; Pellegrino, G.; Smecca, E.; Giannazzo, F.; Sakai, N.; Miyasaka, T.; La Magna, A. Atomistic Origins of CH3NH3PbI3 Degradation to PbI2 in Vacuum. *Appl. Phys. Lett.* **2015**, *106* (13), 131904. https://doi.org/10.1063/1.4916821.
(254) Wei, L.; Ma, W.; Lian, C.; Meng, S. Benign Interfacial Iodine Vacancies in Perovskite Solar Cells. *J Phys Chem C* **2017**, 9.
(255) She, L.; Liu, M.; Zhong, D. Atomic Structures of CH3NH3PbI3 (001) Surfaces. *ACS Nano* **2016**, *10* (1), 1126–1131. https://doi.org/10.1021/acsnano.5b06420.
(256) Buin, A.; Pietsch, P.; Xu, J.; Voznyy, O.; Ip, A. H.; Comin, R.; Sargent, E. H. Materials Processing Routes to Trap-Free Halide Perovskites. *Nano Lett.* **2014**, *14* (11), 6281–6286. https://doi.org/10.1021/nl502612m.
(257) Du, M. H. Efficient Carrier Transport in Halide Perovskites: Theoretical Perspectives. *J. Mater. Chem. A* **2014**, *2* (24), 9091–9098. https://doi.org/10.1039/C4TA01198H.
(258) Tan, S.; Yavuz, I.; Weber, M. H.; Huang, T.; Chen, C.-H.; Wang, R.; Wang, H.-C.; Ko, J. H.; Nuryyeva, S.; Xue, J.; Zhao, Y.; Wei, K.-H.; Lee, J.-W.; Yang, Y. Shallow Iodine Defects Accelerate the Degradation of α-Phase Formamidinium Perovskite. *Joule* **2020**, *4* (11), 2426–2442. https://doi.org/10.1016/j.joule.2020.08.016.
(259) Tong, C.-J.; Geng, W.; Tang, Z.-K.; Yam, C.-Y.; Fan, X.-L.; Liu, J.; Lau, W.-M.; Liu, L.-M. Uncovering the Veil of the Degradation in Perovskite CH3NH3PbI3 upon Humidity Exposure: A First-Principles Study. *J. Phys. Chem. Lett.* **2015**, *6* (16), 3289–3295. https://doi.org/10.1021/acs.jpclett.5b01544.
(260) Kakekhani, A.; Katti, R. N.; Rappe, A. M. Water in Hybrid Perovskites: Bulk MAPbI3 Degradation via Super-Hydrous State. *APL Mater.* **2019**, *7* (4), 041112. https://doi.org/10.1063/1.5087290.
(261) Li, Q.; Chen, Z.; Tranca, I.; Gaastra-Nedea, S.; Smeulders, D.; Tao, S. Compositional Effect on Water Adsorption on Metal Halide Perovskites. *Appl. Surf. Sci.* **2021**, *538*, 148058. https://doi.org/10.1016/j.apsusc.2020.148058.
(262) Zhang, L.; Sit, P. H.-L. Ab Initio Study of Interaction of Water, Hydroxyl Radicals, and Hydroxide Ions with CH3NH3PbI3 and CH3NH3PbBr3 Surfaces. *J. Phys. Chem. C* **2015**, *119* (39), 22370–22378. https://doi.org/10.1021/acs.jpcc.5b07000.
(263) Diao, X.-F.; Tang, Y.; Tang, T.; Xie, Q.; Xiang, K.; Liu, G. Study on the Stability of Organic–Inorganic Perovskite Solar Cell Materials Based on First Principle. *Mol. Phys.* **2020**, *118* (8), e1665200. https://doi.org/10.1080/00268976.2019.1665200.
(264) Leppert, L.; Reyes-Lillo, S. E.; Neaton, J. B. Electric Field- and Strain-Induced Rashba Effect in Hybrid Halide Perovskites. *J. Phys. Chem. Lett.* **2016**, *7* (18), 3683–3689. https://doi.org/10.1021/acs.jpclett.6b01794.
(265) Fan, P.; Gu, D.; Liang, G.-X.; Luo, J.-T.; Chen, J.-L.; Zheng, Z.-H.; Zhang, D.-P. High-Performance Perovskite CH3NH3PbI3 Thin Films for Solar Cells Prepared by Single-Source Physical Vapour Deposition. *Sci. Rep.* **2016**, *6* (1), 29910. https://doi.org/10.1038/srep29910.
(266) Liu, D.; Gangishetty, M. K.; Kelly, T. L. Effect of CH3NH3PbI3 Thickness on Device Efficiency in Planar Heterojunction Perovskite Solar Cells. *J. Mater. Chem. A* **2014**, *2* (46), 19873–19881. https://doi.org/10.1039/C4TA02637C.

(267) Filip, M. R.; Verdi, C.; Giustino, F. GW Band Structures and Carrier Effective Masses of CH3NH3PbI3 and Hypothetical Perovskites of the Type APbI3: A = NH4, PH4, AsH4, and SbH4. *J. Phys. Chem. C* **2015**, *119* (45), 25209–25219. https://doi.org/10.1021/acs.jpcc.5b07891.